



Title	A CFD Study on Added Resistance, Motions and Phase Averaged Wake Fields of Full Form Ship Model in Head Waves
Author(s)	Wu, Ping-Chen
Citation	大阪大学, 2013, 博士論文
Version Type	VoR
URL	https://doi.org/10.18910/26191
rights	
Note	

The University of Osaka Institutional Knowledge Archive : OUKA

<https://ir.library.osaka-u.ac.jp/>

The University of Osaka

Doctoral Dissertation

A CFD Study on Added Resistance, Motions
and Phase Averaged Wake Fields of Full Form
Ship Model in Head Waves

Ping-Chen Wu

July 2013

Graduate School of Engineering,
Osaka University

TABLE OF CONTENTS

List of symbols.....	1
List of tables.....	6
List of figures.....	8
CHAPTER 1: INTRODUCTION.....	13
 1.1 Computation methods of added resistance.....	13
1.1.1 Analytical method.....	13
1.1.2 Unsteady wave pattern analysis and ray theory.....	17
1.1.3 Advanced potential flow method.....	19
1.1.4 CFD.....	24
 1.2 The dependence of added resistance.....	26
1.2.1 Ship motions and maximum forces/moments responses.....	27
1.2.2 Ship speed/Froude number.....	30
1.2.3 Heading angle.....	30
1.2.4 Wave length and amplitude.....	32
1.2.5 Ship geometry.....	33
1.2.6 Relative motion.....	35
1.2.7 Propulsion and nominal wakes in waves.....	36
CHAPTER 2: EFD METHODS.....	38

2.1 Ship geometry.....	38
2.2 Osaka University.....	38
2.3 Other EFD resources.....	44
2.4 Evaluation of facility biases.....	46
CHAPTER 3: CFD METHODS.....	49
3.1 CFDSHIP-IOWA.....	49
3.2 Boundary conditions, grids, and computational domain.....	50
3.3 Simulation conditions.....	55
CHAPTER 4: UNCERTAINTY ANALYSIS.....	56
4.1 The theory of verification and validation.....	56
4.2 Result of verification study.....	58
4.3 Verification for phases.....	60
CHAPTER 5: MAXIMUM SHIP RESPONSE.....	63
5.1 1 DOF ship motion.....	63
5.2 Maximum ship response condition.....	64
5.3 Diffraction and radiation problem in PF and CFD.....	66
5.4 CFD natural frequency simulations.....	67
CHAPTER 6: GLOBAL VARIABLE RESULTS.....	69
6.1 Calm water results.....	69
6.2 Fully-loaded condition.....	71

6.2.1 Time history study.....	71
6.2.2 Motion responses.....	77
6.2.3 Forces, moments and added resistance responses.....	83
6.2.4 Maximum responses.....	91
6.2.5 Comparison with PF predictions.....	93
6.2.6 Wave amplitude effect.....	95
6.3 Ballast condition.....	96
6.3.1 Time history.....	96
6.3.2 Motion responses and added resistance.....	99
CHAPTER 7: LOCAL FLOW ANALYSIS.....	105
7.1 Force distribution on the hull.....	105
7.2 Unsteady wave pattern analysis.....	109
7.3 Nominal wake analysis.....	115
7.3.1 Boundary layer development.....	115
7.3.2 Propeller plane in tank fixed coordinate.....	118
7.3.3 Propeller plane in ship fixed coordinate.....	125
a. Vortex behavior in nominal wake.....	125
b. Orbital velocity.....	129
c. Volume mean velocity.....	131
d. Fourier analysis on propeller plane.....	134
e. Simple estimate for thrust and torque.....	138
CHAPTER 8: CONCLUSIONS AND FUTURE WORKS.....	141

Reference.....	146
Acknowledgements.....	155
List of publications.....	156
Curriculum vitae.....	158

List of symbols

α	:Damping
Γ	:Circulation
Δ	:Ship mass or moment of inertia
Δ_A	:Added mass or added inertia
ε_{DF}	:Diffraction phase
ε_{FK}	:Froude-Krylov phase
ζ	:Free surface elevation (m)
λ	:Wave length (m)
ν_t	:Turbulent kinematic viscosity (Ns m ⁻²)
ρ	:Water density (Kg m ⁻³)
σ	:Ship sinkage (mm)
τ	:Ship trim (°)
ω	:Wave frequency (s ⁻¹)
ω_e	:Encounter frequency (s ⁻¹)
ω_t	:Specific dissipation rate (s ⁻¹)
$\overline{\omega_x}$:X-direction vorticity
A	:Wave amplitude=wave height H/2 (m)
\hat{A}	:Area
A_{DF}	:Diffraction amplitude
A_{FK}	:Froude-Krylov amplitude
A_W	:Wetted area
B	:Beam length of the ship=Bwl (m)

B	:Damping term
C	:Restoring term
B_{wl}	:Maximum beam at the waterline (m)
C_{aw}	:Added resistance coefficient
C_B, CB	:Block coefficient
C_{IT}	:Coefficient of inertia of the water plane area
C_p	:Pressure coefficient
C_F	:Friction resistance coefficient
C_M	:Midship Coefficient
C_T	:Resistance coefficient
C_{Wp}	:Water plane area coefficient
D	:Experimental data
$E\%D$:Comparison Error=100($D-S$)/ D
F_o	:External force (N)
f_θ	:Pitch natural frequency (HZ)
f_e	:Encounter frequency=2 $\pi\omega_e$
f_n	:Natural frequency (s ⁻¹)
Fr	:Froude number based on ship length
f_s	:Spring natural frequency (s ⁻¹)
F_x	:X-direction Hydrodynamic force (N)
F'_x	:Inertial force (N)
F_W	:Wave force (N)
f_z	:Heave natural frequency (HZ)
g	:gravity (N m ⁻²)

I_y	:Moment of inertia around y axis
J	:Ship advance ratio= $U/(n^2 r_p)$, n: propeller's rotational speed
k	:Form factor = C_T/ C_F
k	:wave number
K	:Spring stiffness (N m ⁻¹)
KG	:Ship's center of gravity above keel (m)
k_t	:Turbulent kinetic energy (m ² s ⁻²)
K_T	:Thrust coefficient=Thrust(N)/(16 $\rho r p^4 n^2$)
K_Q	:Torque coefficient=Torque(N m)/(32 $\rho r p^5 n^2$)
K _{XX} , K _{YY} , K _{ZZ}	:Radius of gyration (m)
L	:Ship length= L _{pp} (m)
LCB	:Longitudinal center of buoyancy (%)
LCG	:Longitudinal center of gravity (m)
L _{pp}	:Ship length between perpendiculars (m)
Lwl	:Ship length at the waterline (m)
m	:Total mass of the moving parts (Kg)
m_1	:Mass of the model and pitch free gimbals (Kg)
m_2	:Mass of dynamometer (Kg)
m_3	:Mass of light weight carriage (Kg)
m_x	:Added mass (Kg)
p	:Pressure in flow field (N m ⁻²)
R	:Resistance (N)
r_o	:hub radius
r_p	:Propeller radius

R_C	:Resistance in calm water (N)
R_{Co}	:Resistance in calm water at advance speed U_0 (N)
R_{AW}	:Added resistance in waves= $X_0 - X_S$ (N)
Re	:Reynolds number
R_G	:Parameter refinement ratio
P_G	:Order of accuracy
q	: Q-criterion
S	:Simulation result
t	:time (s)
T	:Ship draft (m)
T_A, T_F	:Draft of ship aft and forward (m)
T_e	:Encounter period (s)
u'	:Orbital velocity (potential flow)
U	:Ship speed (m s ⁻¹)
U_0	:Carriage speed (m s ⁻¹)
U_G	:Grid Uncertainty (%)
u_N	:Volume average axial velocity
x	:Surge motion (m)
X	:Surge force, x-force (N)
x, y, z	:x, y, z location in Cartesian coordinate system (m)
X_0	:Mean value of x-force (N)
X_1	:1 st harmonic amplitude of x-force (N)
X_2	:2 nd harmonic amplitude of x-force (N)
X_{DF}	:Diffraction forces

X_E	:Wave excitation forces
X_{FK}	:Froude-Krylov force
X_G	:Gravitational forces
X_{HD}	:Hydrodynamic forces
X_{HS}	:Hydrostatic forces
X_{RF}	:Radiation forces
X_S	:Steady x-force in calm water
X_{TF}	:Total wave forces
u, v, w	:Velocity component in flow field (m s ⁻¹)
$u, w; q$:Surge, heave and pitch velocity (m s ⁻¹)
x_0, z_0, θ_0	:Mean value of ship motions: surge (cm), heave (cm), and pitch (°)
x_1, z_1, θ_1	:1 st harmonic amplitude of ship motions: surge (cm), heave (cm), and pitch (°)
$x_{e1}, z_{e1}, \theta_{e1}$:1 st harmonic phase of surge, heave and pitch
Z	:z-direction force (N)

List of tables

Table 1-1 Added resistance and ship motions for different geometries	29
Table 2-1 Ship model properties (OU 1/100 model).....	39
Table 2-2 EFD and CFD test conditions.....	42
Table 2-3 Facility biases for calm water resistance, sinkage and trim.....	46
Table 3-1 Boundary conditions.....	51
Table 3-2 Grid systems.....	53
Table 4-1 Verification study for $\lambda/L=1.1$ (fully-loaded condition).....	58
Table 4-2 Phase values for verification studies.....	62
Table 5-1 Natural frequency in calm water at $Fr=0.0$	68
Table 6-1 Comparison of CFD and EFD resistance force and motions for resistance test in calm water.....	69
Table 6-2 Running mean and running RMS of EFD and CFD time histories.....	72
Table 6-3 Prediction errors for free surge condition for CFD and EUT simulations.....	81
Table 6-4 Prediction errors for CFD simulations for fixed surge condition.....	81
Table 6-5 Scatter of EFD data (OU, free surge) (% of average value).....	81
Table 6-6 Difference between total CFD force/moment with free surge condition and the combination of wave exciting and radiation force/moment for $Fr=0.142$...	85
Table 6-7 Difference between total CFD force/moment with fixed surge condition and the combination of wave exciting and radiation force/moment for $Fr=0.142$...	86
Table 6-8 Difference between total CFD force/moment with fixed surge condition and the combination of wave exciting and radiation force/moment for $Fr=0.25$	86

Table 6-9 Prediction errors for free and fixed surge condition for CFD in ballast condition (EFD source: OU, free surge)	104
Table 7-1 Orbital velocity and time average of volume average velocity.....	130

List of figures

Fig. 1-1 Review of added resistance and surge, wave excitation total forces and moments for fixed/free ship in head waves for different geometries.....	27
Fig. 2-1 KVLCC2 body plan and hull form.....	39
Fig. 1-2 Test setup for free surge condition.....	40
Fig. 2-3 PIV system.....	40
Fig. 3-1 Overset grid system, four blocks (three for short wave cases): boundary layer, shaft, stern bulb, background and refinement (there is no refinement block for short wave case)	51
Fig. 3-2 Computational domain for both short and long waves.....	54
Fig. 4-1 Time history of verification cases for ship motions.....	61
Fig. 6-1 The results for $\lambda/L=0.6$: (a) Wave signal and motions; (b) Running mean time histories; (c) Running root mean square time histories.....	73
Fig. 6-2 The results for $\lambda/L=1.1$: (a) Wave signal and motions; (b) Running mean time histories; (c) Running root mean square time histories.....	75
Fig. 6-3 The results for $\lambda/L=1.6$: (a) Wave signal and motions; (b) Running mean time histories; (c) Running root mean square time histories.....	76
Fig. 6-4 1 st harmonic amplitude and phase responses of surge motion at $Fr=0.142$	77
Fig. 6-5 1 st harmonic amplitude, phase responses and mean value of heave motion at $Fr=0.142$ and 0.25.....	78
Fig. 6-6 1 st harmonic amplitude, phase responses and mean value of pitch motion at $Fr=0.142$ and 0.25.....	80

Fig. 6-7 Amplitude and phase of relative motion for $Fr=0.142$ and 0.25 : (a) bow;	82
(b) stern.....	
Fig. 6-8 1 st and 2 nd harmonic amplitude and phase of surge force: (a) $Fr=0.142$;	84
(b) $Fr= 0.25$	
Fig. 6-9 Added resistance at $Fr=0.25$ and 0.142	87
Fig. 6-10 1 st and 2 nd harmonic amplitude and phase of heave force: (a) $Fr=0.142$;	89
(b) $Fr= 0.25$	
Fig. 6-11 1 st and 2 nd harmonic amplitude and phase of pitch moment: (a)	90
$Fr=0.142$; (b) $Fr= 0.25$	
Fig. 6-12 Time history of heave and pitch motion for ballast condition at $\lambda/L=0.6$.	96
Fig. 6-13 Time history of heave and pitch motion for ballast condition at $\lambda/L=0.9$.	97
Fig. 6-14 Time history of heave and pitch motion for ballast condition at $\lambda/L=1.6$.	98
Fig. 6-15 1 st harmonic amplitude and phase of surge motion for ballast condition	99
at $Fr=0.142$	
Fig. 6-16 1 st harmonic amplitude and phase of heave motion for ballast condition	101
at $Fr=0.142$	
Fig. 6-17 1 st harmonic amplitude and phase of pitch motion for ballast condition	102
at $Fr=0.142$	
Fig. 6-18 Added resistance at $Fr=0.142$ for ballast condition.....	103
Fig. 7-1 Local resistance difference and ship motions ($\lambda/L=0.1810$, fixed surge).	107
(a) $t/T_e=0$; (b) $t/T_e=0.25$; (c) $t/T_e=0.5$; (d) $t/T_e=0.75$	
Fig. 7-2 Local resistance difference and ship motions ($\lambda/L=0.6$, fixed surge). (a)	107
$t/T_e=0$; (b) $t/T_e=0.25$; (c) $t/T_e=0.5$; (d) $t/T_e=0.75$	
Fig. 7-3 Local resistance difference and ship motions ($\lambda/L=1.1$, fixed surge). (a)	108

$t/T_e=0$; (b) $t/T_e=0.25$; (c) $t/T_e=0.5$; (d) $t/T_e=0.75$

Fig. 7-4 Local resistance difference and ship motions ($\lambda/L=1.6$, fixed surge). (a)

108

$t/T_e=0$; (b) $t/T_e=0.25$; (c) $t/T_e=0.5$; (d) $t/T_e=0.75$

Fig. 7-5 The mean value, 1st and 2nd harmonic amplitude of local resistance

109

difference for fixed surge: (a) $\lambda/L=0.1810$; (b) $\lambda/L=0.6$; (c) $\lambda/L=1.1$; (d) $\lambda/L=1.6$

Fig. 7-6 Wave pattern for the four quarter encounter periods $t/T_e = 0, 0.25, 0.5,$

110

0.75 : (a) $\lambda/L=0.1810$; (b) $\lambda/L=0.6$; (c) $\lambda/L=1.1$; (d) $\lambda/L=1.6$

Fig. 7-7 Unsteady wave component ζ_u ($=\zeta - \bar{\zeta} - \zeta_s$; ζ : unsteady free surface

elevation; $\bar{\zeta}$: incident wave elevation; ζ_s : steady free surface elevation in calm

112

water) of the free surface elevation for four quarter encounter periods $t/T_e = 0,$

$0.25, 0.5, 0.75$: (a) $\lambda/L=0.1810$; (b) $\lambda/L=0.6$; (c) $\lambda/L=1.1$; (d) $\lambda/L=1.6$

Fig. 7-8 Fourier analysis of ζ_u for $\lambda/L=0.1810$, $A/L=0.002719$ and fixed surge. (a)

Mean value. (b) 1st harmonic amplitude of Cosine (left) and Sine (right)

113

component. (c) 2nd harmonic amplitude of Cosine (left) and Sine (right)

component.....

Fig. 7-9 Fourier analysis of ζ_u for $\lambda/L=0.6$, $A/L=0.009375$ and fixed surge. (a)

Mean value. (b) 1st harmonic amplitude of Cosine (left) and Sine (right)

114

component. (c) 2nd harmonic amplitude of Cosine (left) and Sine (right)

component.....

Fig. 7-10 Fourier analysis of ζ_u for $\lambda/L=1.1$, $A/L=0.009375$ and fixed surge. (a)

Mean value. (b) 1st harmonic amplitude of Cosine (left) and Sine (right)

114

component. (c) 2nd harmonic amplitude of Cosine (left) and Sine (right)

component.....

Fig. 7-11 Fourier analysis of ζ_u for $\lambda/L=1.6$, $A/L=0.009375$ and fixed surge. (a)

115

Mean value. (b) 1st harmonic amplitude of Cosine (left) and Sine (right) component. (c) 2nd harmonic amplitude of Cosine (left) and Sine (right) component.....

Fig. 7-12 Boundary layer represented by slices colored with axial velocity below $u/U=0.9$ for the four quarter encounter periods for $\lambda/L=1.1$, $A/L=0.009375$ and fixed surge. (a) $t/T_e = 0.01$; (b) $t/T_e = 0.277$; (c) $t/T_e = 0.455$; (d) $t/T_e = 0.813$

Fig. 7-13 Vortex behavior in stern flow: Q-criterion $q=400$ with axial velocity u/U_0 contour for the four quarter encounter periods for $\lambda/L=1.1$

Fig. 7-14 The comparison between CFD (fixed surge) and PIV (free surge): axial velocity contours and velocity vector at propeller plane ($x/L=0.98$) for the four quarter encounter periods for $\lambda/L=0.6$, $A/L=0.009375$, fully-loaded condition.....

Fig. 7-15 The comparison between CFD (fixed surge) and PIV (free surge): axial velocity contours and velocity vector at propeller plane ($x/L=0.98$) for the four quarter encounter periods for $\lambda/L=1.1$, $A/L=0.009375$, fully-loaded condition.....

Fig. 7-16 The comparison between CFD (fixed surge) and PIV (free surge): axial velocity contours and velocity vector at propeller plane ($x/L=0.98$) for the four quarter encounter periods for $\lambda/L=1.6$, $A/L=0.009375$, fully-loaded condition.....

Fig. 7-17 The comparison between CFD (fixed surge) and PIV (free surge) for $\lambda/L=0.6$, $A/L=0.009375$, ballast condition.....

Fig. 7-18 The comparison between CFD (fixed surge) and PIV (free surge) for $\lambda/L=0.9$, $A/L=0.009375$, ballast condition.....

Fig. 7-19 The comparison between CFD ($\lambda/L=1.6$, fixed surge) and PIV ($\lambda/L=1.5$, free surge), ballast condition.....

Fig. 7-20 Vortex behavior in one encounter period for $\lambda/L=1.1$ at fully-loaded

116

117

119

120

121

122

123

124

126

condition. (a) A/L=0.009375. (b) A/L=0.0046875.....	
Fig. 7-21 Circulation at propeller plane in one encounter period. (a) Fully-loaded condition. (b) Ballast condition.....	128
Fig. 7-22 Total velocities (ship speed+orbital velocities) at different lateral distances.....	130
Fig. 7-23 Volume average nominal wake velocities. (a) Fully-loaded condition. (b)Ballast condition.....	133
Fig. 7-24 The comparison of u_N by CFD and linear method.....	134
Fig. 7-25 Axial velocity distribution at propeller plane in calm water. (a) Fully loaded condition; (b) Ballast condition.....	135
Fig. 7-26 Fourier analysis on axial velocity distribution at propeller plane for fully loaded condition.....	136
Fig. 7-27 Fourier analysis on axial velocity distribution at propeller plane for ballast condition.....	137
Fig. 7-28 Thrust estimate in one encounter period.....	139
Fig. 7-29 Estimated local propeller performance in calm water. (a) Thrust. (b) Torque.....	139
Fig. 7-30 Estimated local propeller performance in waves for one-quarter encounter period. (a) Thrust. (b) Torque.....	140

CHAPTER 1: INTRODUCTION

The prediction of the added resistance of a ship in waves is essential to evaluate ship performance in seaway. Also, it is of interest as the main factor for the fuel consumption in seaway to meet the requirement for minimum energy efficiency level measured by an Energy Efficiency Design Index (EEDI) and Energy Efficiency Operational Indicator (EEOI) which are regulated by the International Maritime Organization's (IMO) Marine Environment Protection Committee (MEPC). Many approaches have been developed to predict and estimate the added resistance such as using experimental fluid dynamics (EFD) and potential flow (PF) and lately computational fluid dynamics (CFD). Since the added resistance has a second order nature and it is based on mean value of wave force, its value is relatively small compared to the amplitude of the excitation force (Faltinsen, 1990). Thus a high degree of accuracy is required both in the experiments and calculations. On the other hand, the studies of added resistance have shown the dependency on ship motion, ship speed, wave length, wave height, wave heading, hull form, bow shape and bow relative motion.

1.1 COMPUTATION METHODS OF ADDED RESISTANCE

1.1.1 Analytical method

Many efforts have focused on using both linear and nonlinear PF for added resistance. For linear potential flow, the added resistance force is estimated from velocity potential and fluid pressure solution corrected with the perturbation method to include the

higher order terms using pressure integration method (Havelock, 1942; Boese, 1970; Salvesen, 1978), momentum and energy method (Maruo, 1957 and 1963), and radiated energy method (Gerritsma and Beukelman, 1972). The pressure integration method is a near-field method which computes the added resistance from hydrodynamic pressure integration on the body surface using Bernoulli's equation, and a Taylor expansion of the pressure about the mean position of the ship. By only integrating along the non-shadow part of water-line in wave direction and ship motions neglected, Faltinsen's asymptotic formula was derived to consider wave reflection effect (Faltinsen et al., 1980). The other two approaches are far-field method computing the added resistance from the generated waves energy and momentum flux at infinity. The details of these methods and their implementations in the linear potential flow solvers are discussed in Faltinsen (1990). Base on the formula of these analytical methods, the ship motions are required firstly and provided by strip theory generally. Gerritsma and Beukelman's (1972) method (G-B method) has been preferred widely in literatures and performed better than the other methods.

Fujii and Takahashi (1975) investigated the increase of resistance due to the bow reflection in short waves. Based on Maruo's formula, the added resistance is divided into two terms approximately: one is the resistance due to ship motion and another one is due to bow reflection. An approximate calculation method for the part of added resistance due to bow reflection was proposed. To consider the effect of blunt bow, bluntness coefficients, reflection and ship advance speed were introduced. The experiments were conducted: a containership model at Froude number (Fr) 0.12 with different heading angles ($\mu=180^\circ\sim0^\circ$) and wave lengths ($\lambda/L=0.5\sim2.0$), and tanker model at $Fr=0.15$ and 0.25 with $\mu=180^\circ\sim135^\circ$ and $\lambda/L=0.3\sim1.5$. Heave and pitch were

considered. To improve the under-predicted added resistance of this work, Tsujimoto et al. (2008) proposed a correction based on semi-empirical formula considering effect of draft, frequency, advanced speed and bow bluntness. The computation and experiment of a wall-sided model ($Fr=0.3, 0.25$), containership and PCC (pure car carrier) with $Fr=0.2/0.25$, $\mu=0^\circ\sim40^\circ$ and $\lambda/L=0.3\sim2.0$ were presented.

Erb (1977) modified MIT 5-DOF seakeeping program. A 21,000 tons Mariner cargo vessel at 15 knots with $\mu=2^\circ\sim180^\circ$, and various speeds at $\mu=180^\circ$ was computed. Also the other analytical methods: a modified G-B method (Loukakis and Sclavounos, 1977) and Salvesen's method were compared for various heading waves with various speeds. Three methods agreed well with each other over the full speed range for the heading angles larger than 105° bow waves. Obvious disagreement occurred in the beam seas.

Wilson (1985) compared Joosen's (extended Maruo's), Salvesen's, Loukakis and Sclavounos, G-B and Faltinsen's method for a full scale ship with $CB=0.825$ at $Fr=0.145$, S60 ($CB=0.8$) at $Fr=0.147$ and a destroyer at $Fr=0.3$. Loukakis and Sclavounos's method for head and oblique seas provided the most acceptable results.

McTaggart (1997) used SHIPMO seakeeping code (strip theory) and proposed a near-field method for added resistance with a switch to consider short wave condition. For $\lambda/L<1$, the added resistance would be the maximum value between the method and Faltinsen's formula. S60 ($CB=0.6, 0.7$ and 0.8), a towed and self-propelled FFG7 frigate were calculated. For S60 ($Fr=0.266/0.283$ at head waves), the added resistance was over-predicted compared with EFD (Ström-Tejsen 1973). For FFG7 ($Fr=0.15/0.3$, $\mu=0^\circ\sim180^\circ$), the added resistance was under-estimated against (O'Dea and Kim 1981). The method only provided acceptable (positive) values for $\mu=0^\circ\sim45^\circ$ following waves.

Journee (2001) studied the verification and validation of the seakeeping program

SEAWAY (linear strip theory). The added resistance was calculated by G-B and Boese's method. Several experiments were referred: S60 with CB=0.6, 0.7 and 0.8 at Fr=0.15 (Ström-Tejsen, 1973), a fast cargo ship at Fr=0.15, 0.2, 0.25 and 0.3 (Gerritsma & Beukelman, 1972; Journée, 1976), and S-175 at Fr=0.15 for $\mu=180^\circ, 150^\circ, 120^\circ$ (Nakamura, 1976; Fujii & Takahashi, 1975). For following waves, Boese's method is better than G-B's which seems to be very sensitive to low encounter frequency. G-B method has a preference for low CB and Boese's method does for high CB. The under-predicted added resistance was addressed for short waves as the 3-D bow wave diffraction is dominant and not taken into account for the strip theory.

Arribas (2007) concluded that added resistance computation has great sensitivity to motion prediction. An accurate prediction of vertical motions is more important than developing more sophisticated added resistance theories. By using Mauro's, Boese's and G-B method and comparing with experiments, a fast cargo ship, S175 containerships and a ferry for various Froude number were studied for non-dimensional encounter frequency=1~6. The analytical methods, especially G-B method, are accurate enough from the practical point of view if used with a good calculation for motions.

Nabergoj and Prpic-Orsic (2007) pointed out ship geometry also impacts the ability of analytical methods for the added resistance. Different methods gave fairly different results for a Ro-Ro ship at 25 knots in head waves. Among Havelock, Maruo, G-B, and other empirical methods, G-B method provided a better prediction for almost all ship forms except for cruiser-stern ships with low CB. Maruo's formula gave accurate results only for cruiser-stern ships without large bulbous bows.

Ghani and Julait (2008) utilized G-B method for a 100m long product tanker model for Fr=0.21, 0.25 and 0.28 and $\lambda/L=1\sim 2$. EFD showed the added resistance increases

with model speed with the peak at $\lambda/L=1.5\sim1.6$. The predicted added resistance decreases with increasing speed before peak value ($\lambda/L=1.4\sim1.6$) but increases at and after peak value. It is about 33% under-estimated generally but difference is smaller at lower λ/L because G-B method includes diffraction effect.

Alexandersson (2009) proposed a simplified method for added resistance, and compared with EFD and the other analytical methods: G-B, Boese's method and Faltinsen's formula. S60, S-175 and a fast cargo ship for $Fr=0.15, 0.2, 0.25$ and 0.3 with $\mu=0^\circ\sim180^\circ$ were examined. G-B method and Boese's method provided quite similar results from head to beam waves. G-B method would meet a singularity in zero encounter frequency. Instead, Boese's method had no problem on this because encounter frequency is in the denominator of the equation. Faltinsen's formula obtained negative added resistance in following waves.

Bingjie and Steen (2010) combined G-B method and Faltinsen's formula to provide a better prediction of the added resistance for KVLCC2 in almost all wave length conditions. Compared with their EFD data, G-B method would under-predict the added resistance. Faltinsen's formula is limited by $L/\lambda\geq2$. Chuang & Steen (2011) showed the most severe speed loss and error between computation (G-B method) and experiment when the added resistance reaches its peak value at $\lambda/L\sim1$ for an 8000 DWT tanker at $Fr=0.212$ in wave lengths $\lambda/L=0.46\sim1.29$.

1.1.2 Unsteady wave pattern analysis and ray theory

In Naito (2001), the methods to estimate the added resistance and speed loss were surveyed. For the added resistance, the measurement, Maruo's formula, pressure

integration method, ray theory and unsteady wave pattern analysis were mentioned. The pressure integration method could predict the value close to the measurement. The far field method, Maruo's formula based on slender body theory, could be improved by the ray theory to capture the diffraction component of added resistance, and the non-uniform current and wave breaking region around the bow. The method also could be improved by including the unsteady wave component provided by unsteady wave pattern analysis. The studies about Wigley and ore carrier with different above-water hull form, and different bow shapes such as delta, blunt, sharp were introduced.

The ray theory (Whitham, 1960) was applied by Hermans (1991) to capture short wave pattern and consider general ship form and any wave direction. The added resistance was calculated by a pressure integration method. The results of modeling surface-piercing cylinder were compared with Faltinsen's formula. Later, this method was applied on S60 by Kalske (1998).

The unsteady wave pattern analysis and its development were also mentioned by Ohkusu (2004) to improve the analytical method for the added resistance. The analysis and measurement could be performed in parallel along with the ship course (longitudinal cut; used by Ohkusu, 2004; Kashiwagi, 2011) or in the downstream transversely to the ship direction (transverse cut; used by Gui et. al. 2000; Erwandi and Suzuki 2001; Naito, 2001). An amplitude function of propagating wave component to each direction from the ship could be obtained from the wave pattern analysis. Although the added resistance is a wave-making resistance, the value obtained from the wave pattern is much smaller than the one from the resistance measurement for the blunt bow form. The reason might be the interaction between steady and unsteady wave pattern. The incident waves measured in far-forward position was extrapolated to the

near field to obtain the unsteady wave pattern. Near the bow, the unsteady wave height computed by a Rankine panel method was much lower than the measured one.

For the diffraction wave (motion-fixed), Gui et al. (2000) conducted the experiment for the DTMB 5512 model in waves. Forces and moments were measured. The near- and far-field free surface elevations were recorded on a domain. Two maximum amplitudes of unsteady wave pattern were observed with around 40% of the 1st harmonic of unsteady free surface elevation. They initiate at the fore-body shoulder and transom corner and diverge with 24.5° from the center-plane. Instead of wave probe, Erwandi and Suzuki (2001) used CCD camera to record the wave profile image generated by a Wigely hull. The measurement was compared with Ohkusu's experiment and the computation by a slender body theory (with the modified amplitude function).

1.1.3 Advanced potential flow method

Following the development of more advanced PF method such as source distribution method, panel method and more recently enhanced unified theory (EUT), these linear seakeeping solvers were employed with the above-mentioned analytical methods to compute the added resistance. For some nonlinear solver developed such as LAMP-2, the first order and higher order solutions are not separated and they are solved through a single solution process. Contrary to strip theory, these PF methods could consider 3D flow field and complex ship geometry.

Chan (1990) used 3-D source distribution method for motions with a near-field method proposed for the added resistance. Several kinds of source were discussed: translating pulsating source with higher pitch damping, oscillating pulsating and

translating pulsating source. S60 with $CB=0.6, 0.7$ and 0.8 at $Fr=0, 0.2\sim0.3$ with $\mu=0^\circ\sim180^\circ$ were investigated and compared with EFD (Ström-Tejsen, 1973). The prediction of the added resistance in head waves is very sensitive to the heave and pitch motion responses in the region of resonances. Hulls with poor motion responses, particularly in pitch, would produce large added resistance. The 3-D flow close to ship bow should be considered in short waves. The rapid decay of small wave length might cause the asymptotic value of added resistance. Faltinsen's formula provided some promising results for ships with blunt ends but had large discrepancies for fine form ship at high speeds.

Kashiwagi (1995) developed EUT (enhanced unified theory) with a modified version of Maruo's formula to compute the added resistance and conducted the experiment. The effect of 3D diffracted wave at the bow is considered. For the SR221 at $Fr=0.15$ for fully-loaded and ballast condition in head waves, EUT (Kashiwagi, 2009) showed the good agreement with EFD for ship motions including the amplitudes and phases. The added resistance was predicted well for most of wave lengths by EUT except that $\lambda/L\leq0.65$ has smaller values than the measured one. The nonlinear effects of the geometry above this still water line which could not take into account in this linear theory caused error for large motions, for example, in ballast condition the surface piercing bulbous bow. For the ballast condition, although the motions were well-predicted but the computed added resistance was much smaller for $\lambda/L\leq1.2$. Kashiwagi (2011, 2013) included the unsteady wave pattern analysis into EUT for the modified blunt and slender Wigley hull at $Fr=0.2$. The cases were tested with motion-fixed, forced motion (heave and pitch), and free to surge, heave and pitch. The added resistance predicted by EUT using the superposed waves (motion-fixed+forced

motion) showed fairly good agreement with the value of pure EUT and measurement.

The values predicted using measured waves were smaller, especially for the peak of the added resistance because the non-linear local waves near the bow occur for the larger ship motion. The steady sinkage and trim should be considered for short waves.

Bunnik (1999) derived a linear discrete dispersion relation of the reflected and radiated waves by a Rankine source method. To consider the interaction between the steady flow around the ship and the incoming waves, the non-linear steady flow was solved by a potential flow code RAPID. The sources were distributed on the panels on the ship hull and free surface with constant strength. By the pressure integration method and perturbation theory, the force and moment including 1st and 2nd order component were obtained. A 125,000 m³ (273 m long) LNG carrier at Fr=0.14, 0.17 and 0.2 with $\mu=0^\circ$, 45° and 180° was modeled and compared with experiment. The ship motions were predicted precisely at moderate and high encounter frequencies except for the roll motion due to the lack of viscosity. In head waves and short waves, the prediction and measurement for motions and added resistance agreed well. The double-body and linear steady flow method under-predicted the added resistance largely. For long waves and oblique waves, the computational domain is not large enough to obtain efficient damping effect on the free surface.

Fang and Chen (2006) developed a 3-D nonlinear pulsating source distribution method with 6DOF ability. The nonlinear hydrodynamic forces including added resistance and lateral drifting forces were calculated by Salvesen's method. The test cases were Series 60 and Marine ship hull. Usually, the results of 3-D method were better than 2-D's, especially in short waves.

Liu et al (2010) used frequency domain 3D panel method with Maruo's method. And

Faltinsen's formula was for the short wave condition. A fixed half-immersed spheroid at $Fr=0$ and 0.2, and Wigley hull at $Fr=0.3$ were simulated. Several computations were executed and compared with EFD: S60 with $CB=0.6$ at $Fr=0.266$ and 0.283 (Ström-Tejsen, 1973), S-175 at $Fr=0.25$ and 0.3 (ITTC, 1987), and a bulk-carrier at $Fr=0.1$ and 0.15 (Kadomatsu, 1988). The result revealed fully satisfactory for the prediction of the added resistance of ships if the input motions are estimated accurately.

Joncquez et al. (2008) validated AEGIR (panel method) and the added resistance was computed by pressure integration and momentum conservation methods. A sphere at $Fr=0$, Wigley hull free to heave and pitch at $Fr=0.3$, S60 free to heave and pitch at $Fr=0.207/0.222$, and a Bulk carrier free to surge, heave and pitch at 14 knots were tested for the non-dimensional encounter frequency=2~8. It was found that both methods predict the added resistance well for most of the geometries except momentum conservation method underestimates for the bulk carrier. Good agreement with experiment data from existed literatures and G-B, Salvesen's, Faltinsen's method were presented. Good trend of the computed added resistance following the experiment data but with lower mean value was observed.

Lee (2008) investigated JHSS (Joint High Speed Sealift) free to heave and pitch at $Fr=0.24$ and 0.35 in regular head waves $\lambda/L=0.7\sim1.3$ by using several solvers. SWAN-1 is 3-D Rankine panel method and the added resistance is calculated by wake analysis. LAMP-2 is 3-D panel method with viscous correction and obtains the added resistance from time dependent surge forces. VERSE is G-B and pressure integration method. The computational results were compared with the experiment data. SWAN-1 provided the best prediction. Pitch RAO showed good agreement but heave RAO was over-predicted. The added resistance was under-predicted with the peak at larger λ/L . LAMP-2

over-predicted heave and pitch motions but under-predicted the added resistance. VERES result showed G-B method provides good agreement.

Zhang et al. (2009) validated the prediction of added resistance using both LAMP-1 and LAMP-2 and proposed the formulation for LAMP-4. LAMP-1 is a linear potential code, LAMP-2 is approximate nonlinear code for which the hydrostatic and Froude-Krylov forces are applied on the instantaneous wetted surface of the body, and LAMP-4 includes the highest nonlinearity level with the boundary conditions applied on the instantaneous position of free surface and body. Both LAMP-1 and LAMP-2 showed very similar results for vertical motions. For both solvers, the added resistance and its peak were under-predicted for S60 (CB=0.7) at Fr=0.3 against EFD (Ström-Tejsen, 1973) and over-predicted for Wigley hull at Fr=0.207 against EFD (Journee 1992).

Kim et al. (2010) applied WISH and AEGIR for two different Wigley hull at Fr=0.2 and 0.3, and S60 (CB=0.7) at Fr=0.222 and S175 containership. Both are B-spline based Rankine panel method. The added resistance is computed by pressure integration method. It showed that among the components of added resistance, radiation is much larger than diffraction around $\lambda/L \sim 1$ but diffraction was slightly larger in shorter and longer waves. 2nd-order forces oscillate two times faster than the linear force. The added resistance should be the mean value of the 2nd-order forces. For the free surface treatment, Neumann-Kelvin linearization based on thin-ship theory had good results for Wigley hull form, but double-body method is better for larger beam-to-length ship.

Duan and Li (2013) used an extended integral equation method based on mixed source and doublet distribution without the irregular frequency effects to solve hydrodynamic coefficient. The G-B method is applied to compute the added resistance and combined with an approximated formula based on reflection law for short waves.

S-60, S-175 and KVLCC2 were tested and compared with the other methods and experiment. The method provided better results for short waves and fine hull ship.

1.1.4 CFD

By solving Reynolds average Navier-Stokes (RANS) equations, CFD has the advantage of predicting added resistance and ship motions by performing nonlinear computation without using an analytical formula for added resistance or empirical values for viscous effect, but it is considerably more expensive than PF approaches. Orihara and Miyata (2003) validated WISDAM-X for added resistance and motions for SR108 container and showed a long and protruding bow reduces the added resistance. Simonsen et al. (2008) conducted simulations for KCS container using CFDShip-IOWA showing good prediction for the motions but mean and 1st harmonic amplitude of the resistance was predicted by 24%D and 80.6%D, respectively. Castiglione et al. (2009) studied the added resistance and response of high speed Delft catamaran in head waves for several ship speeds by CFDShip-IOWA. A peak was observed for motions at the resonant frequency for all speeds. The peak increases with speed, reaching their maximum at the highest speed. Orihara (2011) applied WISDAM-X to predict sea-keeping performance for SR221C tanker under fully-loaded and ballast condition in regular head waves at $F_n=0.150$. The results agree well with the experiment for unsteady surface pressure on the bow, added resistance and ship motion. For ballast condition in $\lambda/L=1.0$, the bow bulb is fully submerged with higher pressure on it and also emerged exposing the bow bottom.

The added resistance of KVLCC2 in head waves is studied as one of the Gothenburg

2010 workshop test cases by Deng et al. (2010), Moctar et al. (2010) and Sadat-Hosseini et al. (2010a). Deng et al. (2010) predicted the added resistance and motions for $\lambda/L=1.1$ and 1.6 by average of $E=17.7\%D$ using ISISCFD RANS solver. The verification study and validation for more wave length conditions were later reported in Guo et al. (2012) which showed good prediction of the motions and the added resistance for all of the wave length conditions studied there. Moctar et al. (2010) validated only the motions for $\lambda/L=0.6$, 1.1 and 1.6 predicted by OpenFOAM and Comet RANS codes. The simulations with free surge were also conducted using Comet. Sadat-Hosseini et al. (2010a) predicted the added resistance and motions for KVLCC2 at $Fr=0.142$ using CFDShip-Iowa V4.5, an Unsteady Reynolds Average Navier-Stokes (URANS) code, for long wave region for both fix and free surge and the preliminary results were compared against available EFD data.

Weymouth et al. (2005) implemented the 6DOF solver in CFDShip-IOWA. The free surface is modeled by a surface tracking method (moving boundary) to predict the pitch and heave for a modified Wigely hull in head seas. $Fr=0.2, 0.3, 0.4$; $\lambda/L=0.75\sim2.0$. The verification and validation study was performed. The average error for forces and motions is less than 2% compared with the experiment (Journee, 1992). Unsteady wave pattern and unsteady boundary layer were analyzed. As Gui et al. (2000) observed, the shoulder and trailing edge waves formed with the maximum and 1st harmonic amplitude which is around 197% of the incident wave height. The 2nd harmonic has much smaller amplitude (49%) and shares the similar pattern with the 1st harmonic.

Bunnik et al. (2010) compared the several different methods including linear PF solvers based on strip theory, source distribution method, panel method and CFD. The results were compared with the experiment for the ship motion, added resistance,

internal loads and relative vertical motions. A 270m long containership (1/50 model) with CB=0.598 at 24.5 and 27 knots and 173m long ferry (1/36 model) with CB=0.541 at 25 knots were tested in head seas. The methods based on strip theory could obtain reasonable prediction for ship motions for traditional ship forms with $L/B > 5$ but less accurate for the added resistance. CFD did not provide better results than the best linear PF codes. The added resistance is under predicted by most of the solvers except for a CFD code. Heave motion is more difficult to predict accurately than pitch motions.

Nordas (2012) investigated the optimal bow ship for large slow ship. The viscous effect was simulated by CFD solver Shipflow and the free surface effect is modeled by a Rankine panel code XPAN. A variation of KVLCC2 with different bow shape is tested. The sharper bow has significantly lower added resistance in the diffraction regime. The innovative bow shapes for the reduction of added resistance were reviewed: X-BOW, a STX OSV's new design, BEAK-BOW, AX-BOW and LEADGE-BOW.

Ye et al. (2012) developed a URANS solver based on OpenFOAM. A wave generation/damping module and 6DOF solver using dynamic deformation mesh were also developed. The S-175 containership free to heave and pitch in $\lambda/L = 0.8-1.5$ was simulated and compared with the experiment (Fujii and Takahashi, 1975) and the results by G-B and Boese method (Journée, 2001). The CFD performed better accuracy than the strip theories and could predict large ship motions with strong nonlinearity which reveals in the 2nd harmonic component.

1.2 THE DEPENDENCE OF ADDED RESISTANCE

Some major trends of the added resistance has been studied by Blok (1983) by

experiment, including the influence of length/frequency, height, heading of waves and the speed, size, main particulars and hull form of ships. The relation among relative motion, dynamic swell-up and the added resistance were investigated too.

1.2.1 Ship motions and maximum forces/moment responses

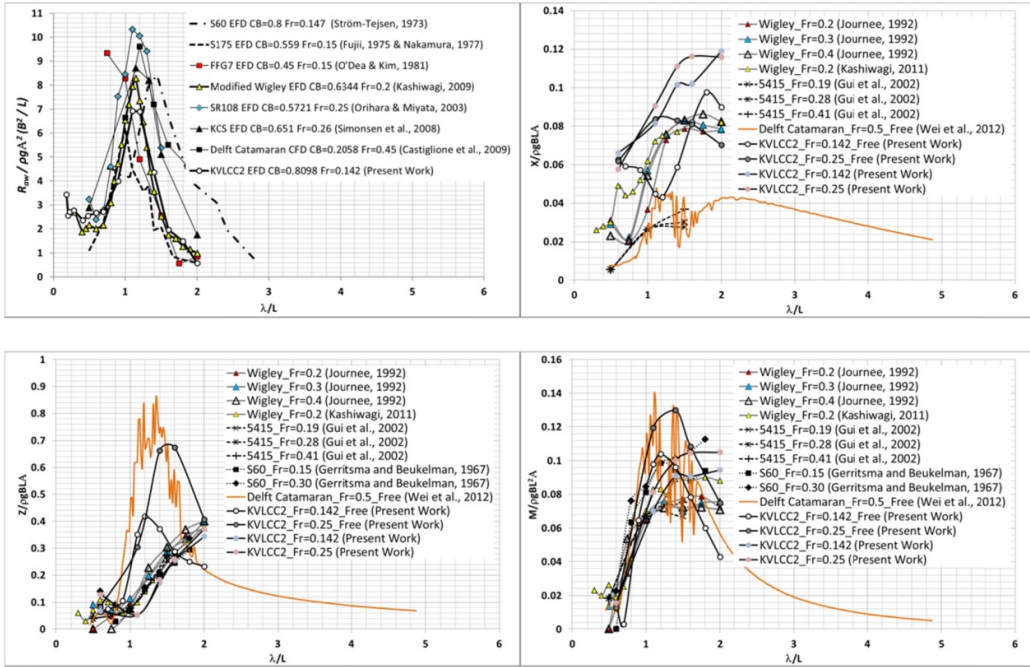


Fig. 1-1 Review of added resistance and surge, wave excitation total forces and moments for fixed/free ship in head waves for different geometries.

Generally, ship motions have been considered as the major origin of added resistance in long wave region. In short waves, the added resistance is caused by wave reflection mainly. The added resistance reaches the peak when the heave and pitch responses are relatively large, i.e. the corresponding wave frequency is near the resonance condition (equal to motion natural frequency), refer Figure 1-1. The data existed in literatures are

collected in the figure including CFD and EFD (Ström-Tejsen, 1973; Fujii, 1975; Nakamura, 1977; O'Dea and Kim, 1981; Orihara and Miyata, 2003; Simonsen et al., 2008; Castilion, et al., 2009; Kashiwagi, 2009; present work). The wave excitation surge force (X) / heave force (Z) / pitch moment (M) are large which happens at $\lambda=1.33L$ for pitch and very long waves for heave, and is fairly independent of ship speed and ship geometry (CB, block coefficient), see Table 1-1. The data, including CFD and EFD, existed in literatures are collected in the figure (Journee, 1992; Kashiwagi, 2011; Gui et al., 2002; Wei et al., 2012; present work).

Erb (1975)'s computation and experiment reported that the added resistance peak can be seen that all the significant motion-related second-order force component peak at one place (generally near the heave or pitch resonance, respectively). This peak is present for all heading angles, although its location varies, depending primarily on the location of heave and pitch peaks in bow and beam waves. Dallinga et al. (2008) used a numerical method for a 180m long ferry with typical bow flare considering pitch motion at 20 knots. A peak of the added resistance coincides with relatively high pitch response. Fang and Chen (2006) computed a Marine ship hull for $Fr=0.194, 0.266$ and 0.283 and showed the maximum value of added resistance usually coincides with the heave resonance observed around $\lambda/L=0.65$.

In the experiment in Joncquez et al. (2008), a model of Bulk carrier with $CB=0.814$ free to surge, heave and pitch was tested. The small influence of surge motion on the added resistance coefficient is mentioned. However, Kashiwagi (1995) addressed that the prediction considering surge motion is still of importance as the motions might be slightly influenced by coupling with heave and pitch.

Table 1-1 Added resistance and ship motions for different geometries.

	C_B	Fr	RAO _{max}				f_n (Hz) (ave. f_e)	
			RAO		at λ/L	f_e (Hz)	f_{n_heave}	f_{n_pitch}
SR221C (Kashiwagi, 2009)	0.803	0.15	z/A	1.1283	1.3	0.5386	0.5386	0.4736
			θ/AK	1.0692	1.6	0.4736		
			C_{aw}	6.9244	1.2	0.5663		
Delft Catamaran (Castiglione et al., 2009)	0.2058	0.45	z/A	2.1667	1.201	1.3367	1.2910	1.1728
			θ/AK	1.3134	1.397	1.1929		
			C_{aw}	9.6136	1.201 [‡]	1.3367		
		0.6	z/A	2.6444	1.6	1.2484		
			θ/AK	1.7015	1.795	1.1429		
		0.75	z/A	2.7333	1.806	1.2878		
			θ/AK	1.6007	2.012	1.1827		
KCS (Simonsen et al., 2008)	0.651	0.26	z/A	1.1093	1.33	0.81	0.8633	0.75
			θ/AK	1.052	1.5	0.75		
			C_{aw}	8.7172	1.15	0.9		
		0.33	z/A	1.4695	1.33	0.89		
			θ/AK	-	-	-		
			C_{aw}	8.0889	1.33	0.89		
		0.4	z/A	1.5488	1.5	0.89		
			θ/AK	-	-	-		
			C_{aw}	4.9019	1.5	1.08		
SR108 (Orihara and Miyata, 2003)	0.5721	0.25	C_{aw}	10.3230	1.1	1.9032	1.8096	1.4287
		0.275	z/A	1.3175	1.2471	1.8096		
			θ/AK	1.2068	1.7646	1.4287		
			C_{aw}	11.1367	1.2	1.8584		
		0.3	C_{aw}	12.2706	1.2	1.9237		
Blunt modified Wigley (Kashiwagi, 2010)	0.6344	0.2	C_{aw}	8.2803	1.15	1.0814	-	-
S175 (Kim et al., 2010)	0.561	0.15	C_{aw}	5.7347	1	0.1300	-	-
		0.2	C_{aw}	7.5989	1.1	0.1223	-	-
		0.25	C_{aw}	10.0698	1.25	0.1129	-	-
FFG (McTaggart, 1997)	0.45	0.15 (towed)	C_{aw}	-	-	-	-	-
		0.3 (towed)	C_{aw}	15.2532	1	0.1620	-	-
		0.3 (propelled)	C_{aw}	14.8523	1	0.1620	-	-
S60 (McTaggart, 1997) (Zakaria and Baree, 2008)*	0.6	0.25	C_{aw}	8.5321	1.18*	0.1642	-	-
		0.266	C_{aw}	8.9506	1.2	0.1761	-	-
		0.283	C_{aw}	9.3930	1.24	0.1625	-	-
	0.7	0.207	C_{aw}	8.1704	1.24	0.1625	-	-
		0.222	C_{aw}	9.1054	1.3	0.1580	-	-
		0.25	C_{aw}	10.547	1.24*	0.1588	-	-
	0.8	0.147	C_{aw}	7.9068	1.31	0.1561	-	-
		0.165	C_{aw}	8.0092	1.37	0.1517	-	-
		0.25	C_{aw}	15.647	1.25*	0.1580	-	-

‡ Only CFD data of Fr=0.45 available; others are based on EFD data.

1.2.2 Ship speed/Froude number

The added resistance increases as the ship speed increases and its peak moves to longer waves, see Figure 1-1.

Erb (1975) revealed higher forward speed increases the peak of drift force and added resistance, and shifts it to longer wavelengths. Chan (1990)'s computation showed that the peaks of heave and pitch amplitude, and added resistance increases with increasing speed and occur in longer waves.

Zeraatgar & Abed (2006) applied G-B method to the MARINER ship in regular and irregular waves for $Fr=0.194$ and 0.252 . The ship motions (heave and pitch) were calculated by STATEK computer program. The added resistance and drift force in different heading angles increase by increasing ship speed.

The experiment presented in Lee (2008) for JHSS free to heave, pitch and roll at $Fr=0.24$ and 0.35 showed higher speed has larger added resistance. In Ghani and Julait (2008), EFD showed the added resistance increases with model speed. The peak occurs at $\lambda/L=1.5\sim1.6$.

1.2.2 Heading angle

The added resistance is often larger in head waves than that in beam waves. And the heading would change the encounter frequency i.e. the location of the peak of the added resistance shifts.

Fujii and Takahashi (1975) also conducted the experiment of added resistance in regular oblique waves. In head or bow wave with incident angle from 180° to 120° , the

resistance increases. It might be caused by larger disturbance due to ship motion. However, in beam or following waves with incident angle from 90° to 0°, the resistance increases is considerably small.

Zeraatgar & Abed (2006)'s computation for $\mu=180^\circ, 150^\circ, 120^\circ, 105^\circ$ showed The added resistance increases rapidly as increasing $\mu=120^\circ$ to 150° , but the drift force decreases rapidly. In $\mu=180^\circ$, the largest added resistance appeals but drift force is close to zero. In $\mu=90^\circ$, the largest drift force occurs but added resistance is about zero.

Dallinga et al. (2008)'s numerical results concluded with heading angle, the transverse drift forces induce drift angle. The bulb bow might not be in the design draft and generates different bow wave pattern. The influence of drift angle on the added resistance in head waves is less than that in oblique waves.

Grigoropoulos et al. (2000) used a modified G-B method (Loukakis and Sclavounos, 1978) and derived an experimental formula to S60 (CB=0.7) against EFD (Vossers et al., 1960) at $Fr=0.2$ for $\mu=90^\circ \sim 180^\circ$. The added resistance of $\mu=170^\circ$ has larger maximum value and the whole distribution shifted to longer wave length against the 130° one. Heave, pitch and bending moment resonance occurs about $\mu=100^\circ, 90^\circ$ and 90° respectively. For lower sea states, the added resistance increases as the heading angle increases. For higher sea states, largest value is at $\mu=180^\circ$.

In Journee (2001), the computation and the experiment of S-175 container ship at $Fr=0.15$ referring Nakamura (1976), Fujii and Takahashi (1975) showed the added resistance decreases as the heading angle decreases from $180^\circ, 150^\circ$ to 120° . The computational result in Duan and Li (2013) indicated that the peaks of added resistance occur at shorter wave length and become smaller for larger heading angles.

1.2.4 Wave length and amplitude

For added resistance problem, the wave length (λ) and wave height(H)/amplitude(A) is related because both decide the wave steepness ($2A/\lambda = H/\lambda$). $H/\lambda < 1/7$ would cause nonlinear effect, such as a local stagnation point at a sharp crest and trochoidal wave profile (Newman, 1977). If $H/\lambda < 1/10$, the waves would break.

Fujii and Takahashi (1975) revealed effect of bow reflection decreases as λ/L decreases (1.5~0.3). The effect of ship motion rises when wave becomes longer. Journee (1976) showed in regular following waves, the added resistance has quadratic dependence on wave amplitude. For different wave amplitude, motions change linearly but phase differences between motions and waves have no influence.

Journee (1976) used G-B method to calculate the added resistance of a fast cargo ship in regular head waves and following waves in two separate reports. Heave and pitch motion was considered. $Fr=0\sim0.3$ and $\lambda/L=0.5\sim2.0$. Two kind of condition was tested: the model overtakes the waves or the waves overtake the model. The results had good agreement with the experiment data conducted in the study. The relation between ship motion and wave amplitude is linear. Phase differences between the motion and waves are constant for different amplitude. The added resistance varies as the square of wave amplitude.

Fang and Chen (2006) computed S60 at $Fr=0.194$ with $\mu=30^\circ, 60^\circ, 90^\circ, 120^\circ$ and compared with EFD (Ström-Tejsen, 1973). For stern quartering waves the mean lateral drifting forces increase with the decreasing wave lengths.

Joncquez et al. (2008) revealed that the choice of the amplitude used for normalization (min., max. and RMS amplitude) has huge influence on the added

resistance coefficient, especially around the encounter frequency corresponding to the ship's heave resonance.

Bingjie and Steen (2010) showed the existence of some error and uncertainty caused by very short wave condition ($\lambda/L=0.181\sim0.917$). The high steepness causes Benjamin-Feir instability and wave amplitude decreases as propagation. However, to avoid that, keeping very small wave amplitude during the measurement is very difficult. The error of oscillating at low frequency was eliminated by running many time windows and averaging the values. The uncertainty analysis of was 0.296% for one time window and 0.196% for 1000 time windows.

The experiment of $A=2.1\sim4.6\text{cm}$ for a 7.32m long SR221C ship model was recorded in Kashiwagi (2009) in short wave region. The differences seem to be more obvious in the added resistance than motions. Kashiwagi (2011) showed the main difference between two wave amplitudes for the slender and blunt Wigley hull is around the peak of the added resistance.

1.2.5 Ship geometry

The hull form with larger block coefficient (CB) has larger added resistance with a peak shifted to longer waves as large block coefficient reduces heave and pitch natural frequencies (see Table 1). Zakaria and Baree (2008) who discussed the effect of block coefficient on the added resistance for Series 60 ship hull with $CB=0.6, 0.7, 0.8$ and showed that increasing the block coefficient increases the added resistance. Since increasing CB reduces the vertical motion natural frequency, lower speed is required to have an encounter frequency close to the vertical motion natural frequency. Therefore

the low CB geometries such as Catamaran have the peak of the added resistance in wave region of $\pi/L=1.2\sim1.4$ at higher speed compared to the other geometries.

Besides CB, the hull form at fore and aft might change the added resistance. The blunt bow shape generally provides larger added resistance. Blok (1983) found that the added resistance of the ship with blunt bow is generally larger than that for the ship with wedge or fine bow.

Ogiwara and Yamashita (1996) found that the added resistance owing to diffraction of waves on the bow is attributed to a pressure increase on a very narrow area of hull surface along the wave profile in steady state. With 20~30% reduction for the added resistance in regular head waves, BEAK-BOW was proposed by Matsumoto et al. (1998) for tanker and bulk carrier. Later Matsumoto (2002) proposed an energy-saving bow shape called AX-BOW. The sharpened bulb bow could reduce the added resistance by 20~30% for the whole range of wave lengths. The full scale measurement was conducted on a 289m long 172,000 DWT Cape size bulk carrier. Nordas (2012) also reviewed those new bow designs and concluded the sharper bow has lower added resistance.

Naito et al. (1996) introduced two above-water bow shapes to reduce added resistance in waves. The mechanism of the reduction of added resistance with changing the above-water bow shape was explained. Naito (2001) mentioned the effect of above-water hull form and stem line. The model with strong flare has larger added resistance than that with wall side. The EFD data of the added resistance for a ship hull with different bow forms and concluded that the ship hull with blunt bow shape has the largest added resistance while the sharp bow provides the minimum added resistance. He also showed that the effects of bow shape on the motions are negligible.

Orihara and Miyata (2003) presented the EFD data of the added resistance for a

medium-speed tanker with the conventional rounded bow and with long and protruding bow above the still waterline. The results indicated no significant change for motions while smaller added resistance for protruding bow shape was observed.

The importance of bow shape to PF computation for the added resistance has been also addressed. Chan (1990) suggested that 3-D flow close to ship bow should be considered in short waves. McTaggart (1997) suggested a bow-swell-up correction related to ship forward speed is required for the computation of fine hull form ship (strip theory and a near-field method for added resistance). For transom stern ship, the correction is needed rather than full transom one. Joncquez et al. (2008) reported the dominant source of added resistance is from the fat and flat bulb bow. Kashiwagi (2009) mentioned that the piercing bulb bow of a KVLCC2 in ballast condition causes non-linearity.

1.2.6 Relative motion

The bow relative motion has correlation with the added resistance such that the peak of the added resistance is near the maximum bow relative motion. Blok (1983) discussed the EFD data of the added resistance for several geometries and concluded the upper bow segment which becomes alternately wet and dry due to its large relative motion contributes most to the added resistance while stern contributes very little. He pointed out that for the high speed crafts the “swell-up” caused by very high pressure at bow is significant and should be considered in computing the added resistance. Grigoropoulosa et al. (2000) presented the EFD data of the added resistance for Series 60. The bow relative motion was also reported to evaluate the possibility of deck wetness and

slamming. Comparing the added resistance and bow relative motion reveals the strong correlation between them and the important role of bow on the added resistance. Kashiwagi et al. (2004) also showed that the peak value of non-dimensional bow relative motion reduces by increasing wave height.

1.2.7 Propulsion and nominal wakes in waves

As discussed above, the studies of added resistance have focused on ship bow for the long history. The blunt bow shape generally suffers larger added resistance. The peak of the added resistance is near the maximum bow relative motion, and the wave length around one ship length, and heave natural frequency. Few studies considered propulsion. McTaggart (1997) presented the added resistance for a towed and self-propelled FFG-7 frigate model at $Fr=0.3$ and concluded that the self-propulsion would not influence the added resistance much.

The modern ships always are driven by the propeller operating at stern in waves. The importance to understand the propeller performance in waves has been stressed. Nakamura et al. (1975) conducted the self-propulsion experiment in irregular head waves for a single screw high speed container. The inflow velocity at the propeller plane was measured by a ring type wake meter. The propeller performance also was calculated by the blade element theory using the measured inflow velocity. The added resistance and RAOs in irregular waves could be estimated by the linear superposition of the data from regular waves. Kashiwagi et al. (2004) developed an analysis system based on EUT to estimate the propeller performance in waves. The RAOs in frequency domain, relative height, added resistance, steady lateral force and yaw moment could be

predicted firstly. By using those results with a wave spectrum, the ship speed loss in irregular waves could be calculated. Good prediction was presented compared with the data from experiment, speed trail and actual voyages.

However, very few studies discuss the wake field the propeller works inside in waves in detail. The wake profile and behavior would influence the propeller performance definitely. Tsukada et al. (1997) measured the unsteady ship wakes in regular waves by a five Pitot tube system for future CFD validation. The ship was towed in heave and pitch free, and motion fixed condition in wave length $\lambda/L=1$ and 0.5, and a forced pitch condition in calm water. The change of wake fraction and mean circulation in one encounter period were presented. The wake factor increases because of larger ship motions in longer waves. In short waves, the main influence is from incident wave number. The wave factor change due to motion free in one encounter period could be explained by the superposition of the motion fixed and forced pitch condition. Ueno et al. (2013) conducted the free running test for a 4m long container ship model (CB=0.65) with rudder in regular and irregular waves at $Fr=0.158$ and 0.223. The wake velocity was measured by vane-wheel current meters. The thrust and torque measured by dynamometer in waves vary by time. A strip method to estimate inflow velocity and ship motions from thrust and torque in waves was proposed. The relative longitudinal flow velocity measured and estimated were compared and discussed. It revealed that the effective wake coefficient in regular waves is higher than that in calm water for all wave length $\lambda/L=0.4\sim3.0$. The difference increases as heading angle increases from 0° to 180° .

CHAPTER 2: EFD METHODS

2.1 SHIP GEOMETRY

The experiments and simulations are conducted for bare hull KVLCC2 appended with propeller shaft. The experiments are provided mainly by OU (Osaka University) in free surge condition including fully loaded and ballast condition. For fully loaded condition, the data from INSEAN (Italian Ship Research Institute) is for fixed surge condition and NTNU (Norwegian University of Science and Technology) is for short wave condition. OU and INSEAN use a model manufactured of wood with scale ratio of 1/100. The main particulars of the ship model are shown in Table 2-1. The experiment conducted by NTNU uses larger model with 1/58 scale ratio. For CFD simulations, the model with scale ratio of 1/320 is employed. The CFD model includes the propeller shaft similar to EFD models. The body plan of the model in fully-loaded and ballast condition is shown in Figure 2-1. The coordinate system is located at center of gravity, with x pointing toward the aft (positive downstream), y to starboard and z upward.

2.2 OSAKA UNIVERSITY

The free surge tests are conducted in Osaka University towing tank. The tank is 100 m long, 7.8 m wide and 4.35 m deep. It is equipped with a drive carriage (7.4m in length, 7.8m in width, and 6.4 m height) running from 0.01 to 3.5 m/s. It is also equipped with plunger-type wave maker generating regular and irregular waves up to 500 mm wave height and wave length of 0.5 to 15m. The wave absorber is a small fixed gridiron beach

Table 2-1 Ship model properties (OU 1/100 model).

		Fully-loaded cond.	Ballast cond.
Length between perpendiculars	L_{PP} (m)	3.200	
Beam	B_{WL} (m)	0.580=B	
Depth	(m)	0.30	
Draft	T (m)	0.208	$T_F=0.067$ $T_A=0.119$
Displacement	V (m^3)	0.313	0.126
Longitudinal center of buoyancy	LCB(% L_{PP}), fwd+	3.48	-0.923
Vertical Center of Gravity (from keel)	KG (m)	0.186=KG _D	0.75KG _D
Radius of gyration	K_{XX} (m)	0.4B	
	K_{YY} (m)	0.25L _{PP}	
	K_{ZZ} (m)	0.25L _{PP}	
Block coefficient	C_B	0.8098	0.5725
Mid-ship section coefficient	C_M	0.9980	0.8245
Water plane area coefficient	C_W	0.9000	0.8218

* INSEAN model scale: 1/100; NTNU: 1/58

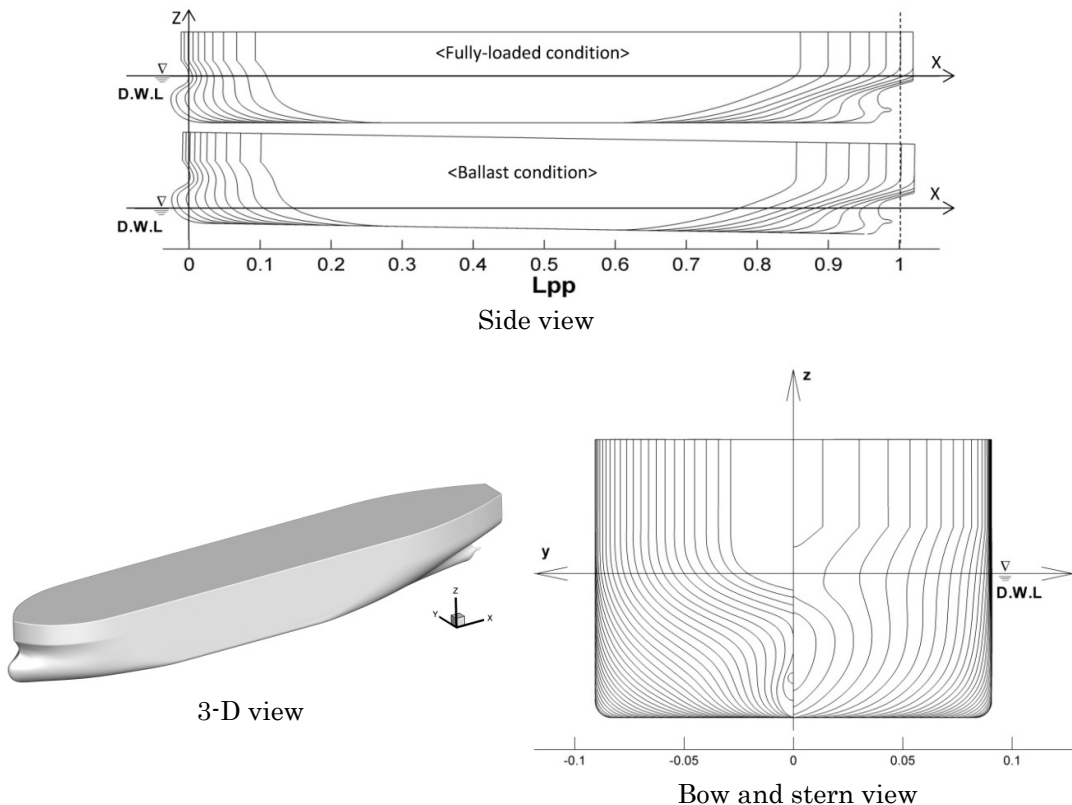


Fig. 2-1 KVLCC2 body plan and hull form.

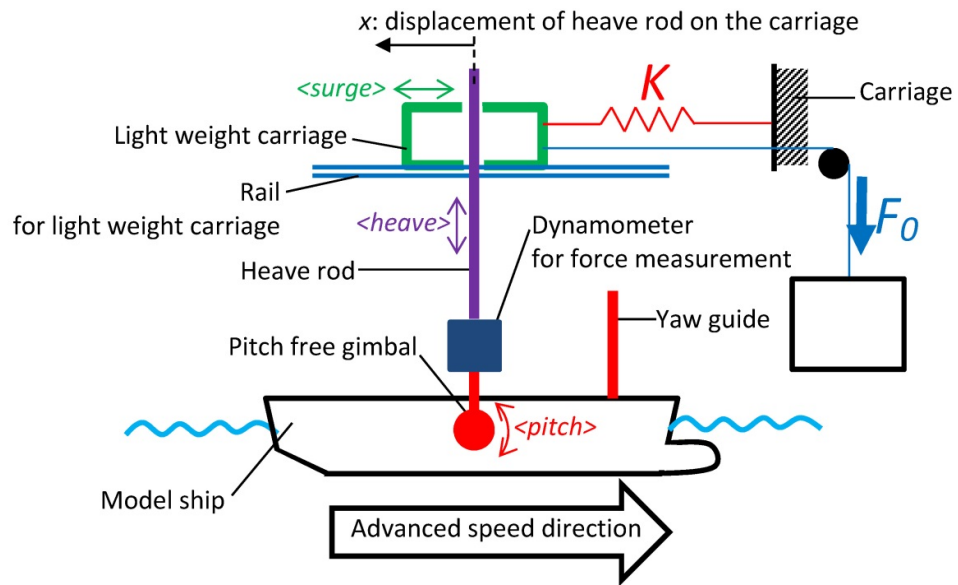


Fig. 2-2 Test setup for free surge condition.

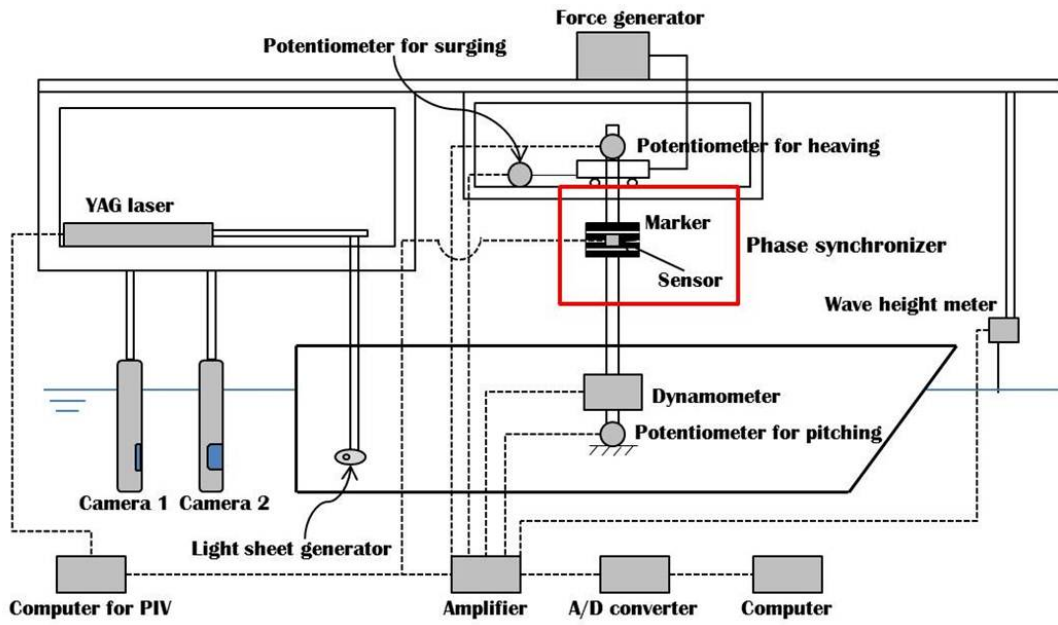


Fig. 2-3 PIV system.

at the basin's end, with movable beaches along its sides. The model is towed with a light weight carriage connected to the main carriage by mean of a spring to allow the model to be free in surge motion while it is free to heave and pitch, as shown in Figure 2-2. Note that the towing method of the model might be important to study not only the added resistance but also the speed loss (Minsaas and Steen, 2008). The 2-D Particle Image Velocimetry (PIV) system is used to measure the velocity distribution at propeller plane (Figure 2.3; Hayashi, 2012). Three potentiometers are to record heave and pitch motion respectively. Incident wave elevation is measured by a wave height meter.

The experiments are carried out at $Fr=0.142$ in calm water and in head waves with $\lambda/L=0.6\sim 2.0$ for fully-loaded condition and $\lambda/L=0.3\sim 2.0$ for ballast condition. The test condition is shown in Table 2-2 in detail. By considering the wave steepness $h/\lambda \leq 1/30$, wave amplitude is $A/L=0.009375$ for most of the wave lengths. And to keep the wave height during propagating, smaller wave amplitude is chosen: $A/L=0.005\sim 0.008281$ for the short wave region ($\lambda/L=0.3\sim 0.5$) in ballast condition.

During the test, the external force F_0 is used to avoid large stretch for spring. An appropriate spring stiffness K and F_0 are found based on the analytical solution of the following 1DOF surge equation:

$$m\ddot{x} = X - Kx - F_0 \quad (1)$$

Herein X is the hydrodynamic force, and x is the surge motion and m is the total mass of the moving parts including the model, hull and pitch free gimbals, dynamometer and light weight carriage. The mass of the model including hull and pitch free gimbals is $m_1=306.2$ Kg. The mass of the dynamometers and light weight carriage are $m_2=6.4$ Kg and $m_3=2.5$ Kg, respectively.

Table 2-2 EFD and CFD test conditions.

Fully-loaded condition								
EFD	OU	INSEAN	NTNU	CFD				
model scale	1/100	1/100	1/58	1/320				
DOF*	3	2	2	2	3	2	1, 2	I, 0
Fr	0.1422	0.1422	0.1422	0.1422	0.1422	0.25	0 (0.1422)	a:0.1422 b:0.25
Re $\times 10^6$	2.546	2.546	5.763	a: 5.763 b:5.763 c:2.546	2.546	4.482	0 (2.546)	a:2.546 b:4.482
λ/L	Calm 0.6 0.7 0.9 1.1 1.2 1.4 1.6 1.8 2	Calm 1.1 1.6	Calm a: 0.1810 0.2042 0.2289 b: 0.2289 0.2833 0.4077 0.4782 c: 0.2833 0.4077 0.4782 0.6365 0.8170 0.9174	a: 0.1810 0.2042 0.2289 b: 0.2289 0.2833 0.4077 0.4782 c: 0.2833 0.4077 0.4782 0.6 1.1 1.2 1.4 1.6 1.8 1.6 2 d: 0.6365 0.8170 0.9174	Calm 0.6 0.7 0.9 1.1 1.2 1.4 1.6 1.8 2	Calm 0.6 0.7 0.9 1.1 1.2 1.4 1.6 1.8 2	Calm * Natural frequency	Calm * DOF=I: Radiation *DOF=0: Diffraction
A $\times 10^{-3}/L$	9.375	9.375	a:2.72 b:4.53 c:9.375 d:4.6875	a:2.72 b:4.53 c:9.375 d:4.6875	9.375	9.375	-	-
Ballast condition								
EFD	OU			CFD				
DOF*	3			2	3		2	
Fr	0.1422			0.1422	0.1422		0 (0.1422)	
Re $\times 10^6$	2.546			2.546	2.546		0 (2.546)	
λ/L	Calm a:0.3 b:0.4 c:0.5 d: 0.6 0.7 0.9 1.1 1.2 1.4 1.6 1.8 2			Calm 0.3 0.6 0.9 0.9 1.1 1.1 1.6 1.6 2.0	0.6 0.9 1.1 1.6 2.0	Calm * Natural frequency		
A $\times 10^{-3}/L$	a:5.0 b:6.719 c:8.281 d:9.375			9.375	9.375			

* 0: no motion; 2: heave and pitch; 3: heave, pitch and surge; I: imposed heave and pitch.

The hydrodynamic force X can be assumed a linear superposition of added mass force, resistance in calm water, added resistance in waves and wave force.

$$X = -m_x \ddot{x} + R_C + R_{AW} + F_w \cos(\omega_e t) \quad (2)$$

Here m_x denotes the added mass, R_C the resistance in calm water, R_{AW} the added resistance in waves, F_w the amplitude of total wave force, ω_e the encounter frequency, and t is time.

Since the surge velocity is very close to carriage speed U_0 , resistance force can be evaluated from resistance coefficient (C_T) at carriage speed:

$$R_C = 1/2\rho A_W (-U_0 - \dot{x})^2 C_T \cong \underbrace{1/2\rho A_W U_0^2 C_T}_{R_{C0}} + \rho A_W U_0 C_T \dot{x} \quad (3)$$

Herein R_{C0} is the resistance in calm water for the model advancing at speed U_0 , A_W is the wetted area and ρ is the water density. Then, Eq. (1) and its solution can be written as follow:

$$(m + m_x) \ddot{x} - \rho A_W U_0 C_T \dot{x} + Kx = \underbrace{R_{C0} + R_{AW} - F_0}_{F'} + F_w \cos(\omega_e t) \quad (4)$$

$$\begin{aligned} x = & \\ \frac{F'}{K} + \frac{K - \omega_e^2(m + m_x)}{\left(K - \omega_e^2(m + m_x)\right)^2 + (\rho A_W U_0 C_T)^2} F_w \cos(\omega_e t) + & \frac{\rho A_W U_0 C_T}{\left(K - \omega_e^2(m + m_x)\right)^2 + (\rho A_W U_0 C_T)^2} F_w \sin(\omega_e t) + \\ C_1 e^{-\alpha t} \sin \sqrt{\omega_s^2 - \alpha^2} t + C_2 e^{-\alpha t} \cos \sqrt{\omega_s^2 - \alpha^2} t & \end{aligned} \quad (5)$$

Herein C_1 and C_2 are the constants for the general solution, $\alpha = \frac{\rho A_W U_0 C_T}{2(m + m_x)}$ and $\omega_s = K/(m + m_x)$.

To avoid interfere of spring with surge motion due to waves, a weak spring compared with $\omega_e^2(m + m_x)$ should be used, as shown in Eq. (5). The tests are conducted at Froude number 0.142 in calm water and in head waves with $A/L=0.009375$ and $\lambda/L=0.6\text{-}2.0$, i.e. $\min(\omega_e^2(m + m_x)) \cong 4700 \text{ N/m}$. The spring stiffness $K=98 \text{ N/m}$ is used to insure that $K \ll \omega_e^2(m + m_x)$. The external force F_0 for each case is adjusted close to $R_{C0} + R_{AW}$

i.e. $F' \cong 0$ to reduce the stretch of the spring.

Due to the nature of EFD test setup the hydrodynamic force excluding inertial force $X' = X - m\ddot{x}$ is recorded but not the hydrodynamic force X directly. Also, since the surge acceleration estimated from surge motion carries high level of noises, there is no way to estimate X from the recorded X' . The amplitude of measured force X' is much smaller than that of hydrodynamic force X and cannot be used to study the amplitude of resistance force in waves. Yet, the mean values for X and X' still remain the same because $\overline{m\ddot{x}} \cong 0$ such that the mean value of measured force X' can be still used to estimate the added resistance.

Some repeated tests are also performed to check the repeatability but the uncertainty of the data is not reported.

2.3 OTHER EFD RESOURCES

The fixed surge tests for long head waves were conducted for a 1/100 scaled model in the INSEAN 220×9×3.5 m³ towing tank. The towing tank is equipped with a single-flap wave generator that provides regular as well as irregular waves up to 450 mm height and wave length of 1 to 10m. The wave maker has 9 m wide controlled by a 100 harmonic components electronic programming device. The model was towed by the motor driven carriage while it was free to heave and pitch. A servo-mechanical (finger) probe Kenek-SH, positioned at the port side and at the same longitudinal position of the fore perpendicular, was used for the incoming wave measurements. Heave and pitch motions were measured using gyroscopic (MOTAN) platform and inclinometer. The surge force was measured by load cells lodged inside the joint, fixed to the model at the

center of gravity. The model was towed at Froude number 0.142 in head waves with $A/L=0.009375$ and $\lambda/L=1.1, 1.6$, and in calm water as shown in Table 2-2. The uncertainty of the data was not reported.

The fixed surge tests for short head waves were carried out for a 1/58 scaled model in the large towing tank at the Marine Technology Centre in Trondheim (Bingjie and Steen, 2010). The tank consists of two parts, one part is $175\times10.5\times5.6$ m³ and the other one is equally wide but with a length of 85m and a depth of 10m. For the current tests, the two parts were used as one tank with 260m length. The tank is equipped with double flap wave maker producing both regular and irregular waves with a period of 0.8-5 sec and generates waves with up to 0.9m wave height. The wave beach at the end of the tank reduces the reflection of waves. The model was connected to the carriage through a towing force dynamometer in the middle. The model was also connected to the carriage through trim posts at the fore and aft perpendiculars. The trim posts allowed freedom in heave and pitch, while keeping the model fixed in sway and yaw. The more details of experimental setup and procedure are discussed in Bingjie and Steen (2010). The experiment was carried out at $Fr=0.142$ in calm water and head waves and the calm water resistance and non-dimensional added resistance were reported. The wave cases were performed in different wave lengths and wave amplitudes to insure the wave steepness remains in linear region for very short waves. The wave length ranged from $\lambda/L = 0.18$ to 0.9173 . The wave amplitude was $0.002719L$ for $\lambda/L \leq 0.2289$, $0.00453L$ for $\lambda/L = 0.2289\sim0.4782$, and $0.01359L$ for $\lambda/L = 0.6365\sim0.9174$ as shown in Table 2-2. The uncertainty of the data was not provided but the precision error of the resistance force was reported about 0.7%D.

2.4 EVALUATION OF FACILITY BIASES

Table 2-3 Facility biases for calm water resistance, sinkage and trim (Fr=0.142).

	Surge motion	Model Length (m)	Re $\times 10^6$	Rudder	$10^3 \times C_T$		$I+k$		$10^3 \times (C_T - (I+k)C_F)$	
					D	Biases*	D	Biases*	D	Biases*
OU	Free	3.2	2.546	No	5.093	10.374	1.180	1.027	0.534	11.688
INSEAN ¹	Fixed	3.2	2.546	No	5.141	11.415	1.160	0.685	0.659	9.034
NTNU	Fixed	5.517	5.763	No	4.568	1.014	1.170+	0.171	0.696	15.162
MOERI	Fixed	5.517	4.6	W/	4.110	10.929	1.160	0.685	0.108	82.068
INSEAN ²	Fixed	7	8.240	No	4.160	9.845	1.170+	0.171	0.529	12.507
Average					4.614	8.714	1.168	0.548	0.605 ^{##}	12.098 ^{##}
Min.-Max. Facility Biases [‡]						11.172		0.856		13.834 ^{##}
	Surge motion	Model Length (m)	Re $\times 10^6$	Rudder	$10^2 \times x/L$ (-)		$10^2 \times \sigma/L$ (-)		τ (deg)	
					D	Biases*	D	Biases*	D	Biases*
OU	Free	3.2	2.546	No	-0.388	-	-0.099	5.930	-0.129	0.310
INSEAN ¹	Fixed	3.2	2.546	No	-		-0.081	13.660	-0.142	10.420
NTNU	Fixed	5.517	5.763	No	-		-0.116	24.170	-0.130	1.090
MOERI	Fixed	5.517	4.6	W/	-		-0.079	15.500	-0.132	2.640
INSEAN ²	Fixed	7	8.240	No	-		-0.093	0.940	-0.110	14.460
Average					-0.388	-	-0.094	12.040	-0.129	5.784
Min.-Max. Facility Biases [‡]						-		19.836		12.442

* Biases=100*|D-Average|/Average

+form factor is average of k from other facilities

‡Min.-Max. Facility Biases=100*($\frac{Max-Min}{2}$)/Average.

Excluded MOERI

Reference: OU (G2010); INSEAN¹ (G2010); NTNU (Bingjie and Steen, 2010); MOERI (Kim et al., 2010); INSEAN² (Fabbri et al., 2011)

Table 2-3 summarizes all available EFD data at Fr=0.142 in fully-loaded condition for total resistance force (C_T), sinkage (σ) and trim (τ) for calm water condition including data from MOERI for a model with L=5.5172 m (Kim et al., 2010) and another data from INSEAN for a model with L=7.0 m (Fabbri et al., 2011). Besides the total resistance, the residuary resistance ($C_T - (I+k)C_F$) which is mainly the wave resistance is compared among the facilities. For this purpose, the frictional resistance component (C_F) is calculated based on ITTC 1957 friction line and the estimated form factor (k) by

Prohaska method (Larsson et al., 2010) is used. For NTNU and INSEAN with larger model size, the form factor is estimated from the average k . In Prohaska method, data sets of C_T/C_F versus Fr^4/C_F prepared from a series of low-speed resistance tests are fitted to the first order polynomial equation in form of a Fr^4/C_F+b , in which b is $1+k$.

The facility biases for each facility (U_{FB}) and the facility biases based on the dynamic range ($U_{FB_{DR}}$) for forces and motions are estimated from:

$$\begin{cases} D_{ave} = \frac{1}{M} \sum_{i=1}^M D_i \\ U_{FB} = 100 \times |D_i - D_{ave}| / D_{ave} \\ U_{FB_{DR}} = \frac{1}{2} [\text{Max}(|D_i|) - \text{Min}(|D_i|)] / D_{ave}, \quad i = 1 \dots M \end{cases} \quad (6)$$

where D_i is the data in i^{th} facility and M is the number of facilities

Since different model sizes are used in different facilities, the Reynolds number is different among all EFD data. Due to the reduction of boundary layer thickness for higher Re , the friction component of the total resistance decreases with the increase of Reynolds number according to ITTC 1957 friction line as shown in Table 2-3. This results in lower total resistance for the models with larger sizes suggesting $U_{FB_{DR}} = 11.2\%$ for C_T . Among all facilities, the maximum facility bias U_{FB} for C_T is for INSEAN data. The facility biases $U_{FB_{DR}}$ for the residual resistance data excluding MOERI is 14%. The facility biases for the residual resistance are fairly large as the residual resistance data at low Fr is very small and slight difference provides large biases. The maximum facility bias for the residual resistance is for MOERI data. In fact, the measured resistance by MOERI is surprisingly 10% less than that for NTNU model which has the same size but no rudder. Based on the calculation conducted by Toxopeus et al. (2011), 0.76% of C_T is produced by the rudder, suggesting that the total resistance for MOERI model without the rudder is about 4.079×10^{-3} . This results in 0.08×10^{-3} residual resistance, even increasing more the facility biases for MOERI. For the form factor,

the $U_{FB_{DR}}$ is 0.86%. The INSEAN and MOERI form factors are the same i.e. $k \sim 0.16$. However, OU provides a fairly larger form factor. For motions, the surge is only available from OU and the facility biases cannot be studied. The sinkage is about 10% of the ship length for OU model while it is smaller for INSEAN and MOERI models and larger for NTNU model. The trim is about -0.13 deg for the facilities except for INSEAN 3.2 m long model. The facility biases $U_{FB_{DR}}$ for sinkage and trim are about 20% and 12%, respectively. Overall, the average of facility biases of the resistance and motions is about 11.63%D with the largest facility biases for sinkage. Since uncertainty of the data (U_D) is not available, the overall uncertainty in the data i.e. RSS of facility biases and U_D cannot be estimated.

CHAPTER 3: CFD METHODS

3.1 CFDSHIP-IOWA

The code CFDShip-Iowa v4.5 (Carrica et al., 2010) is used for the CFD computations. The CFDShip-Iowa is an overset, block structured CFD solver designed for ship applications using either absolute or relative inertial non-orthogonal curvilinear coordinate system for arbitrary moving but non-deforming control volumes. Turbulence models include the blended $k\text{-}\varepsilon/k\text{-}\omega$ based isotropic and anisotropic RANS, and DES approaches with near-wall or wall functions. A single-phase level-set method is used for free-surface capturing. Captive, semi-captive, and full 6DOF capabilities for multi-objects with parent/child hierarchy are available. The actual propeller, or interactive or prescribed body force propeller model can be employed for propulsion. Numerical methods include advanced iterative solvers, higher order finite differences with conservative formulation, PISO or projection methods for pressure-velocity coupling. Dynamic SUGGAR is used to obtain the overset interpolation information. A MPI-based domain decomposition approach is applied, where each decomposed block is mapped to one processor to perform high performance parallel computation.

For the current simulations, absolute inertial earth-fixed coordinates are employed with the blended $k\text{-}\varepsilon/k\text{-}\omega$ turbulence model using no wall function. The location of the free-surface is given by the ‘zero’ value of the level-set function, positive in water and negative in air. The 3DOF rigid body equations of motion are solved including spring force and external force F_0 introduced in the previous chapter in surge equation:

$$(m_1 + m_2 + m_3)[\dot{u} + wq] = X - Kx - F_0$$

$$(m_1 + m_2)[\dot{w} - u\dot{q}] = Z \quad (7)$$

$$I_y\dot{q} = M$$

Herein u, w, q are surge, heave, pitch velocities and I_y is moment of inertia around y axis.

For fixed surge condition, the surge equation is not solved and inertial term in heave equation includes only the mass of the model.

The governing equations are discretized using finite difference schemes on body-fitted curvilinear grids. In the turbulence and momentum equations, the time derivatives are discretized using second order finite Euler backward difference, the convection terms are discretized with higher order upwind formula, and viscous terms are computed by second order difference scheme. Projection method, a two-stage fractional step scheme, is employed to couple pressure and velocity field effectively using the PETSc toolkit (Krylov subspace method; BCGSL, Stabilized version of BiConjuate Gradient Squared method). In order to solve the system of the discretized governing equations, between three and five inner iterations are ran in each time step and solutions are considered to be converged once the error for velocities, pressure, and level-set reach to less than 10^{-5} , 10^{-8} , and 10^{-5} respectively.

3.2 BOUNDARY CONDITIONS, GRIDS, AND COMPUTATIONAL DOMAIN

Several types of boundary condition are required in this CFD study as described in Table 3-1. The half of the ship and flow field is modeled due to the symmetric conditions of the test cases. Thus, the X-symmetric condition is employed on $y=0$. The same boundary condition is also used for $y=1$. The far field boundary conditions are imposed on the top and bottom of background. The no-slip condition is applied on the solid

Table 3-1 Boundary conditions.

Type	Location	u	v	w	p	k_t	ω_t	v_t	ζ
Wave	Inlet/outlet	Eq. (8)	0	Eq. (9)	Eq. (10)	0	0	0	Eq. (7)
X-symmetric	Two sides of background	0	$\nabla v=0$	$\nabla w=0$	$\nabla p=0$	$\nabla k_t=0$	$\nabla \omega_t=0$	$\nabla v_t=0$	0
Far field #1	Bottom of background	u_∞	$\nabla v=0$	$\nabla w=0$	0	$\nabla k_t=0$	$\nabla \omega_t=0$	$\nabla v_t=0$	0
Far field #2	Top of background	u_∞	v_∞	w_∞	$\nabla p=0$	$\nabla k_t=0$	$\nabla \omega_t=0$	$\nabla v_t=0$	0
No-slip	Hull, tail and shaft	0	0	0	$\nabla p=0$	0	$\frac{60}{Re\beta\Delta y^2}$	0	0

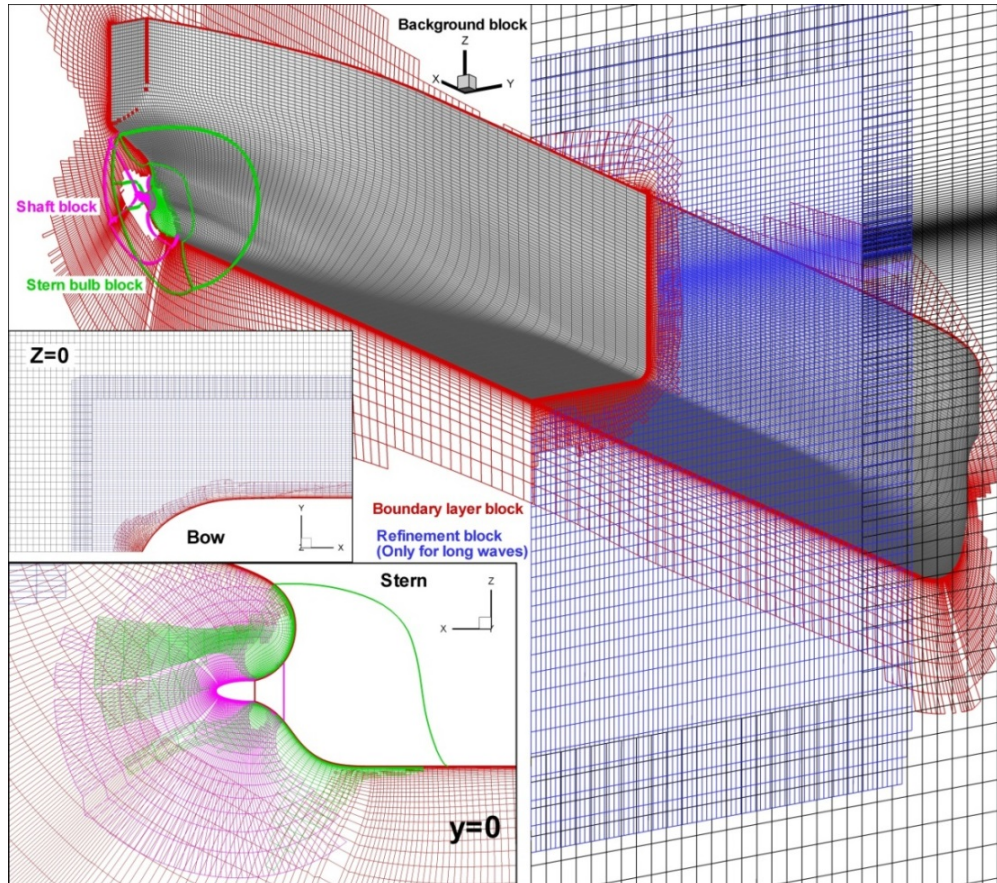


Fig. 3-1 Overset grid system, four blocks (three for short wave cases): boundary layer, shaft, stern bulb, background and refinement (there is no refinement block for short wave case).

surfaces. The wave boundary conditions calculated from the linear potential flow solution are applied for the inlet and outlet of the domain (Weymouth et al., 2005):

$$\zeta(x, t) = A \cos(kx - \omega_e t) \quad (8)$$

$$u(x, z, t) = \omega A e^{kz} \cos(kx - \omega_e t) \quad (9)$$

$$w(x, z, t) = \omega A e^{kz} \sin(kx - \omega_e t) \quad (10)$$

$$p(x, z, t) = \frac{\omega^2 A e^{kz}}{k} \cos(kx - \omega_e t) - \frac{\omega^2 A^2 e^{2kz}}{2} \quad (11)$$

Herein ζ is the unsteady free surface elevation, A is the wave amplitude, $k=2\pi/\lambda$ is the wave number, ω is the wave frequency and ω_e is the encounter frequency.

The computational grids are overset, with independent grids for the boundary layer, shaft, stern bulb, refinement, and background, and then assembled together to generate the total grid, as shown in Figure 3-1. The boundary layer, stern, and shaft grids are generated by a hyperbolic grid generator (Gridgen). A Cartesian grid is used to impose the far-field boundary conditions and to resolve the flow far from the hull, including a refinement block closer to the ship. The different grids generated for the current simulations are listed in Table 3-2. The grids G_3 and G_1 are generated from medium grid G_2 using coarsen/refinement ratio of $\sqrt{2}$. The grids G_3 , G_2 and G_1 are used for grid verification study firstly. The medium grid G_2 is used for all the simulations in calm water and head waves (mainly for long waves) including iteration and time step verifications. The total grid points are 1.66M, 4.7M and 13.1M for G_3 , G_2 and G_1 which are decomposed on 16, 40, and 104 CPUs for parallel processing, respectively. Since no wall function is applied in this study, the grid size on the solid surface is designed small enough to capture the boundary layer and turbulence. For instance, the smallest grid size in grids G_2 , GS_a , GS_b , GB_a and GB_b , which have the same grid design on boundary layer, stern bulb and shaft, is $10^{-6} L$ corresponding to $y^+=0.2$.

Table 3-2 Grid systems.

Grid name	Study	$i_{max} \times j_{max} \times k_{max}$ (grid points)					Total grid number	CPU numbers	Grid points per λ/L
		Boundary Layer	Stern bulb	Shaft	Refinement	Background			
G ₁	Grid verification $\lambda/L=1.1$	217×70×203 (3,083,570)	77×70×56 (301,840)	77×70×56 (301,840)	255×111×167 (4,726,935)	283×78×213 (4,701,762)	13,115,947	104	157
G ₂	Grid, iteration, and time step verification $\lambda/L=1.1$	154×50×144 (1,108,800)	55×50×40 (110,000)	55×50×40 (110,000)	181×79×119 (1,701,581)	201×56×151 (1,699,656)	4,730,037	40	111
	Calm water								-
	Added resistance (long waves)								60~200
G ₃	Grid verification $\lambda/L=1.1$	109×35×102 (389,130)	39×35×28 (38,220)	39×35×28 (38,220)	128×56×84 (602,112)	142×39×107 (592,566)	1,660,248	16	78
GS _a	Added resistance in shorter waves & fully-loaded cond. $\lambda/L=0.2833\sim0.4782$	154×50×144 (1,108,800)	55×50×40 (110,000)	55×50×40 (110,000)	-	2001×121×151 (36,560,271)	37,889,071	292	226~382
GS _b	Added resistance in shortest waves & fully-loaded cond. $\lambda/L=0.1810$	154×50×144 (1,108,800)	55×50×40 (110,000)	55×50×40 (110,000)	-	2001×121×181 (43,823,901)	45,152,701	348	144
GB _a	Added resistance with finer grid in ballast cond. $\lambda/L=0.6.0.9$	154×50×144 (1,108,800)	55×50×40 (110,000)	55×50×40 (110,000)	-	501×121×151 (9,153,771)	10,482,571	96	120,180
GB _b	Added resistance in shortest waves & ballast cond. $\lambda/L=0.3$	154×50×144 (1,108,800)	55×50×40 (110,000)	55×50×40 (110,000)	-	1001×121×151 (18,289,271)	19,618,071	192	120

To avoid strong numerical dissipation on wave propagation and capture the wave length and height, the grid size along x and z direction are designed carefully. The grids GS_a/GS_b and GB_a/GB_b are generated for the different domain size designed for the short wave cases in fully-loaded and ballast condition, respectively, as shown in Table 3-2. Both GS_a and GS_b grids have the same number of grid points along x and y directions but more grid points along z direction are designed for GS_b. The grid GS_a is used for the most of short wave cases in fully-loaded condition and GS_b is used for the shortest wave condition which owns very small wave amplitude. The total grid points are 37.9M and 45.1M for GS_a and GS_b, decomposed on 292 and 348 CPUs for parallel processing, respectively. The constant x spacing with grid size of 1.25×10^{-3} is applied to capture very short wave length. Near the free surface on z direction, the grid size is 2×10^{-4} for GS_a

and 10^{-4} for GS_a providing 22 and 27 grid points per wave amplitude. To consider the computational time consumption, for ballast condition in the short waves the grid GB_a and GB_b has the similar grid topology for the background with GS_a and GS_b but coarser with the constant x spacing with grid size of 5×10^{-3} and 2.5×10^{-3} . On z direction near the free surface, the grid size is 4×10^{-4} for both grids.

The computational domain extends from $-0.41 < x < 2.35$, $0 < y < 1$, $-0.97 < z < 0.23$ for grids G₁, G₂ and G₃ (long wave cases) and $-0.5 < x < 2$, $0 < y < 1$, $-0.8 < z < 0.2$ for GS_a, GS_b, GB_a and GB_b (short wave or fine grid cases) in dimensionless coordinates based on ship length, as shown in Figure 3-2. The ship axis is aligned with x with the bow (FP) at x=0 and the stern (AP) at x=1. The y axis is positive to starboard with z pointing upward. The undisturbed free surface at rest lies at z=0.

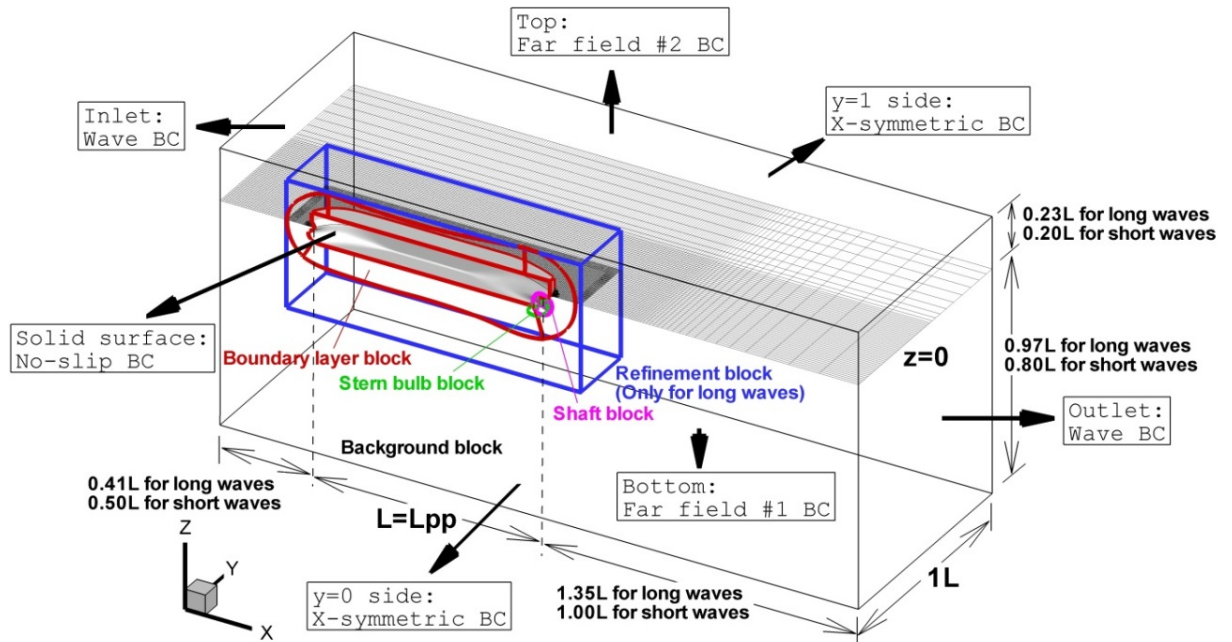


Fig. 3-2 Computational domain for both short and long waves.

3.3 SIMULATION CONDITIONS

The simulations are carried out in calm water and in head waves for both long and short wave length conditions, in fully-loaded and ballast condition as shown in Table 2-2. To obtain the added resistance in waves, the calm water resistance is gained firstly from the calm water simulations with ship free to sinkage and trim at $Fr=0.142$ and $Fr=0.25$. The simulations at $Fr=0.142$ are conducted for two model lengths corresponding to $Re=2.546\times10^6$ and $Re=5.763\times10^6$. The simulations in long waves are performed with $A/L=0.009375$ and $Fr=0.142$ for both free and fixed surge condition and $Fr=0.25$ for fixed surge condition. For $\lambda/L=1.1$, a simulation with $A/L=0.0046875$ is also conducted to study the wave amplitude effect. The free surge condition is achieved by towing the ship model using a spring mimicking EFD setup. The short wave simulations are conducted for fixed surge condition at $Fr=0.142$ with $\lambda/L=0.18$ and $A/L=0.002719$ and with $\lambda/L=0.20\sim0.48$ and $A/L=0.004531$ for fully-loaded condition, and with $\lambda/L=0.3$ and $A/L=0.005$ for ballast condition. The details of the test conditions for long and short waves are also shown in Table 2-2. To evaluate the wave forces components i.e. Froude-Krylov, diffraction and radiation, the fixed ship with no motion in head waves and imposed heave and pitch motions in calm water simulations are also conducted at both ship speeds. The natural frequency of vertical motions is also investigated in calm water at $Fr=0.0$ to find the resonance conditions for KVLCC2.

CHAPTER 4: UNCERTAINTY ANALYSIS

4.1 THE THEORY OF VERIFICATION AND VADIATION

Verification studies for the integral variables are performed to estimate the numerical uncertainties and confidence interval of a solution. The iterative uncertainties (U_i) are estimated from the dynamic range of the running mean and running RMS oscillations. The first step for estimation of the grid (U_G) and time step (U_T) uncertainties is the convergence study. For this purpose three solutions are obtained using systematically refined grid-spacing or time steps with refinement ratio:

$$r_{G/T} = \frac{\Delta x_2}{\Delta x_1} = \frac{\Delta x_3}{\Delta x_2} \quad (12)$$

where the subscripts 3,2 and 1 represent the coarse, medium and fine grids, respectively. Δx is either grid or time step spacing. The convergence of the solution is checked from the solution (S) on the three grids:

$$R_{G/T} = \frac{\epsilon_{12}}{\epsilon_{23}} = \frac{s_2 - s_1}{s_3 - s_2} = \begin{cases} 0 < R_{G/T} < 1 & : \text{Monotonic Convergence} \\ -1 < R_{G/T} < 0 & : \text{Oscillatory Convergence} \\ R_{G/T} > 1 & : \text{Monotonic Divergence} \\ R_{G/T} < -1 & : \text{Oscillatory Divergence} \end{cases} \quad (13)$$

The ratio of numerical ($P_{G/T}$) and theoretical order of accuracy (p_{th}) is used to quantify the distance metric from the asymptotic solution:

$$P_{G/T} = -\ln(R_{G/T})/\ln(r_{G/T}) \quad (14)$$

$$P = \frac{P_{G/T}}{p_{th}} \quad (15)$$

The solutions are expected to be in the asymptotic range when $P=1$. The uncertainties are estimated using factor of safety method discussed in Xing and Stern (2010) and

reported based on %S₁.

The iterative, grid and time step uncertainties provide an estimate of total numerical uncertainty U_{SN} for a simulation as below:

$$U_{SN} = \sqrt{U_I^2 + U_G^2 + U_T^2} \quad (16)$$

The validation uncertainty UV of the study accounts for both numerical and experimental (UD) uncertainties:

$$UV = \sqrt{U_{SN}^2 + UD^2} \quad (17)$$

The validation study provides a confidence interval for the numerical predictions by comparing the total uncertainties in the study UV and the comparison error (E). E is defined by the difference between data and simulation values:

$$E = (D - S)\%D \quad (18)$$

The numerical predictions can be validated at UV interval when $|E| \leq UV$.

Herein the validation (section 6.2) is performed at model scale based on the comparison error E for heave, pitch, surge and added resistance for mean value and 1st harmonic amplitude and phase. The mean, 1st harmonic amplitude and phase of parameter P are determined from time histories as follow:

$$P(t) = \frac{P_0}{2} + \sum_{n=1}^N P_n \cos(2\pi f_e t + P_{en}) \quad (19)$$

$$a_n = \frac{2}{T} \int_0^T P(t) \cos(2\pi f_e t) dt \quad (20)$$

$$b_n = \frac{2}{T} \int_0^T P(t) \sin(2\pi f_e t) dt \quad (21)$$

$$P_n = \sqrt{a_n^2 + b_n^2} \quad (22)$$

$$P_{en} = \tan^{-1} \left(-\frac{b_n}{a_n} \right) - \gamma_G \quad (23)$$

where P_0 is the mean value, P_n is the n-th harmonic amplitude and P_{en} is the corresponding phase, and γ_G is the initial wave phase at center of gravity at t=0.

4.2 RESULT OF VERIFICATION STUDY

Table 4-1 Verification study for $\lambda/L=1.1$ (fully-loaded condition).

		z_0 (cm)	z_1/A	θ_0 (deg.)	θ_1/Ak	C_{aw}	X_1 (N)	Ave.
Grid verification with $r_G=\sqrt{2}$; G_1, G_2, G_3 grid	R_G	-0.3369	0.3502	0.4855	0.5862	0.5007	0.4801	
	Convergence [‡]	OC	MC	MC	MC	MC	MC	
	P_G	-	3.0277	2.0847	1.5412	1.9959	2.1174	
	$\varepsilon_{I2_G}\%S_I$	0.65	1.65	2.73	3.48	3.36	0.88	
	$U_G\%S_I$	0.97	2.41	2.88	4.93	3.37	0.95	2.59
Uncertainty of time step with $r_T=\sqrt{2}$; $\Delta t=0.015$, $\Delta t_2=0.021$, $\Delta t_3=0.03$	R_T	-0.2662	-0.0607	-1.3778	0.1371	-0.0730	0.5335	
	Convergence [‡]	OC	OC	OC	MC	OC	MC	
	P_T	-	-	-	5.7342	-	1.8129	
	$\varepsilon_{I2_T}\%S_I$	0.35	0.22	4.88	-0.40	0.40	1.51	
	$U_T\%S_I$	0.67	1.81	1.86	0.74	2.76	1.75	1.60
Uncertainty of iteration (S_I)	$U_I\%S_I$	2.01	0.10	4.14	0.12	0.71	0.46	1.26
	U_I/ε_{I2_G}	3.09	0.06	1.52	0.03	0.21	0.52	
	U_I/ε_{I2_T}	5.74	0.45	0.85	0.30	1.78	0.30	
	U_I/U_G	2.07	0.04	1.44	0.02	0.21	0.48	
	U_I/U_T	3.00	0.06	2.23	0.16	0.26	0.26	
Simulation uncertainty	$U_{SN}\%S_I$	2.33	3.02	5.38	4.99	4.41	2.04	3.69

[‡] Convergence: MC=Monotonic Convergence; OC=Oscillatory Convergence; MD=Monotonic Divergence; OD=Oscillatory Divergence

The iterative, grid and time step uncertainties are investigated for fully-loaded condition and fixed surge in head waves at $Fr=0.142$ in the wave length of $\lambda/L = 1.1$ for which the added resistance is expected to be the maximum. The iterative uncertainty is evaluated using grid G_2 with $\Delta t=0.015$ sec. The grid verification study is conducted using grid triplets G_3 , G_2 and G_1 with $r_G=\sqrt{2}$. The time step verification study is performed for G_2 with $r_T=\sqrt{2}$, $\Delta t=0.015$, 0.021 and 0.03 sec. Verification variables are the mean value and amplitude of heave ($z_0, z_1/A$), the mean value and amplitude of pitch ($\theta_0, \theta_1/Ak$) and the added resistance and amplitude of axial force (C_{aw}, X_1).

The iterative uncertainty listed in Table 4-1 shows relatively large values for the mean value of the motions, about 2% S_I for z_0 and 4% S_I for θ_0 . Also, U_I for the mean value of the motions is large compared to U_G , U_T , ε_{I2_G} and ε_{I2_T} while the U_I for the rest of the variables are acceptably small. The average uncertainty is about $U_I = 1.26\%S_I$, showing the results are fairly insensitive to the iterative errors.

The grid study shows oscillatory convergence for z_0 and $z_{\varepsilon 1}$ with $R_G = -0.34$ and -0.58 and monotonic convergence for z_1/A with $R_G = 0.35$. The grid verification study for θ_0 and θ_1/Ak shows monotonic convergence with R_G of 0.48 and 0.59, respectively. The added resistance and amplitude of axial force are also converged monotonically with R_G of about 0.5. The order of accuracy P_G is about 2 for most of the variables. The ε_{I2_G} and U_G ranges from $\varepsilon_{I2_G}=0.65$ to $3.48\%S_I$ and $U_G = 0.94$ to $4.76\%S_I$ in which the minimum is for z_1/A and X_1 and the maximum is for θ_1/Ak . The average of the grid uncertainty is about $U_G = 2.6\% S_I$, suggesting that the effects of the grid changes are negligible on the results for the present range of grid size.

The time step verification study shows monotonic convergence for θ_1/Ak and X_1 with $R_T = 0.14$ and 0.53 ; oscillatory convergence for z_0 , z_1/A , θ_0 and C_{aw} with $R_T = -0.06 \sim -1.4$; and oscillatory divergence for $z_{\varepsilon 1}$ and $\theta_{\varepsilon 1}$. The order of accuracy for monotonically converged variables θ_1/Ak and X_1 is $P_T = 5.7$ and 1.8 . The ε_{I2_T} is less than $0.4\%S_I$ for most of the variables while it is $4.88\%S_I$ and $1.51\%S_I$ for θ_0 and X_1 . The average of time step uncertainty is $U_T = 1.60\% S_I$ with maximum uncertainty of $2.76\% S_I$ for C_{aw} .

The total numerical uncertainty is computed using Eq. (16) showing average uncertainty of $U_{SN}=3.69\%S_I$ for the verification variables for fixed surge in head waves at $\lambda/L = 1.1$. The numerical uncertainty is about 40% smaller than the average

numerical uncertainty $U_{SN} = 5.77\%S_I$ for the seakeeping cases performed using CFDShip-Iowa for other geometries reported in Weymouth et al. (2005), Carrica et al. (2007), Simonsen et al. (2008), Castiglione et al. (2009) and Mousaviraad et al. (2010).

4.3 VERIFICATION FOR PHASES

Sadat-Hosseini et al. (2013) revealed the difficulty to achieve converged verification for the phases of heave and pitch motion (1st harmonic). Since URANS solves the flow field in time domain, the time needs to be discretized numerically. The time step ($\Delta t=0.015$) for $\lambda/L=0.6\sim2.0$ is determined by the shortest wave length, i.e. more than 50 time steps for one period. And based on the boundary conditions, Eq. (8)~(11), the incident waves propagate on discretized space and time. Also the phase lag could not be obtained before the simulations. Thus, the encounter period extracted from numerical time history would keep varying very slightly from the exact encounter period. It might cause the problem for the Fourier analysis to calculate the phases. On the other hand, the computation time for the case with fine grid or small time step would be much longer than the case with coarse grid or large time step. It is not easy to choose the longer and the same time length for all cases for the Fourier analysis.

However, Figure 4-1 shows that the phase differences among different grid sizes (G_1 , G_2 and G_3) and different time step ($\Delta t=0.015$, 0.021 and 0.03) are very small. The curves are almost oscillating in the same period although the phases do not satisfy the verification requirement in the previous section. By picking up one and the same period to perform Fourier analysis (Table 4-1), the phase differences among the verification cases are around 1 deg, which is smaller than the time step in deg and minimum grid

size in x direction in deg. Also, from coarse to fine grid and large to small time step, the converging peak of the motion amplitude is observed (the value in red is closer to the blue one). It confirms the verification result concluded in the previous section. Therefore, the G_2 grid system with time step $\Delta t=0.015$ would be used in the following studies for $\lambda/L=0.6\sim 2.0$.

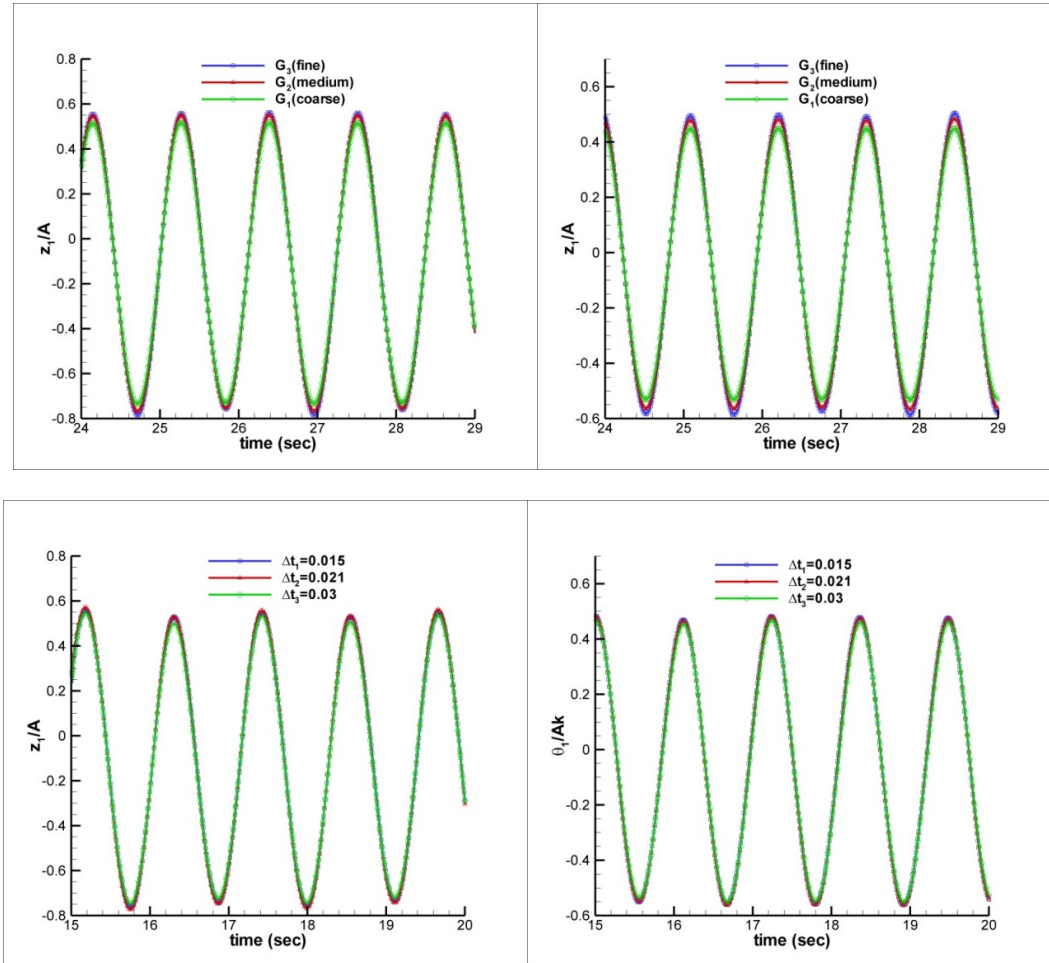


Fig. 4-1 Time history of verification cases for ship motions.

Table 4-2 Phase values for verification studies.

		z_{el} (deg.)	θ_{el} (deg.)	Δt	Δt (deg.)	Grid points per λ/L : n	Δx (deg.)
Grid size study	G ₁	45.92	-15.46	0.015	4.82	157	2.29
	G ₂	46.28	-14.94	0.015	4.82	111	3.24
	G ₃	47.40	-14.14	0.015	4.82	78	4.62
Time step study	Δt_1	46.34	-15.18	0.015	4.82	111	3.24
	Δt_2	44.71	-14.54	0.021	6.75	111	3.24
	Δt_3	44.38	-13.38	0.03	9.64	111	3.24

$$\Delta x \text{ (deg.)} = 1/n * 360 \text{ (deg.)}$$

$$\Delta t \text{ (deg.)} = \Delta t \text{ (sec)} * f_e \text{ (Hz)} * 360 \text{ (deg.)}$$

CHAPTER 5: MAXIMUM SHIP RESPONSE

5.1 1 DOF SHIP MOTION

The motions of 1 DOF ship in ship fixed coordinate system can be found from the following equation.

$$\Delta \ddot{x} = X \quad (24)$$

where Δ is the ship mass or moment of inertia, x is the displacement which could be surge, heave or pitch and X is the forces or moments.

This equation is simplified version of the equations solved for CFD simulation (see Eq. (7)) since it is 1DOF and not coupled with other modes of motion. For potential flow, the forces on the right hand side are divided into the gravitational forces (X_G) and the fluid forces including hydrostatic (X_{HS}) and hydrodynamic forces (X_{HD}). The hydrodynamic forces on the free ship can be divided between the steady forces in calm water (X_S) and the unsteady forces which are the total wave forces (X_{TF}) acting on free ship in waves. The total wave forces including the wave forces acting on the restrained ship (X_{EF}), i.e., the forces that excite the motions, and the radiation forces due to the motions of the ship in calm water (X_{RF}). The excitation forces and moments are divided into the Froude-Krylov (X_{FK}) and diffraction (X_{DF}). Froude-Krylov is the wave force induced by incident wave on the fixed ship while the waves are undisturbed. The diffraction is the wave force induced by the diffracted waves in the presence of the ship:

$$\Delta \ddot{x} = X_G + X_{HS} + X_{HD} = \underbrace{X_G + X_{HS}}_{X_{HS}^*} + X_S + \underbrace{X_{FK} + X_{DF} + X_{RF}}_{X_{TF}} \quad (25)$$

The combined gravitational and hydrostatic forces are the net hydrostatic restoring

forces (X_{HS}^*) and are assumed to be proportional to the ship displacements (Cx) and radiation forces are assumed to be in form of ($-B\ddot{x} - \Delta_A\ddot{x}$). These terms are brought to the left hand side, providing the equations of motion for potential flow approaches.

$$(\Delta + \Delta_A)\ddot{x} + B\dot{x} + Cx = X_S + X_{FK} + X_{DF} \quad (26)$$

where Δ_A is the added mass or added inertia, B is damping and C is restoring terms.

Eq. (26) shows that the wave-induced motion of a ship can be described in analogy to a forced mass-spring system with damping. The steady forces and the mean value of wave forces are responsible for the steady motions while the oscillatory components of wave forces are responsible for oscillatory ship motions. To investigate the maximum amplitude of ship motions, non-dimensional Eq. (26) can be rewritten as follow assuming that both forces are in form of sinusoidal functions.

$$\ddot{x} + \alpha\dot{x} + \omega_n^2x = A_{FK} \left(\frac{\lambda}{L} \right) \sin(\omega_e t + \varepsilon_{FK} \left(\frac{\lambda}{L} \right)) + A_{DF} \left(\frac{\lambda}{L} \right) \sin(\omega_e t + \varepsilon_{DF} \left(\frac{\lambda}{L} \right)) \quad (27)$$

Herein, α is damping, ω_n is natural frequency, A_{FK} and ε_{FK} are Froude-Krylov amplitude and phase, and A_{DF} and ε_{DF} are diffraction amplitudes and phases.

5.2 MAXIMUM SHIP RESPONSE CONDITION

Eq. (27) shows that the ship motions are dependent on α , ω_n , ω_e and Froude-Krylov and diffraction amplitudes and phases. The ship motions would be maximum when the amplitude of combined Froude Krylov and diffraction (wave excitation force amplitude) is large and the ship is at resonance condition. As shown earlier (see Fig. 1-1), the surge and pitch excitation forces are largest around $\lambda=1.33L$ and the heave excitation force increases by increasing wave length. The heave and pitch would be at resonance condition when $f_e=f_n$. The heave and pitch natural frequencies neglecting speed effects

can be assessed using the empirical formula. The natural frequency of heave is given by:

$$f_z = \sqrt{\frac{g C_{Wp}}{8\pi^2 C_B T}} \quad (28)$$

where C_{Wp} is water plane area coefficient, C_B is block coefficient, and T is draft.

The natural frequency of pitch is given by:

$$f_\theta = \sqrt{\frac{C_{IT} g B^3}{96\pi^2 \hat{I}_y L_{PP}^4}} \quad (29)$$

where, $C_{IT}=12I_T/(B^3L_{PP})$ is the coefficient of inertia of the water plane area about the y axis, and $\hat{I}_y=I_y/(\rho L_{PP}^5)$ is a non-dimensional mass moment of inertia about the y axis.

Note that the empirical formula for both heave and pitch frequencies are derived under the assumption that the added mass/inertia of heave/pitch is the same as the ship mass/moment of inertia.

Irvine et al. (2008) investigated the critical ship speed for maximum ship motions condition by matching the resonance condition ($f_e=f_n$) and maximum excitation forces/moment wave length condition but did not distinguish the conditions for maximum heave and pitch excitation forces/moment and used $\lambda=1.33L$ for both heave and pitch as shown in Eq. (32).

$$Fr_{coincidence} = \frac{\lambda}{L} \left(\sqrt{\frac{L}{g}} f_n - \sqrt{\frac{3}{8\pi}} \right) \quad (30)$$

The condition for maximum ship motions was postulated after comparing the predictions of maximum condition with the experimental data of a surface combatant. Simonsen et al. (2008) and Castiglione et al. (2009) attempted to confirm the proposed condition for maximum ship motions by Irvine et al. (2008) but the maximum heave motion was at a wave length fairly far from $\lambda/L=1.33$. Herein, the maximum ship responses condition is studied and fully explained which is also supported by the data from Simonsen et al. (2008) and Castiglione et al. (2009).

5.3 DIFFRACTION AND RADIATION PROBLEM IN PF AND CFD

The components of the forces in the equations of ship motion for potential flow including Froude-Krylov, diffraction and radiation can be evaluated using CFD results.

In PF, the X_{FK} component is computed by integrating the wave-induced pressure on hull which is known from the velocity potential of the incident wave. The X_{DF} is computed from the velocity potential for the diffracted waves after solving the diffraction problem. The wave excitation force is provided by adding Froude Krylov and diffraction components. The radiation component is considered as the added mass and damping terms and thus not computed directly.

To evaluate the components, different CFD simulations are required. Since the incident waves and the wave-induced pressure field is known, X_{FK} is computed similar to PF. To estimate the wave excitation forces X_{EF} , the ship with forward speed and restrained from moving in the presence of the wave is simulated and the forces X on the ship is computed (See right hand side of Eq. (24)). The net hydrostatic forces and steady resistance force are subtracted from the above total forces to have X_{EF} using Eq. (31).

$$X = X_{HS}^* + X_S + X_{EF} \quad (31)$$

The total CFD wave excitation X_{EF} and Froude Krylov X_{FK} can provide estimates for CFD diffraction, assuming that there is no nonlinearity and/or interaction between Froude-Krylov and diffraction:

$$X_{DF} = X_{EF} - X_{FK} \quad (32)$$

The CFD radiation forces are calculated from the forces on a ship forced to oscillate in calm water with forward speed. The forces on the ship X are computed (See right hand

side of Eq. (24)) and then the net hydrostatic forces and steady resistance force need to be subtracted from the computed forces to estimate the radiation component based on Eq. (33). However, herein only the steady resistance force is subtracted from the total radiation force and the radiation component included hydrostatic term for both CFD and potential flow. The imposed motions for the radiation problem is the same as the predicted motions in head wave simulations. After having all the wave component forces, the summation of the components can be evaluated with the total wave forces X_{TF} calculated by integrating the pressure on the free ship in waves.

$$X = X_{HS}^* + X_S + X_{RF} \quad (33)$$

5.4 CFD NATURAL FREQUENCY SIMUATIONS

The empirical natural frequencies for heave and pitch at $Fr=0.0$ in fully-loaded condition based on Eq. (28) and Eq. (29) are $f_z \approx 0.81$ HZ and $f_\theta \approx 0.87$ HZ. Since Fr effects on natural frequencies are small according to Lewis (1989), the empirical heave and pitch natural frequencies are expected to be very close to natural frequencies at $Fr=0.142$ and $Fr=0.25$.

To evaluate the frequencies given by empirical formula, the natural heave and pitch frequencies are calculated by conducting CFD simulations at $Fr=0.0$ for 1DOF ship free only to heave/pitch and 2DOF free to heave and pitch. In all the simulations, the initial heave/pitch is imposed and then the ship is released to record the frequency of the heave/pitch oscillations. The initial heave is $-0.001L$ and the initial pitch is 5.73×10^{-3} deg as shown in Table 5-1. The 2DOF simulation is conducted twice with imposing either heave or pitch in each simulation. For heave motion, 1DOF and 2DOF CFD

simulations and Eq. (28) provide frequencies with less than 4% difference suggesting that the uncoupled, coupled and empirical heave frequencies are fairly the same. For pitch motion, 1DOF CFD simulation and empirical value show 7.6% difference for f_θ and 2DOF CFD simulation provides about 10% smaller f_θ compared to that from 1DOF CFD simulation, introducing that the empirical formula does not estimate the pitch frequency accurately and also there is significant change in pitch frequency in existence of heave motion.

Since the heave and pitch motions are free for all the simulations in this paper, the coupled heave and pitch natural frequencies are considered in this work. For fully-loaded condition, $f_z = 0.809$ HZ and $f_\theta = 0.713$ HZ. For ballast condition, $f_z = 0.691$ HZ and $f_\theta = 0.717$ HZ. Between two different loading conditions, the heave natural frequencies are more different than the pitch one. From Eq. (30) and (31), more differences for C_{WP} , C_B and T could be observed between two different loading conditions to cause more different heave natural frequencies.

Table 5-1 Natural frequency in calm water at $Fr=0.0$.

	Theory	1DOF	1DOF	2DOF	2DOF
Free Motion	-	Heave	Pitch	Heave	Heave
Fully-loaded cond.	-	z/L	$\theta(\text{deg.})$	z/L	$\theta(\text{deg.})$
Initial condition	-	$=-0.001$	$=5.73 \times 10^{-3}$	$=-0.001$	$=5.73 \times 10^{-3}$
f_{n_heave} (Hz)	0.8100	0.8308	-	0.8093*	0.8031
%Theory	-	-2.57	-	0.09	0.85
f_{n_pitch} (Hz)	0.8710	-	0.8043	0.7132*	0.7263
%Theory	-	-	7.66	18.12	16.61
Ballast Cond.	Free Motion	-	-	Heave	-
Initial condition	-	-	-	z/L	-
f_{n_heave} (Hz)	-	-	-	0.6908*	-
f_{n_pitch} (Hz)	-	-	-	0.7171*	-

* f_{n_heave} and f_{n_pitch} are used in the following RAO studies.

CHAPTER 6: GLOBAL VARIABLE RESULTS

6.1 CALM WATER RESULTS

Table 6-1 Comparison of CFD and EFD resistance force and motions for resistance test in calm water.

	CFD	E%DOU	E%DINSEAN	CFD	E%DNTNU	CFD
	Fr=0.142			Fr=0.142		Fr=0.25
	Re=2.546×10 ⁶			Re=5.763×10 ⁶		Re=4.482×10 ⁶
Fully loaded	C_T	5.490×10^{-3}	-7.795	-6.789	4.836×10^{-3}	-5.868
	C_F	3.844×10^{-3}	0.518*	0.518*	3.302×10^{-3}	0.218*
cond.	x/L (-)	-0.406×10^{-2}	-4.558	-	-	-
	τ/L (-)	-0.101×10^{-2}	-2.155	-25.34	-0.101×10^{-2}	12.964
	σ (deg)	-0.124	4.031	12.817	-0.123	5.077
	Ave.		3.81	11.36		6.032
Ballast	CFD	E%DOU				
	Fr=0.142					
cond.		Re=2.546×10 ⁶				
	C_T	9.981×10^{-3}	-2.358			

* EFD friction component is estimated from ITTC57 formula

Table 6-1 shows EFD and CFD comparison for calm water case. CFD simulations are conducted at $Fr=0.142$ in fully-loaded condition with two different Re number ($Re=2.546 \times 10^6$ and 5.763×10^6) and at $Fr=0.25$ ($Re=4.482 \times 10^6$). The results for $Fr=0.142$ and $Re=2.546 \times 10^6$ are compared with the resistance test data provided from the facilities using same model length or Reynolds Number i.e. the OU and INSEAN data. This is to avoid the scaling effect on the results which is not negligible as discussed in Section 2.4. The results for $Fr=0.142$ and $Re=5.763 \times 10^6$ are compared against the data provided by NNTNU.

The CFD total resistance prediction at $Fr=0.142$ and $Re=2.546 \times 10^6$ is about $C_T=0.0055$ showing about 7%D error compared with both OU and INSEAN data. Note

that even though the CFD is conducted with free surge condition similar to OU data, the results can be compared against INSEAN data as the free and fixed condition should not change the steady state values but the transient values. The friction component of CFD resistance is compared against ITTC57 formula and shows very good agreement with $E=0.518\%D$. This suggests that the under prediction of the total resistance is originated from the wave making component of the resistance. The surge motion data is only available from OU. The external force F_0 applied in the experiment was provided 6 N in model scale. The same force is applied in CFD simulation using Eq. (7). The CFD prediction of surge motion provides very good agreement with EFD data by $E=4.6\%D$. CFD predicts sinkage and trim by $E=-2.15\%D$ and $4.03\%D$, respectively, compared with OU data. The prediction errors for both sinkage and trim are larger by comparing with INSEAN data. Note that the trim motion provided by INSEAN is far away from the values provided by other facilities as discussed in Section 3.3. The average of CFD predictions at $Re=2.546\times10^6$ compared with OU and INSEAN data is about $3.8\%D$ and $11.36\%D$, respectively.

The CFD results at $Fr=0.142$ and $Re=5.763\times10^6$ show lower resistance due to the reduction of frictional resistance at higher Re number while the sinkge and trim are the same as before. The comparison of CFD results with NTNU shows the average of prediction error of $6\%D$ with $E=5.8\%$ and $0.2\%D$ for the total resistance and frictional resistance and 12.96 and $5.1\%D$ for sinkage and trim. The average of the errors for both Re numbers for resistance, sinkage and trim are $6.82\%D$, $13.48\%D$ and $7.3\%D$, about 60% of the facility biases discussed in Section 2.4. Overall, the total average of the errors for both Re numbers is $7.07\%D$. The KVLCC2 resistance and motions in calm water was also studied as part of the Gothenburg 2010 workshop test cases by Deng et

al. (2010). The current CFD simulation shows better prediction of the resistance and motions of KVLCC2 in calm water compared with $E=10\%D$ reported in Deng et al. (2010). Also, the prediction error is very close to the average prediction error $E=7.18\%D$ for the resistance test simulations performed using CFDShip-Iowa for other geometries reported in Carrica et al. (2007), Xing et al. (2008, 2009), Sadat-Hosseini et al. (2010b, 2011), Castiglione et al. (2009), Kandasamy et al. (2010) and Takai et al. (2011).

Comparing the CFD results at $Fr=0.142$ and $Fr=0.25$ shows that the total resistance is nearly doubled from $Fr=0.142$ to $Fr=0.25$ while the friction component is reduced due to higher Re number. Thus, the residual resistance or the wave making resistance is significantly raised at high speed as expected. The sinkage and trim are also changed dramatically by changing the ship speed. The non-dimensional sinkage is -0.3472×10^{-2} at $Fr=0.25$ compared to -0.101×10^{-2} at $Fr=0.142$. The sinkage is increased at $Fr=0.25$ due to the significant pressure drop under the ship resulting in pushing the ship down into the water. The trim is also four time larger at $Fr=0.25$.

For the ballast condition, only the cases with $Fr=0.142$ and $Re=2.546 \times 10^6$ are conducted for CFD and EFD. Both results agree well. The CFD predicts the total resistance $C_T=0.009981$ with around $-2\%D$ error.

6.2 FULLY-LOADED CONDITION

6.2.1 Time history study

Figure 6-1 shows the EFD and CFD comparison for motions and axial force for $\lambda/L = 0.6$ and $Fr=0.142$ in time domain. EFD time histories are only available for free

Table 6-2 Running mean and running RMS of EFD and CFD time histories.

	U_f %Ave	x (cm)		z (cm)		θ (deg.)		X (N)		Ave.	
		Running mean	Running RMS	Running mean	Running RMS	Running mean	Running RMS	Running mean	Running RMS	Running mean	Running RMS
$\lambda/L=0.6$	EFD Free	4.2	2.6	1.16	0.33	2.02	0.43	-	-	2.46	1.12
	CFD Fixed	-	-	0.32	0.19	1.47	0.81	2.74	0.20	1.51	0.40
	CFD Free	2.0	0.8	0.12	0.11	1.60	0.16	1.05	0.11	1.19	0.30
$\lambda/L=1.1$	EFD Fixed	-	-	3.92	0.18	10.0	0.22	2.12	0.18	5.35	0.19
	EFD Free	2.2	2.8	2.64	0.55	5.55	0.23	-	-	3.46	1.19
	CFD Fixed	-	-	3.25	0.17	7.10	0.18	1.83	0.36	4.06	0.24
	CFD Free	2.1	1.4	2.01	0.10	4.14	0.12	0.71	0.46	2.24	0.52
$\lambda/L=1.6$	EFD Fixed	-	-	6.91	0.27	14.2	0.31	9.10	0.47	10.07	0.35
	EFD Free	3.1	1.8	3.79	0.39	4.48	0.39	-	-	3.79	0.86
	CFD Fixed	-	-	5.63	0.40	5.85	0.39	5.25	0.57	5.58	0.45
	CFD Free	2.5	1.6	3.46	0.21	3.59	0.17	3.3	0.23	3.21	0.55

surge condition. The EFD running mean and running RMS show 2.46%Ave and 1.12%Ave convergence error for mean values and amplitudes, respectively, as shown in Table 6-2. The EFD surge motion has the maximum convergence error, suggesting x is not converged very well. The x oscillates at both f_e and spring natural frequency $f_s = \frac{1}{2\pi}\sqrt{K/m}=0.09\text{HZ}$ with amplitudes of 0.055A and 0.18A, respectively. The mean value of x cannot be discussed as it is shifted by an arbitrary F_0 used in the experiment. EFD z and θ show sinusoidal response with frequency of f_e with amplitudes of 0.06A and 0.017Ak, respectively, with about 100 deg phase lag between them. The mean values of z (-0.3147 cm) and θ (-0.124 deg) are nearly close to the values for calm water. For axial force, there is no EFD data for X time history as $X' = X - m\ddot{x}$ was recorded which could only be used to estimate the mean value of X since $\bar{X}' = \bar{X}$. The mean value of EFD axial force is 6.85 N which is 2.47 N larger than for calm water representing the added

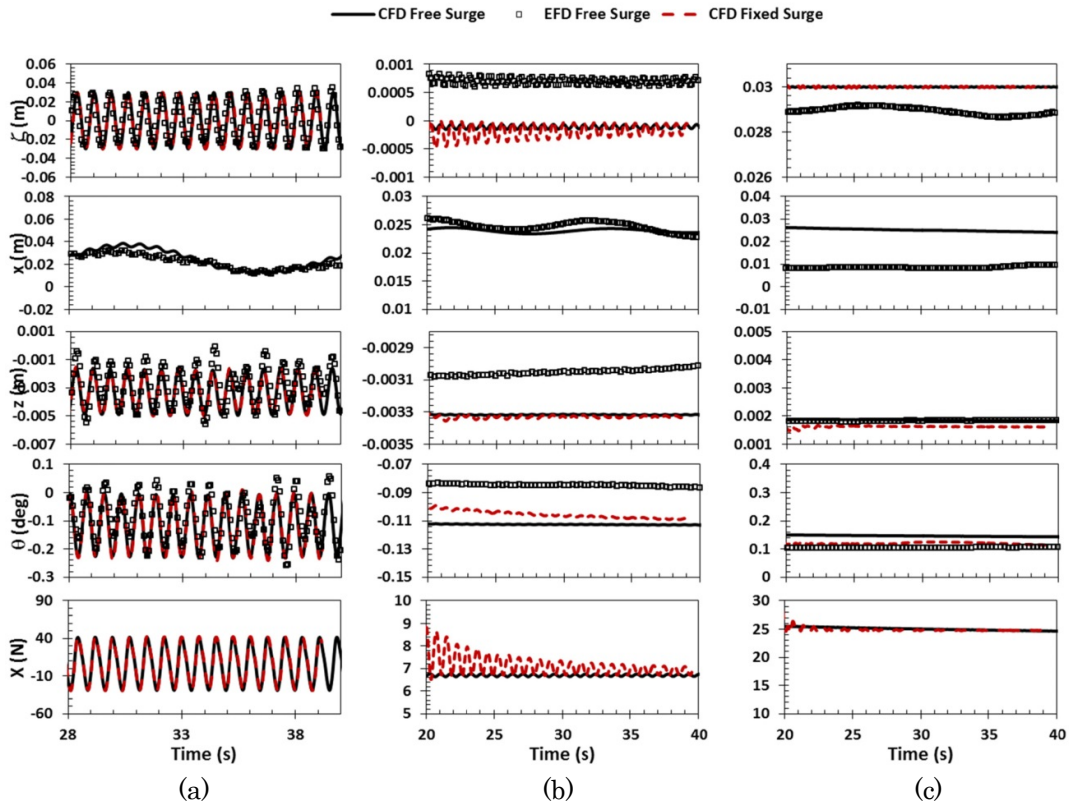


Fig. 6-1 The results for $\lambda/L=0.6$: (a) Wave signal and motions; (b) Running mean time histories; (c) Running root mean square time histories.

resistance. The CFD simulations for free and fixed surge are converged with the smaller convergence errors compared to EFD, as shown in Table 6-2. For free surge condition, x oscillates at f_e and f_s with the amplitude of $0.056A$ at f_e , very similar to the EFD values. The CFD surge motion is simply shifted to match the mean value to that of EFD in the plots as CFD was blind in that EFD F_0 was unknown. CFD z and θ amplitudes are under predicted and over predicted by 10%D, respectively. The mean values of z and θ are predicted by nearly 6%D. For X , the mean value is under predicted by 7%D suggesting the added resistance is under predicted as well. The fairly large difference between CFD and EFD could be partially due to convergence and repeatability uncertainty on EFD data. The comparison with fixed surge results indicates no

significant differences for z and θ responses and X force. This emphasizes that there is no strong coupling between z , θ and x .

Figure 6-2 shows the EFD and CFD comparison for $\lambda/L = 1.1$ and $Fr=0.142$. The EFD convergence errors are fairly large for z and θ mean values for both free and fixed surge conditions, as shown in Table 6-2. The EFD surge motion x oscillates at f_e and f_s with amplitudes of 0.073A and 0.319A, respectively. EFD z and θ for free surge condition show the ship motions just follow the sinusoidal incident wave pattern with a period corresponding to f_e and amplitudes of $z/\theta=0.66A/0.50Ak$, very significant compared to those for $\pi/L=0.6$ as f_e is closer to maximum wave excitation force and resonance condition. Yet, the higher harmonics and nonlinearities are not observed for these motions. The mean values are -0.32 cm and -0.134 deg, suggesting that the ship oscillates around bow down position while it is sank. The EFD mean axial force is 10.39 N, 58% larger than the resistance in calm water. For fixed surge condition, EFD shows sinusoidal pattern for z and θ with amplitude of 0.66A and 0.56Ak, same heave but larger pitch amplitude compared to free surge condition. The mean values are -0.357 cm and -0.183 deg, quite different with those values for free surge. The CFD results are converged with relatively large convergence errors for pitch mean value, similar to EFD, as shown in Table 6-2. For free surge, the amplitude at f_e / f_s is over/under predicted by 8%D. The mean value of CFD x is shifted to match to that of EFD, as discussed earlier. CFD shows remarkable agreement with EFD z and θ with less than 3%D prediction error for both amplitudes and mean values. Also, the mean value of X is over predicted by only 3%D suggesting good prediction of added resistance. The CFD results comparison for fixed and free surge condition shows less than 3% changes in z and θ mean values and amplitudes and 5% changes in mean value of X .

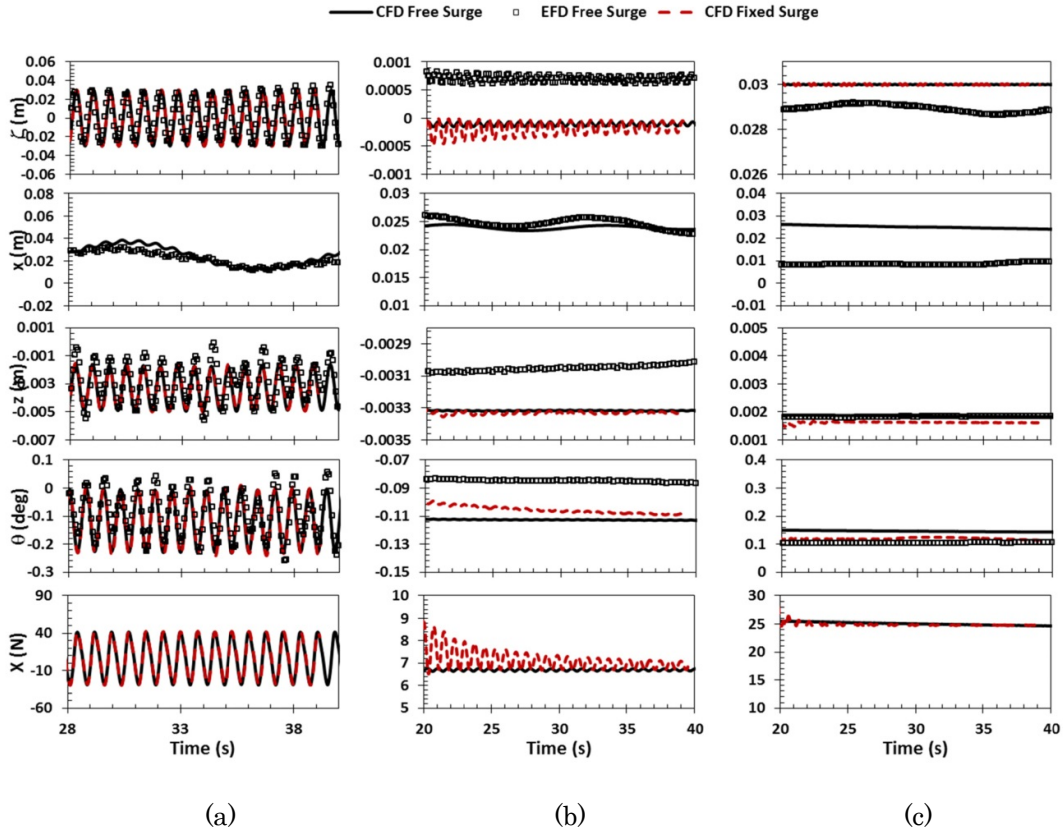


Fig. 6-2 The results for $\lambda/L=1.1$: (a) Wave signal and motions; (b) Running mean time histories; (c) Running root mean square time histories.

The results for $\lambda/L = 1.6$ and $Fr=0.142$ are shown in Figure 6-3. The maximum convergence errors are for z and θ mean values, as shown in Table 6-2. For free surge condition, the EFD x shows clearly harmonics at f_e and f_s with the amplitudes of 0.24A and 0.31A, respectively. The experimental z and θ show similar pattern to those for case $\lambda/L = 1.1$ but with larger amplitude such that z and θ oscillate at 0.88A and 0.85Ak, respectively. The EFD mean value of axial force is 5.98 N, introducing 1.6N added resistance for $\lambda/L = 1.6$ which is less than the added resistance for $\lambda/L = 1.1$. Thus, the wave condition has become far from the point to make maximum resistance on the ship.

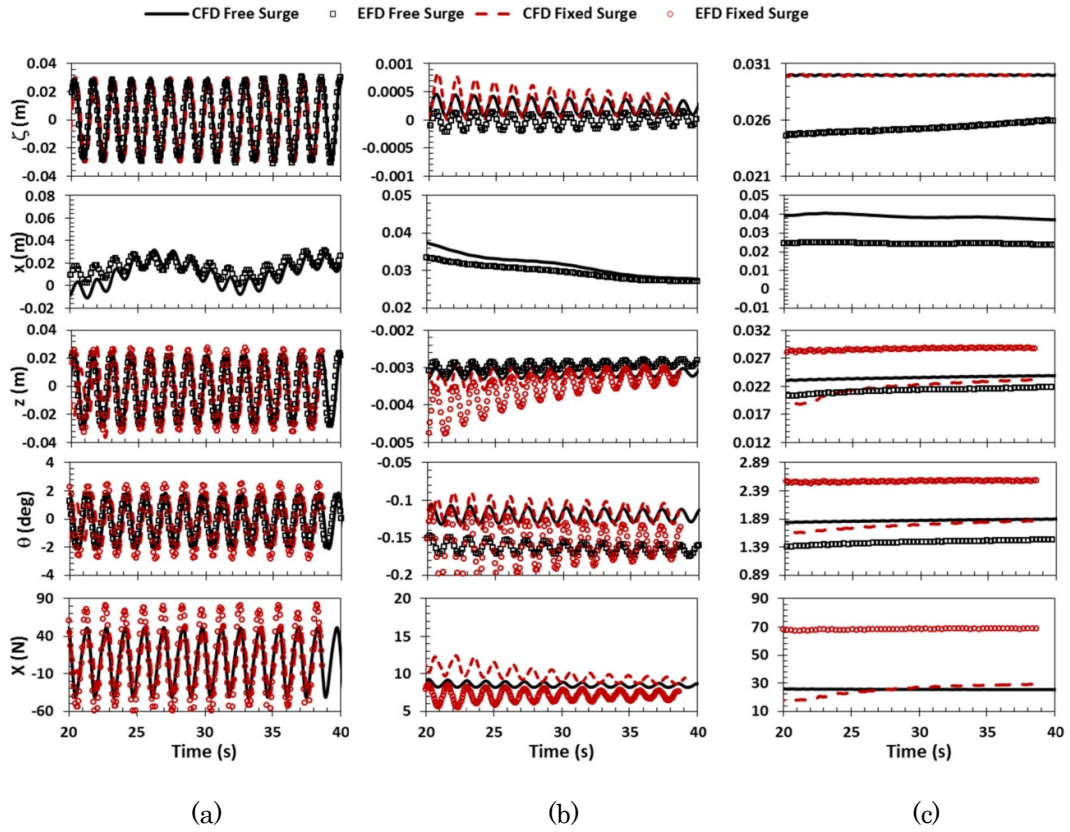


Fig. 6-3 The results for $\Lambda/L=1.6$: (a) Wave signal and motions; (b) Running mean time histories; (c) Running root mean square time histories.

For fixed surge condition, EFD amplitudes of z and θ are $0.90A$ and $1.2Ak$. Thus, the EFD heave amplitude is similar to its value for free surge but the measured pitch amplitude is 40% larger. The CFD results are converged with the average error of 3.21%Ave/5.28%Ave for mean values and 0.55%Ave/0.45%Ave for amplitudes with large convergence errors for z and θ , as shown in Table 6-2. For free surge condition, CFD predicts x with similar harmonics observed in EFD data. The x amplitude at f_e is under predicted by less than 1%D introducing remarkable agreement with EFD. The CFD z and θ responses show fairly close agreement with EFD with the amplitude of $0.84A$ and $0.94AK$, respectively. CFD over predicts the mean value of axial force by 40%D and

accordingly the added resistance. The CFD results for fixed surge condition shows fairly similar values for motions and axial force.

6.2.2 Motion Responses

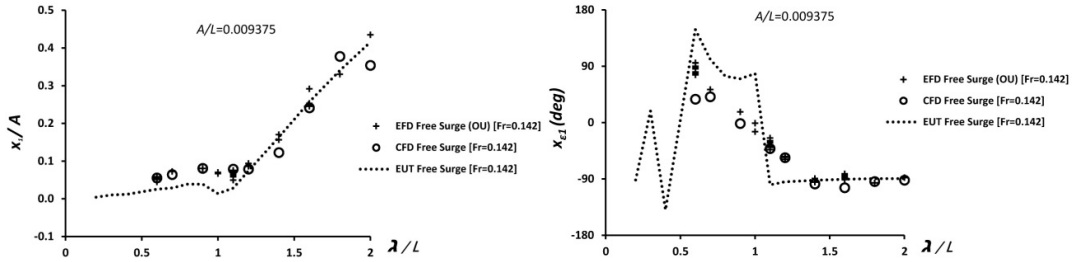


Fig. 6-4 1st harmonic amplitude and phase responses of surge motion at Fr=0.142.

Figure 6-4 shows 1st harmonics of EFD and CFD surge amplitude x_1/A and corresponding phase $x_{\varepsilon 1}$ for free surge condition cases at Fr=0.142. The EFD x_1/A is fairly constant for $\lambda/L < 1.2$ and then increases gradually to 0.4351 at $\lambda/L = 2.0$. The EFD $x_{\varepsilon 1}$ is about -90 deg for long waves introducing the surge response is zero when the wave crest is located at center of gravity. The phase reaches to 90 deg for $\lambda/L = 0.6$. For both x_1/A and $x_{\varepsilon 1}$, the repeated tests show fairly good repeatability. Note that the mean value x_0 cannot be discussed as it is strongly dependent on EFD external force F_0 which is not recorded in the experiment for the wave cases. The CFD predicts very well the trend of x_1/A and $x_{\varepsilon 1}$. The error of CFD simulation compared to the average of EFD repeated test values is listed in Table 6-3. The average error of CFD simulation is 12.3%D and 3.6%2 π for x_1/A and $x_{\varepsilon 1}$, respectively.

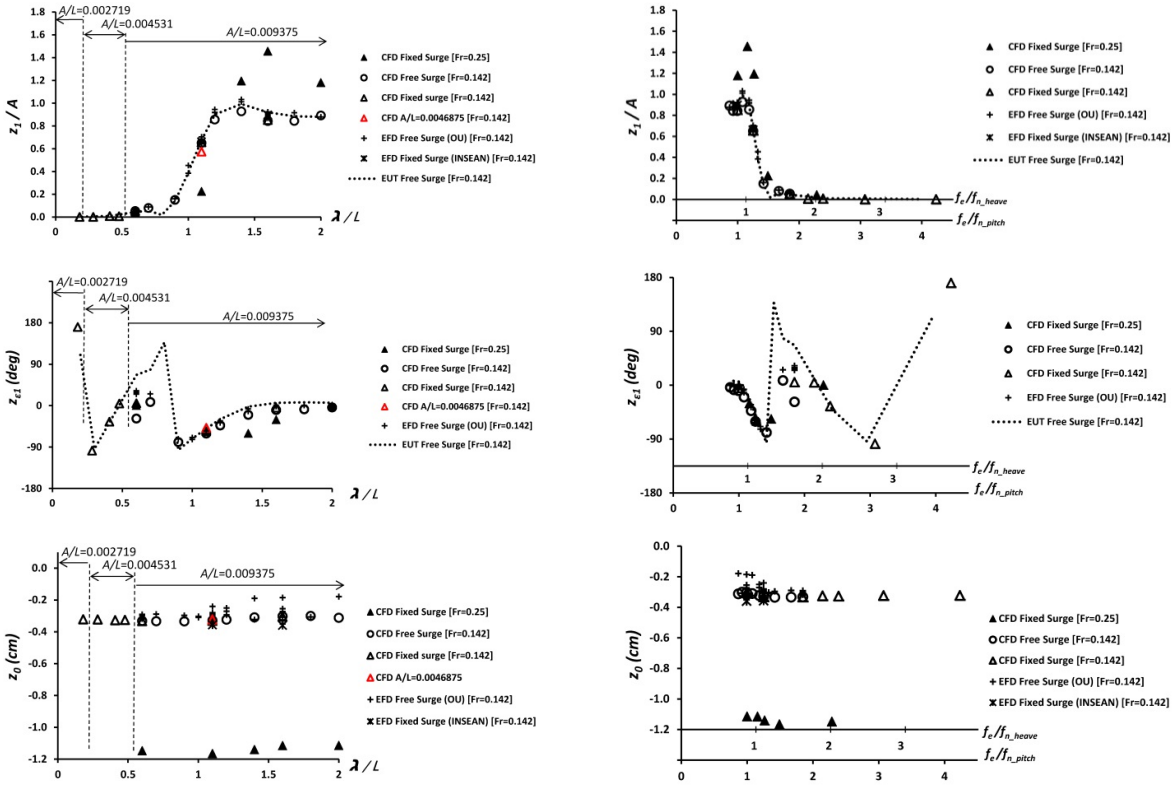


Fig. 6-5 1st harmonic amplitude, phase responses and mean value of heave motion at $Fr=0.142$ and 0.25 .

Figure 6-5 shows 1st harmonic of heave amplitude z_1/A and corresponding phase $z_{\varepsilon 1}$ and mean value z_0 for CFD compared with EFD data for free and fixed surge at $Fr=0.142$. The CFD results for $Fr=0.25$ with fixed surge are also shown in Figure 6-5. For free surge condition at $Fr=0.142$, z_1/A increases gradually by increasing λ/L and reaches 1.0 for long waves where the ship moves up and down with the wave. There is a peak for $\lambda/L = 1.4$ near to $f_e = f_z$ condition. The $z_{\varepsilon 1}$ value indicates zero phase lag for long waves decreasing slowly to -90 deg for $\lambda/L=1$ condition and reaching to zero again at short waves. The z_0 value is about -0.30 cm close to the sinkage value in calm water. The repeated tests show scattered data for some wave length conditions, as shown in

Table 6-5. In particular, z_1/A at $\lambda/L = 0.6$ is scattered around the mean value by 7%D. The scattered value is computed by $\sum_{i=1}^n |D_i - D|/D$ where D_i is the data at i^{th} repeated tests and D is the averaged data. The EFD results for fixed surge show negligible effect of surge on the heave motion. The CFD simulations at $\text{Fr}=0.142$ predicts the trend for z_1/A and $z_{\varepsilon 1}$ with $E=7.06\%D / 2.95\%D$ and $E=3.8\%2\pi / 7.8\%2\pi$ for free/fixed surge, respectively, as shown in Table 6-2 and Table 6-3. CFD follows EFD trend for z_0 with the average errors of 11%D for both free and fixed surge excluding the error for $\lambda/L=2.0$ which is very large as the EFD data is unexpectedly too small. The CFD simulations for the higher ship speed show that the peak for z_1/A is significantly larger for $\text{Fr}=0.25$ and occurs in longer wave length region at $\lambda/L= 1.6$ and the phase changes slightly with speed. Also, z_0 values increase to the dynamic sinkage at $\text{Fr}=0.25$.

Figure 6-6 shows 1st harmonic of pitch amplitude θ_1/Ak and corresponding phase $\theta_{\varepsilon 1}$ and mean value θ_0 for CFD and EFD data for free and fixed surge at $\text{Fr}=0.142$. The CFD results for $\text{Fr}=0.25$ with fixed surge are also shown in Figure 6-6. For free surge condition at $\text{Fr}=0.142$, the EFD θ_1/Ak increases with increasing λ/L and reaches nearly to Ak for long waves with a small peak. $\theta_{\varepsilon 1}$ is nearly 90 deg for long waves such that the pitch response is in phase with wave slope. Abrupt transition is observed around $\lambda/L=0.7$ for the pitch phase. The θ_0 data is significantly scattered but the average value is negative for all conditions i.e. the ship is at bow down position in average. Comparing the free and fixed surge show quite different θ_1/Ak for $\lambda/L=1.6$ while the phase and mean values are very close. This might introduce undesirable difference in static condition of the model for fixed surge tests. The CFD θ_1/Ak and $\theta_{\varepsilon 1}$ predictions at $\text{Fr}=0.142$ follow closely the EFD trend with $E=4.2\%D$ and $E=5.5\%2\pi$, respectively, while larger error for θ_1/Ak is obtained for fixed surge cases, as shown in

Table 6-3 and 6-4. The CFD θ_0 values show fairly large errors as the EFD data is significantly scattered (Table 6-5). The θ_1/Ak and θ_{e1} values at $Fr=0.25$ are fairly similar to those for $Fr=0.142$ but θ_0 is larger as it is near the dynamic trim at $Fr=0.25$.

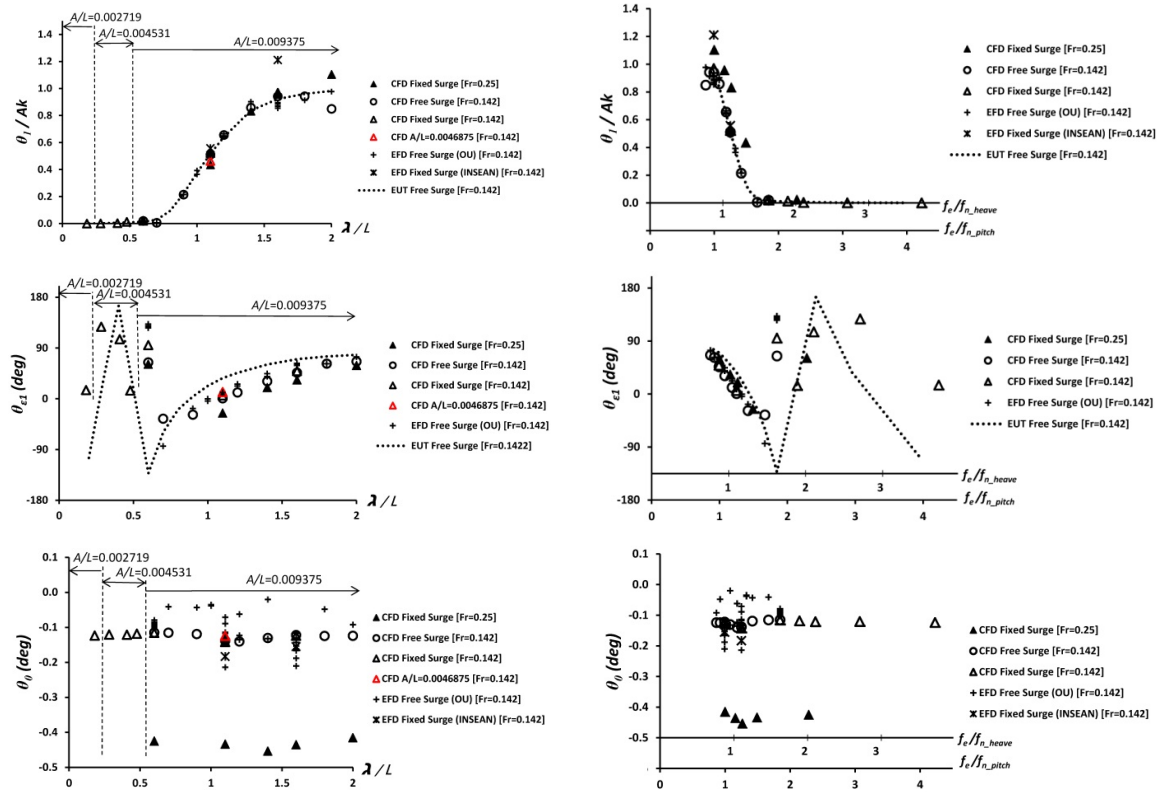


Fig. 6-6 1st harmonic amplitude, phase responses and mean value of pitch motion at $Fr=0.142$ and 0.25 .

Table 6-3 Prediction errors for free surge condition for CFD and EUT simulations.

EFD source	λ/L	x _l /A		x _{el} (deg.)		z ₀ (cm)	z _l /A		z _{el} (deg.)		θ ₀ (deg.)	θ _l /Ak		θ _{el} (deg.)		C _{aw}	
		PF	CFD	PF	CFD		CFD	PF	CFD	PF		CFD	PF	CFD	PF	CFD	PF
OU	0.6	53.11	-1.65	-17.38	13.61	-9.39	27.35	12.55	-10.97	15.3	-22.31	27.84	-7.13	72.19	17.57	21.23	34.75
	0.7	60.73	11.58	-13.35	3.24	-15.24	36.49	10.04	-14.67	4.91	-181.7	-429.3	-1.69	-6.93	-13.52	14.52	29.21
	0.9	52.15	-0.2	-14.71	5.17	-12.77	13.01	6.13	6.7	1.92	-177.0	-3.31	0.4	-5.98	3.03	-22.65	6.01
	1.1	55.79	-22.61	17.97	1.97	-11.15	-0.62	3.09	-2.06	1.02	-7.38	-1.71	-0.43	-7.46	2.54	-20.08	6.41
	1.2	16.86	11.8	10.64	-0.03	-19.16	2.79	7.63	-1.69	2.05	-31.41	1.72	-0.59	-6.23	3.45	-25.54	-3.97
	1.4	-0.07	25.05	-0.07	1.62	-20.93	2.84	9.24	-2.08	2.84	-71.61	6.39	3.97	-5.23	3.04	-38.74	-24.9
	1.6	-1.36	5.04	1.05	4.81	-4.16	-3.15	5.51	-1.81	2.49	23.00	-5.25	-7.46	-2.55	4.12		
	1.8	-2.98	-14.23	-1.91	-0.61	2.14	3.25	7.78	-1.79	2.37	-159.1	-5.03	-3.15	-3.65	-0.04	-26.15	-36.39
	2	4.49	18.64	0.41	1.12	-74.81	-0.22	-1.6	-1.89	0.93	-34.75	-0.48	13.06	-1.00	2.24		
	E	27.5	12.31	8.61	3.58	18.86	9.97	7.06	4.85	3.76	78.71	53.45	4.21	12.36	5.5	24.13	20.23

Table 6-4 Prediction errors for CFD simulations for fixed surge condition.

EFD source	λ/L	z ₀ (cm)		z _l /A		z _{el} (deg.)		θ ₀ (deg.)		θ _l /Ak		θ _{el} (deg.)		C _{aw}		X _l (N)	
		D	E%D	D	E%D	D	E%360°	D	E%D	D	E%D	D	E%D	D	E%360°	D	E%D
NTNU	0.1810	-	-	-	-	-	-	-	-	-	-	-	-	3.4376	-1.92	-	
	0.2833	-	-	-	-	-	-	-	-	-	-	-	-	2.7763	10.68	-	
	0.4077	-	-	-	-	-	-	-	-	-	-	-	-	2.3605	-13.71	-	
	0.4782	-	-	-	-	-	-	-	-	-	-	-	-	2.5495	6.39	-	
INSEAN	0.6	-	-	-	-	-	-	-	-	-	-	-	-	-	-	-	-
	1.1	-0.3567	7.24	0.6611	0.85	-93.8711	-10.56	-0.1831	22.43	0.5573	6.33	-5.6495	-3.19	6.8068	-3.80	37.167	36.65
	1.6	-0.3593	15.23	0.8968	5.04	-22.9783	-5.08	-0.1549	19.85	1.2108	19.99	39.2459	-2.68	2.8893	-24.25	68.375	34.05
E		11.24		2.95		7.82		21.14		13.16		2.94		10.12		35.35	

Table 6-5 Scatter of EFD data (OU, free surge) (% of average value)

λ/L	No. of data	x _l /A	x _{el} (deg.)	z ₀ (cm)	z _l /A	z _{el} (deg.)	θ ₀ (deg.)	θ _l /Ak	θ _{el} (deg.)	C _{aw}
0.6	10	7.08	10.70	-4.07	6.71	19.20	-16.05	5.57	3.64	23.03
1.1	9	17.40	-28.57	-18.76	4.81	-4.73	-44.72	3.25	25.35	9.12
1.2	3	5.35	-3.47	-7.78	1.86	-7.43	-41.88	1.94	9.91	1.88
1.4	2	0.01	2.92	0.07	0.01	2.72	0.06	0.01	2.62	0.18
1.6	8	0.04	4.86	0.10	0.03	1.16	0.04	0.02	1.60	0.14
0.7,0.9,1.8,2.0	1	-	-	-	-	-	-	-	-	-

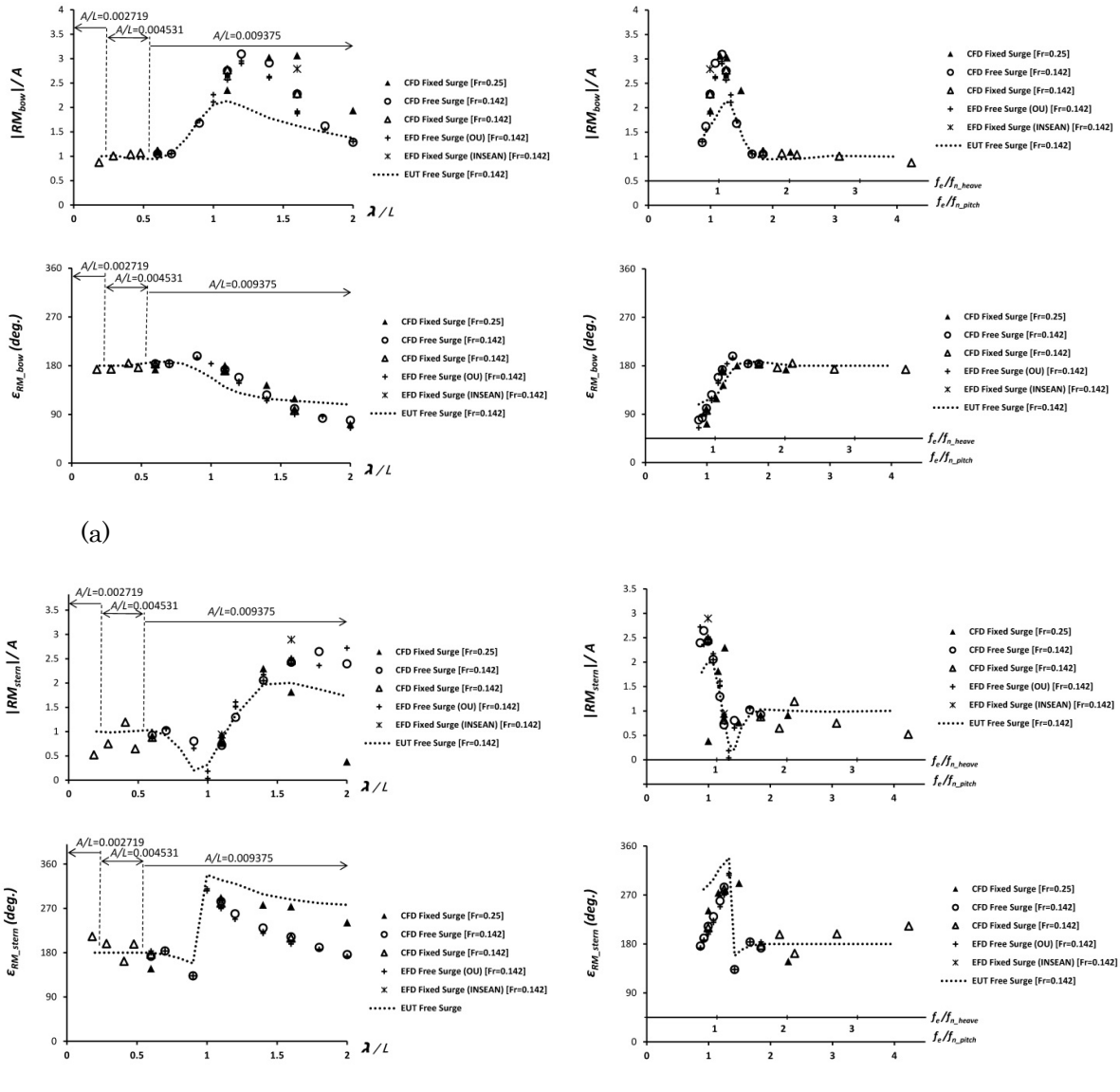


Fig. 6-7 Amplitude and phase of relative motion for $Fr=0.142$ and 0.25 : (a) bow; (b) stern.

The relative motion at bow and aft are also determined as follow and their amplitude and phase are estimated from Eq. (34) and (35) and validated against EFD data:

$$RM_{Bow} =$$

$$z_0 + z_1 \cos(2\pi f_e t + z_{\varepsilon 1}) + x_G \sin(\theta_0 + \theta_1 \cos(2\pi f_e t + \theta_{\varepsilon 1})) - A \cos(2\pi f_e t + \gamma_b) \quad (34)$$

$$RM_{Stern} =$$

$$z_0 + z_1 \cos(2\pi f_e t + z_{\varepsilon 1}) - (L - x_G) \sin(\theta_0 + \theta_1 \cos(2\pi f_e t + \theta_{\varepsilon 1})) - A \cos(2\pi f_e t + \gamma_s) \quad (35)$$

where $(z_0, z_1, z_{\varepsilon 1})$ and $(\theta_0, \theta_1, \theta_{\varepsilon 1})$ are the heave and pitch mean value and 1st amplitude and the corresponding phase. Also, γ_b and γ_s are incident wave phase at bow and aft at $t=0$. Figure 6-7 shows the amplitude and phase of EFD and CFD relative motion at bow (RM_{bow}) and stern (RM_{stern}) estimated from Eq. (34) and Eq. (35). The largest amplitude of EFD RM_{bow} occurs around $\lambda/L=1.2$ where the phase lag between the wave signal and bow motion is close to 180 deg and also z_1/A and θ_1/Ak are large (see Figure 6-3 and 6-4) the combination of which results in large RM_{bow} . The maximum RM_{stern} happens for long waves where the stern is 180 deg out of phase with wave at stern and the motions are large enough to produce large stern motion. The CFD relative motions at $Fr=0.142$ agree very well with EFD. The results at the higher ship speed show that the peak of RM_{bow} shifts to longer waves similar to heave motion but the peak of RM_{bow} is similar to that for $Fr=0.142$.

6.2.3 Forces, moments and added resistance responses

The first and second harmonics of EFD and CFD axial forces and the corresponding phases are plotted in Figure 6-8. The EFD data for fixed surge shows that the 1st harmonic amplitude of X_{TF} is 37N at $\lambda/L=1.1$ increasing to 68N at $\lambda/L=1.6$ while the 2nd harmonic shows very small amplitude for both wave length condition. CFD under predicts the 1st harmonic amplitude of X_{TF} by average of 35%D at $Fr=0.142$. The components of 1st harmonic X_{TF} reveals that X_{FK} is very large compared to X_{DF} in long

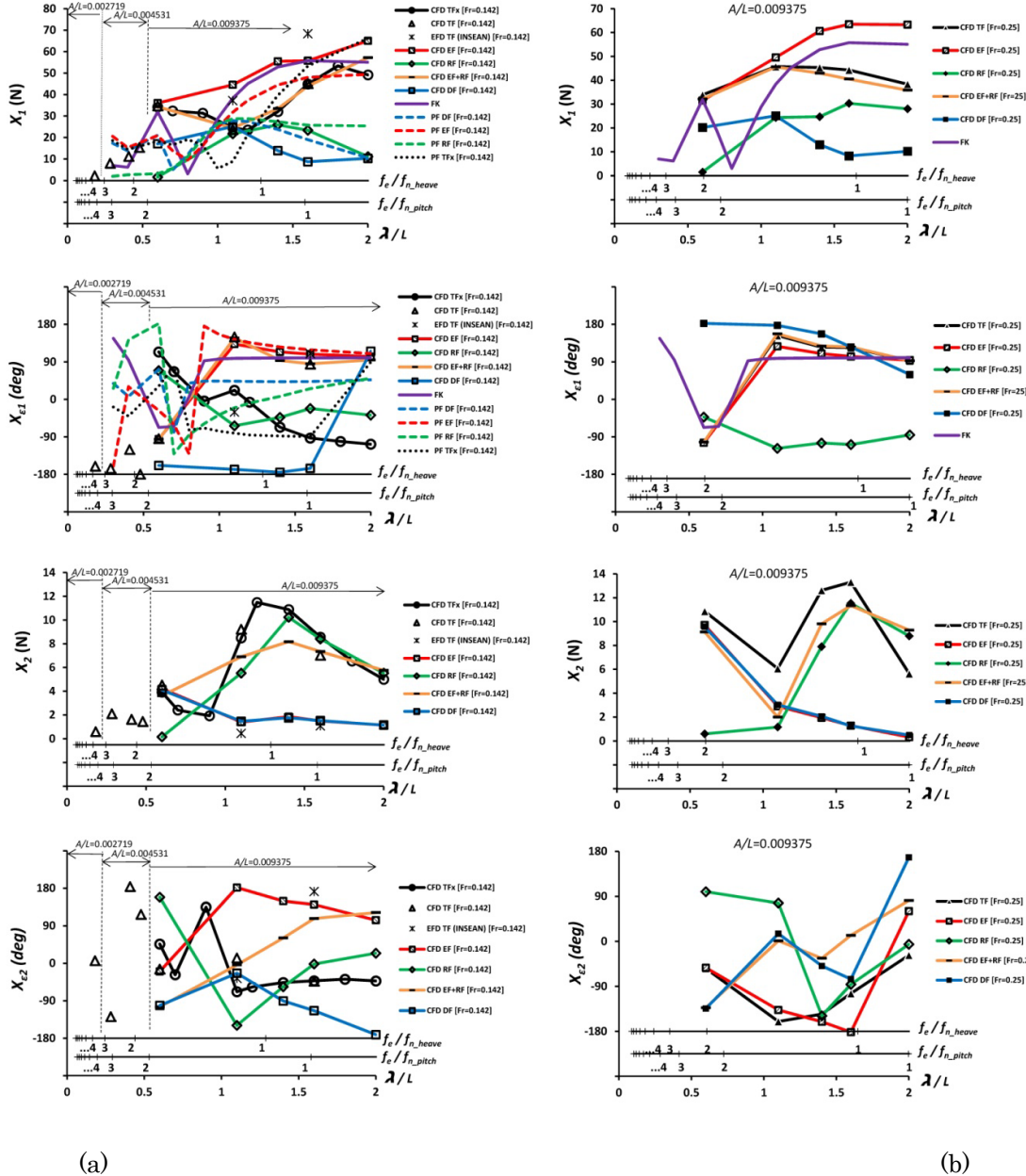


Fig. 6-8 1st and 2nd harmonic amplitude and phase of surge force:
 (a) Fr=0.142; (b) Fr= 0.25.

waves and has a peak near $\lambda/L=1.33$ which causes a peak for X_{EF} . Also there is a peak for X_{RF} near the resonance condition. The summation of X_{EF} and X_{RF} amplitudes

considering their phase difference estimates X_{TF} very well with the average differences of 4.67% and 2.23% for free and fixed surge condition, respectively, as shown in Table 6-6 and Table 6-7. The 2nd harmonic of CFD axial force components shows that the nonlinearity originates from X_{RF} in long waves and from X_{DF} in very short waves. The summation of the components estimates the 2nd harmonic amplitude of X_{TF} with average difference of 16% for both fixed and free surge (see Table 6-6 and Table 6-7), showing interaction between higher harmonics of the components. Since the 2nd harmonic amplitude of X_{TF} are about 50% of the 1st harmonic amplitudes, the large errors for higher order prediction might have a strong influence on the axial force prediction and accordingly surge motion. The CFD results for the higher ship speed shows 1st harmonic amplitudes of X_{FK} and X_{DF} are the same as those for $Fr=0.142$, confirming that EF is fairly independent of ship speed. However, the peak of X_{RF} shifts to longer waves near to the resonance condition at $Fr=0.25$ which changes TF trend.

Table 6-6 Difference between total CFD force/moment with free surge condition and the combination of wave exciting and radiation force/moment for $Fr=0.142$.

λ/L	$X(N)$		$Z(N)$		$M(Nm)$		$X(N)$			$Z(N)$			$M(Nm)$		
	TF _x	$\Delta\%TF_x$	TF _x	$\Delta\%TF_x$	TF _x	$\Delta\%TF_x$	TF _x	X_2/X_1	$\Delta\%TF_x$	TF _x	Z_2/Z_1	$\Delta\%TF_x$	TF _x	M_2/M_1	$\Delta\%TF_x$
0.6	34.25	-0.28	34.68	1.5	26.64	-6.11	3.91	0.114	7.52	2.4	0.069	2.38	2.18	0.082	26.29
0.7	32.4	-	41.45	-	5.01	-	2.41	0.074	-	1.87	0.045	-	1.92	0.383	-
0.9	31.35	-	58.07	-	113.29	-	1.93	0.062	-	5.88	0.101	-	4.9	0.043	-
1.1	24.5	0.23	192.14	2.25	171.05	4.05	8.48	0.346	18.61	11.54	0.060	54.88	8.68	0.051	33.67
1.2	23.55	-	228.31	-	181.73	-	11.48	0.487	-	12.36	0.054	-	9.89	0.054	-
1.4	32.05	-4.28	203.06	2.7	167.93	-0.93	10.88	0.339	24.91	10.08	0.050	49.43	7.34	0.044	-70.78
1.6	44.88	2.18	157.12	4.97	136.76	-2.52	8.56	0.191	14.19	9.43	0.060	58.77	4.9	0.036	-92.2
1.8	53.37	-	136.74	-	104.99	-	6.53	0.122	-	7.9	0.058	-	4.32	0.041	-
2	49.16	-16.39	127.09	-2.19	74.83	40.82	5	0.102	-15.13	7.48	0.059	59.22	2.98	0.040	-90.96
$ \bar{\Delta} $	4.67		2.72		10.89			16.07			44.93			62.78	

Table 6-7 Difference between total CFD force/moment with fixed surge condition and the combination of wave exciting and radiation force/moment for $Fr=0.142$.

λ/L	$X_i(N)$		$Z_i(N)$		$M_i(Nm)$		$X_d(N)$			$Z_d(N)$			$M_d(Nm)$		
	TF	$\Delta\%TF$	TF	$\Delta\%TF$	TF	$\Delta\%TF$	TF	X_d/X_i	$\Delta\%TF$	TFx	Z_d/Z_i	$\Delta\%TF$	TF	M_d/M_i	$\Delta\%TF$
0.6	34.7	1.01	33.95	-0.6	28.1	-0.57	4.52	0.130	19.86	2.61	0.077	10.22	2.71	0.096	40.87
1.1	23.73	-3	193.61	2.99	175.36	6.41	9.22	0.389	25.14	9.23	0.048	43.55	8.02	0.046	28.25
1.6	45.11	2.67	160.55	7	140.85	0.45	7.02	0.156	-4.62	6.62	0.041	41.26	4.09	0.029	-130.02
$ \bar{\Delta} $	2.23		3.53		2.48		16.54			31.68			66.38		

Table 6-8 Difference between total CFD force/moment with fixed surge condition and the combination of wave exciting and radiation force/moment for $Fr=0.25$.

λ/L	$X_i(N)$		$Z_i(N)$		$M_i(Nm)$		$X_d(N)$			$Z_d(N)$			$M_d(Nm)$		
	TF	$\Delta\%TF$	TF	$\Delta\%TF$	TF	$\Delta\%TF$	TF	X_d/X_i	$\Delta\%TF$	TFx	Z_d/Z_i	$\Delta\%TF$	TF	M_d/M_i	$\Delta\%TF$
0.6	33.88	5.14	45.42	-1.88	22.13	1.77	10.86	0.321	15.91	6.23	0.137	-5.25	6	0.271	7.64
1.1	45.75	0.32	166.43	-0.73	208.7	-3.51	6.06	0.132	67.08	11.78	0.071	34.19	11.17	0.054	42.42
1.4	45.32	5.13	362.33	0.68	226.96	1.36	12.61	0.278	22.27	12.9	0.036	85.39	10.78	0.047	-54.41
1.6	44.3	8.58	368.53	0.57	189.67	-30.12	13.3	0.300	14.8	11.13	0.030	-28.56	6.82	0.036	-161.31
2	38.37	6.59	222.36	1.4	130.73	0.62	5.63	0.147	-64.86	1.88	0.008	-582.07	2.74	0.021	-389.56
$ \bar{\Delta} $	5.15		1.05		7.48		36.98			147.09			131.07		

The EFD and CFD added resistance trend is shown in Figure 6-9. For free surge, the EFD added resistance C_{aw} shows a peak near $\lambda/L=1.1$. The EFD repeated tests do not show good repeatability such that the data are scattered for most of wave conditions. In particular, the added resistance at $\lambda/L=1.1$ is scattered around $\pm 10\%$ its average value as shown in Table 6-5. EFD with fixed surge shows the added resistance coefficient increases slightly with decreasing λ/L for very short waves. Comparing the EFD added resistance with RM_{bow} (shown in Figure 6-7) reveals a significant correlation between them such that the peak of the added resistance occurs near maximum RM_{bow} condition.

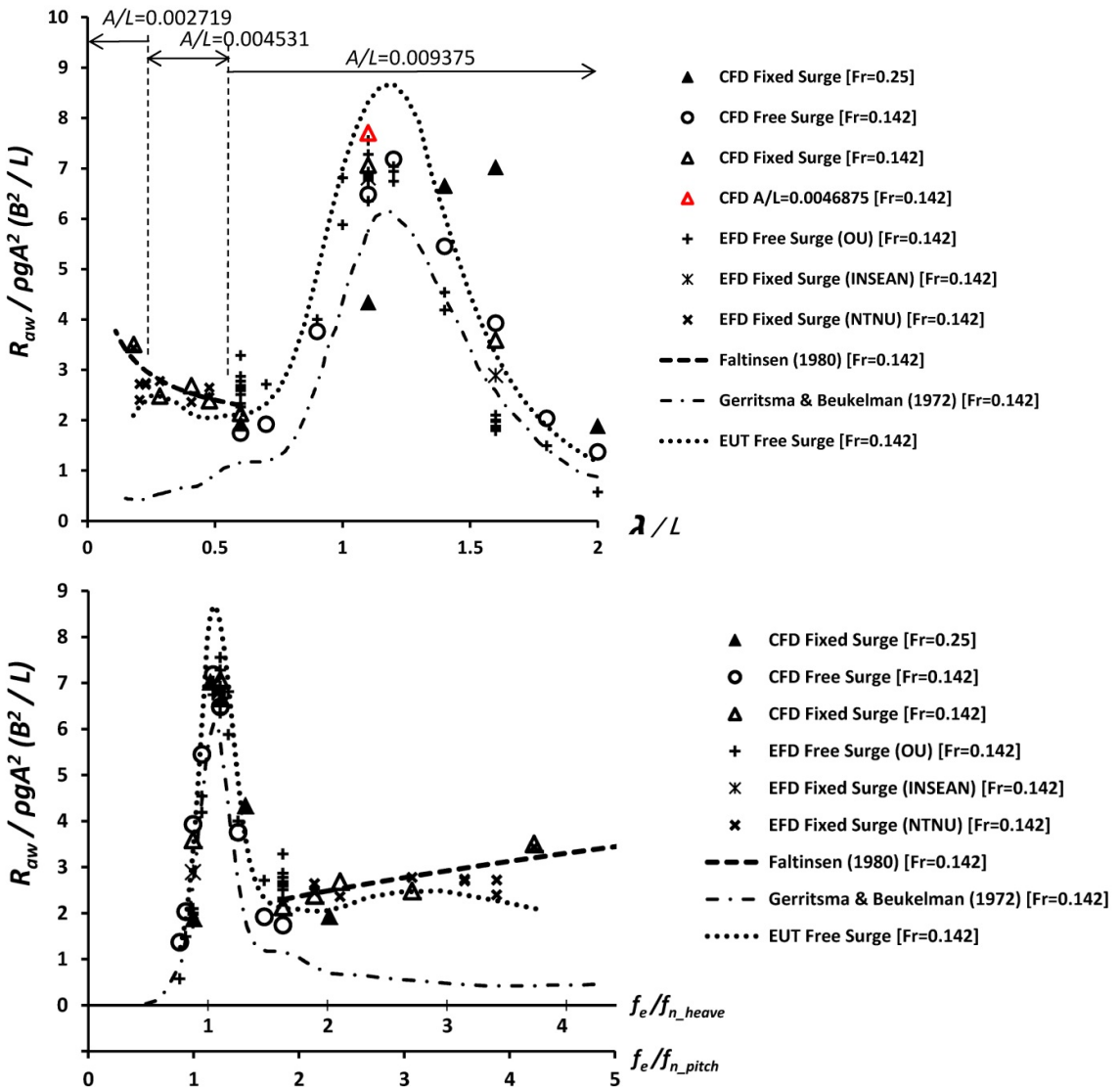


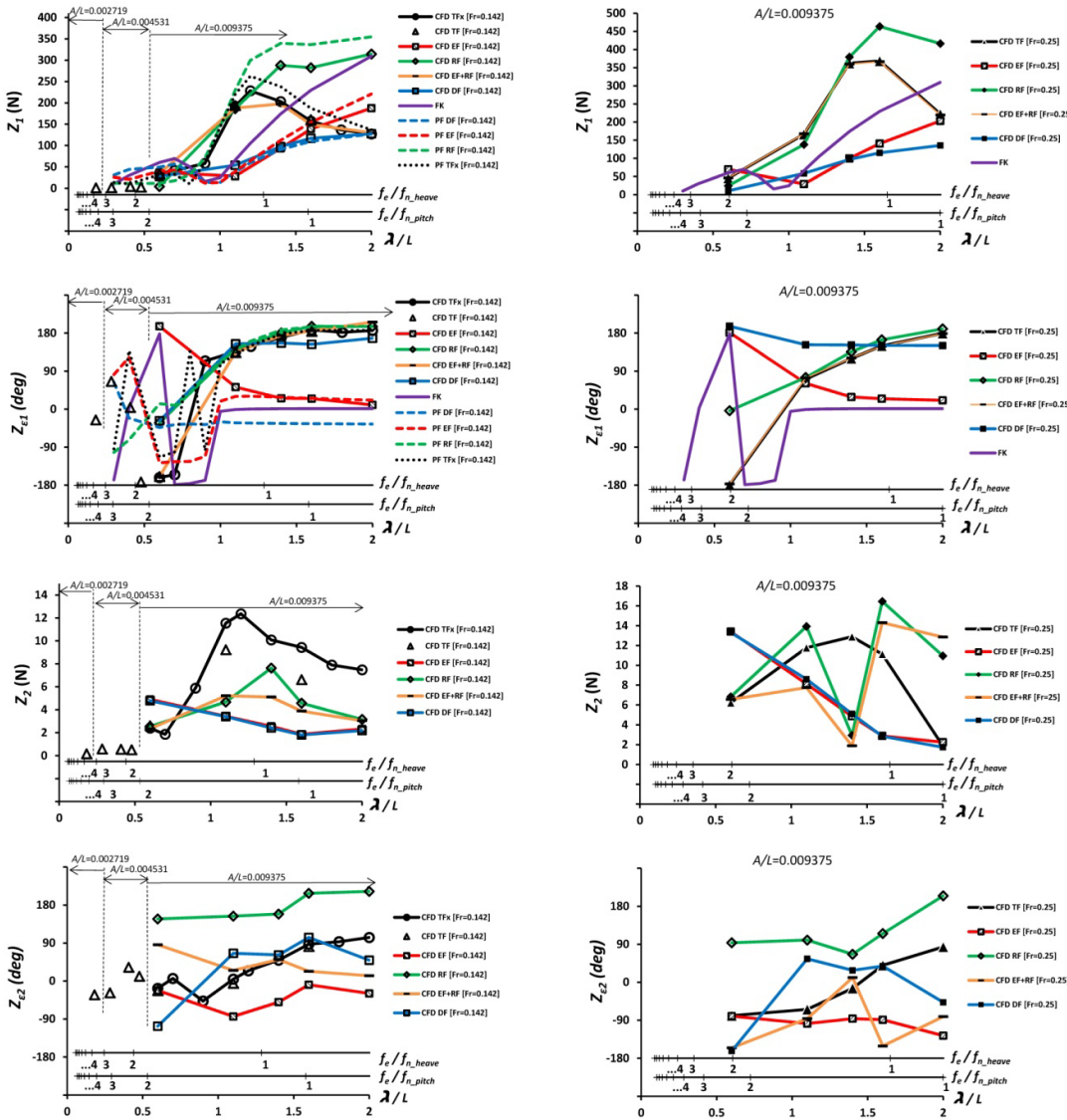
Fig. 6-9 Added resistance at Fr=0.25 and 0.142.

The RM_{stern} does not show correlation with EFD added resistance but it is important for slamming at stern and propeller emergence. The CFD simulation at Fr=0.142 under predicts the added resistance for $\lambda/L < 1.2$ and over predicts for $\lambda/L > 1.2$ with the average error of 20%D. The results for fixed surge condition show similar C_{aw} , with average prediction errors of 10.12%D. The results for higher ship speed shows that

increasing speed shifts the added resistance peak to longer wave length but the peak value is not changed similar to that for RM_{bow} , confirming strong correlation of the added resistance with bow relative motion.

The first and second harmonics of heave forces and the corresponding phases are plotted in Figure 6-10. There is no EFD data as the ship model was free to heave and pitch. The CFD simulations at $Fr=0.142$ with free surge show a peak for 1st harmonic of Z_{TF} amplitude near the resonance condition. The components of 1st harmonic heave force reveals that the amplitude of Z_{EF} increases with wave length while there is a peak for Z_{RF} near the resonance condition. Z_{RF} is very large compared to Z_{EF} but it is about 180 deg out phase respect to Z_{EF} in long waves. The amplitudes of Z_{EF} and Z_{RF} and their phase differences provide a peak for Z_{TF} . The comparison of $Z_{EF}+Z_{RF}$ with Z_{TF} shows that linear summation of components estimates Z_{TF} very well with the average differences of 2.7% and 3.5% for free and fixed surge, respectively, as shown in Table 6-6 and Table 6-7. The 2nd harmonic amplitude shows that the nonlinearity is not very large near the resonance condition, about 6% of the 1st harmonic amplitude. The summation of the components estimates the 2nd harmonic amplitude of Z_{TF} with the average difference of larger than 30% for both fixed and free surge (see Table 6-6 and Table 6-7). The results for $Fr=0.25$ show that the 1st harmonic amplitudes of Z_{FK} and Z_{DF} are the same as those for $Fr=0.142$. However, the peak for Z_{RF} is larger and shifts to longer wave length near the resonance condition at $Fr=0.25$, providing larger Z_{TF} and accordingly larger heave motion as shown earlier.

The harmonics of pitch moments and the corresponding phases are plotted in Figure 6-11. The CFD simulations at $Fr=0.142$ show a peak near $\lambda/L=1.33$ for 1st harmonic amplitude of M_{TF} . The components show a peak for M_{EF} amplitude near $\lambda/L=1.33$ while



(a)

(b)

Fig. 6-10 1st and 2nd harmonic amplitude and phase of heave force:
 (a) Fr=0.142; (b) Fr= 0.25.

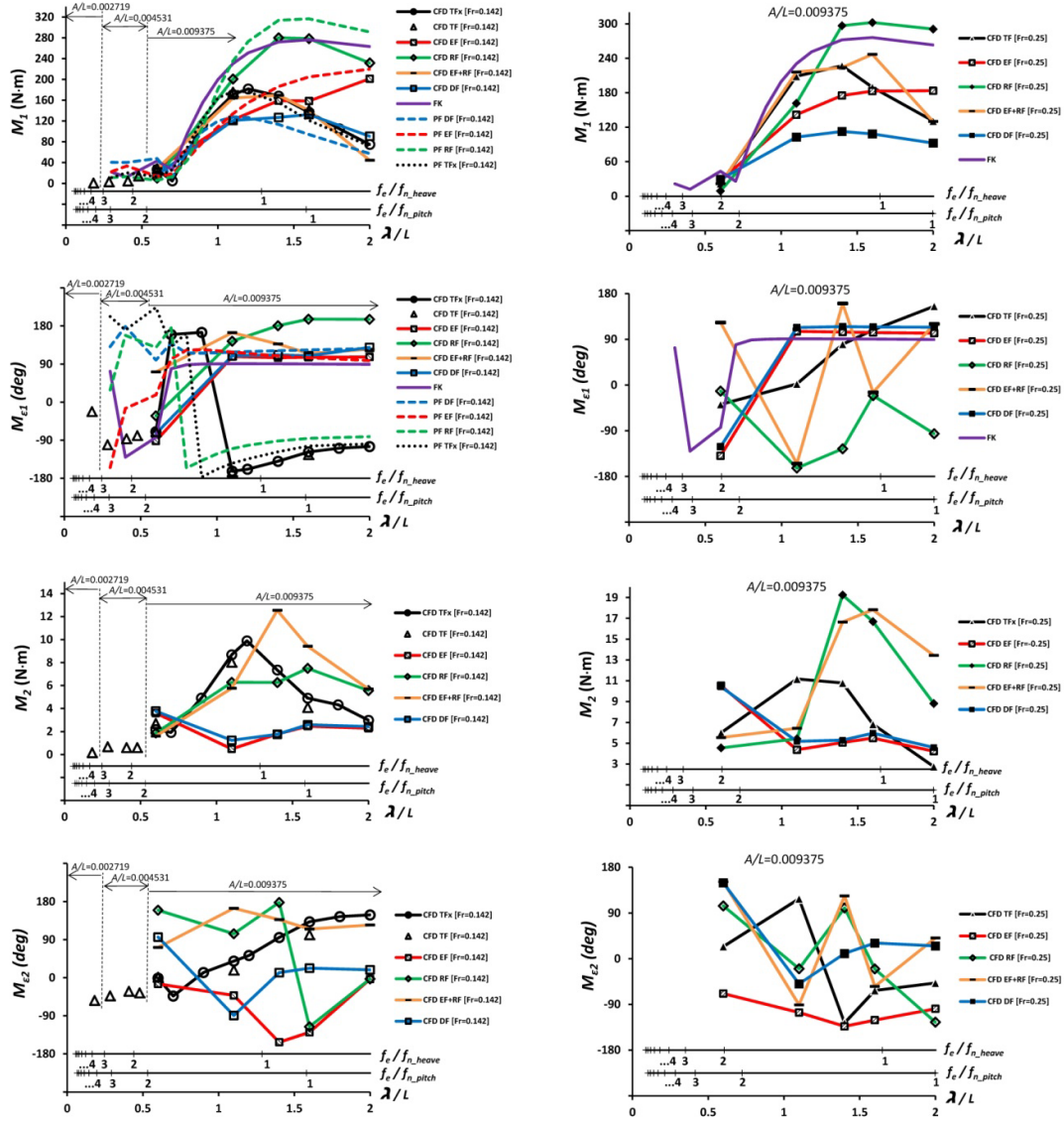


Fig. 6-11 1st and 2nd harmonic amplitude and phase of pitch moment:
 (a) Fr=0.142; (b) Fr= 0.25.

M_{RF} amplitude has a large peak near the wave length $\lambda/L=1.6$ corresponding to the resonance condition at $Fr=0.142$. There is about 90 deg phase lag between M_{EF} and M_{RF} components in long waves and 45 deg in short waves. The amplitudes of M_{EF} and M_{RF}

and their phase differences provide a peak for M_{TF} near $\lambda/L=1.33$. The summation of the components matches M_{TF} fairly well with average differences of 10.9% and 2.5% for free and fixed surge, respectively. The components of M_{EF} show that M_{FK} over predicts M_{EF} and thus M_{DF} is required for M_{EF} computation. The amplitude of 2nd order harmonics are often quite small compared to the 1st harmonic amplitudes, as shown in Table 6-6 and Table 6-7. The nonlinearity is mainly induced by radiation in long waves and diffraction in short waves. The summation of the components for 2nd order harmonic amplitudes shows about 63% difference with the total moment for both free and fixed surge. The results for the higher ship speed shows that the peak for 1st amplitude of M_{RF} shifts to longer wave and the peaks of M_{EF} and M_{RF} are insensitive to the ship speed such that the combination of them slightly changes the trend of M_{TF} .

6.2.4 Maximum responses

Maximum surge motion occurs when X_{TF} is maximum. It is confirmed that X_{TF} can be represented as the summation of X_{EF} and X_{RF} and thus the maximum surge occurs when both components are maximum. X_{EF} component is maximum around $\lambda/L=1.33$ and X_{RF} is maximum near the resonance conditions of heave and pitch. At a given speed and variant wave length, the peak for surge force/motion occurs at a wave length near both $\lambda/L=1.33$ and resonance conditions, as shown for CFD surge force/motion at $Fr=0.142$ in Figure 6-8. For variant speed and wave length, the overall peak for surge force/motion occurs when the peaks for X_{EF} and X_{RF} overlap.

For heave, Z_{EF} is maximum at long waves and Z_{RF} is maximum near the resonance condition. For a given speed and variant wave length, the peak of heave force and

accordingly heave motion occurs in long waves and near the wave length corresponding to the resonance condition as shown for both $Fr=0.142$ and $Fr=0.25$ (see Figure 6-5). For variant speed and wave length, the overall peak for heave motion occurs when the peaks for Z_{EF} and Z_{RF} overlap. This condition happens for infinite Fr based on Eq. (32). This is due the fact that increasing ship speed shifts the resonance condition to the longer wave length region. The comparison of the heave motions for $Fr=0.142$ and 0.25 shows that $Fr=0.25$ provides large heave motion since the resonance condition is shifted from $\lambda/L=1.4$ to $\lambda/L=1.6$.

For pitch, M_{EF} is maximum around $\lambda/L=1.33$ and M_{RF} is maximum near the resonance condition. For a given speed and variant wave length, the peak of pitch moment and consequently pitch motion happens at a wave length near both $\lambda/L=1.33$ and the wave length corresponding to the resonance condition, as shown for pitch motion at $Fr=0.142$ (see Figure 6-6). For variant speed and wave length, the overall peak for pitch motion occurs when the peaks for M_{EF} and M_{RF} overlap. The peaks for M_{EF} and M_{RF} coincide at $Fr=0.082$ based on Eq. (32), which is not simulated here. The pitch moments for $Fr=0.142$ and 0.25 show that the peak for M_{RF} shifts from $\lambda/L=1.6$ to $\lambda/L=2.0$ for the higher ship speed while M_{EF} at $\lambda/L=1.6$ and $\lambda/L=2.0$ are fairly similar such that M_{TF} is quite the same for both ship speeds. This results in similar values for maximum pitch for both Fr as shown in Figure 6-6.

The coincidence of the peaks for EF and RF increases the ship motions and accordingly the bow and stern motions. However, the bow and stern relative motions might not increase as they do also depend on the phase between the wave and the bow and stern motions. Figure 6-7 shows that the peak of RM_{bow} is similar to that for $Fr=0.142$ even though the heave motion is significantly larger for $Fr=0.25$. This is due to

the fact that the bow motion is not 180 deg out of phase with the wave at bow, providing not very large relative motion. The similar RM_{bow} for both ship speeds provides similar added resistance value for both speeds as well (see Figure 6-9). Similar to RM_{bow} , the relative motions at stern are not larger for $Fr=0.25$.

6.2.5 Comparison with PF predictions

The predicted ship motions at $Fr=0.142$ for EUT approach are shown in Figure 6-4 to 6-6. x_1/A and $x_{\varepsilon 1}$ are fairly well predicted for $\lambda/L > 1.0$ while the x_1/A is under predicted for short waves due to the under prediction of axial diffraction force (see Figure 6-8). z_1/A and θ_1/Ak show good agreement with EFD for most of the wave length conditions while $z_{\varepsilon 1}$ and $\theta_{\varepsilon 1}$ show some difference with EFD near to abrupt transition condition. The mean value of heave and pitch motions are not predicted by EUT. The average prediction errors for x_1/A , z_1/A and θ_1/Ak are 27%D, 10%D and 53%D which are larger compared to the errors for CFD simulation (see Table 6-3). The average error for $x_{\varepsilon 1}$ and $\theta_{\varepsilon 1}$ are 8.6%D and 12.36%D which are about twice than those for CFD while the phase for heave is predicted with similar error as CFD.

The EUT results for relative motions are shown in Figure 6-7. To evaluate the relative motion, the mean value of heave and pitch are required as shown in Eq. (24) and Eq. (25). Since the mean value of heave and pitch motions are not predicted by EUT, it is assumed that EUT and CFD mean values for heave and pitch are the same. EUT and CFD have good agreement for amplitudes of bow relative motion in the short and long waves while EUT shows under prediction for the bow relative motion near the resonance condition. The large differences between EUT and CFD for bow relative

motion are originated from differences between EUT and CFD heave and pitch phases.

The large errors for EUT provide large differences for the added resistance. For stern relative motion, the agreement is good near the resonance condition while large differences are observed for both short and long waves.

The added resistance values are predicted using EUT and Gerritsma and Beukelman method (GB) reported in Bingjie and Steen (2010). Also, the asymptotic formula (Faltinsen, 1980) is used to predict the added resistance in short waves. The results show that EUT and GB predict the trend while the values are over/under predicted near the peak by EUT/GB. Also, EUT predicts the added resistance in short waves as it includes the diffraction component in the computation while GB neglects the effect of wave diffraction due to the bow of the ship which has significant contribution to added resistance in short waves. The average error of EUT for added resistance is about 24%D, as shown in Table 6-3. The asymptotic formula (Faltinsen, 1980) computations show good prediction of added resistance for very short waves where the wave diffraction force is dominant.

The comparison of CFD and EUT forces are shown in Figure 6-8, 6-10 and 6-11. The Froude Krylov component is the same for both CFD and EUT as both integrate the given wave-induced pressure on the hull. The 1st harmonic amplitude and corresponding phase of X_{DF} are not predicted well by EUT which cause under prediction of axial X_{EF} in short waves. EUT also slightly over predicts the amplitude of X_{RF} in long waves and shows errors for phases suggesting that the added mass and added damping combination used for X_{RF} computation in potential flow works not very well for axial force. Due to the errors in the predictions of amplitudes and phases of the components, X_{TF} is significantly under predicted in short waves which causes the under prediction of

surge motion in short waves, as shown in Figure 6-4. The CFD and EUT heave forces are presented in Figure 6-10. The 1st harmonics amplitude of Z_{EF} and Z_{RF} show that the amplitudes are slightly over predicted in long waves. The over prediction of Z_{EF} and Z_{RF} provides slightly larger Z_{TF} in long waves compared to that for CFD. The CFD and EUT pitch moments are plotted in Figure 6-11. The EUT predicts the trends of all the components very well. The amplitudes of M_{EF} and M_{RF} are slightly over predicted and the phase of M_{RF} is also not predicted well. However, the summation of M_{EF} and M_{RF} considering their phases provides very good agreement for M_{TF} . Overall, it can be concluded that the composition of forces and moments work fairly well for heave and pitch but not for surge.

6.2.6 Wave amplitude effect

In Figure 6-5, 6-6 and 6-9, the fixed surge CFD results of $A/L=0.0046875$, which is half of $A/L=0.009375$ in the other cases, at $\lambda/L=1.1$ are also listed. Generally, the wave amplitude effect only has small influence on these responses since they are non-dimensionlized by the wave amplitude. For the 1st harmonic amplitude of heave motion z_1/A , the value of $A/L=0.009375$ is slightly smaller than the $A/L=0.0046875$ one. The 1st harmonic amplitude of pitch motion θ_1/Ak shows closer values for both wave amplitudes. Their phases and mean values are very close values. The added resistance of $A/L=0.0046875$ is a little bit larger than the $A/L=0.009375$ value and the EFD data.

6.3 BALLAST CONDITION

6.3.1 Time history

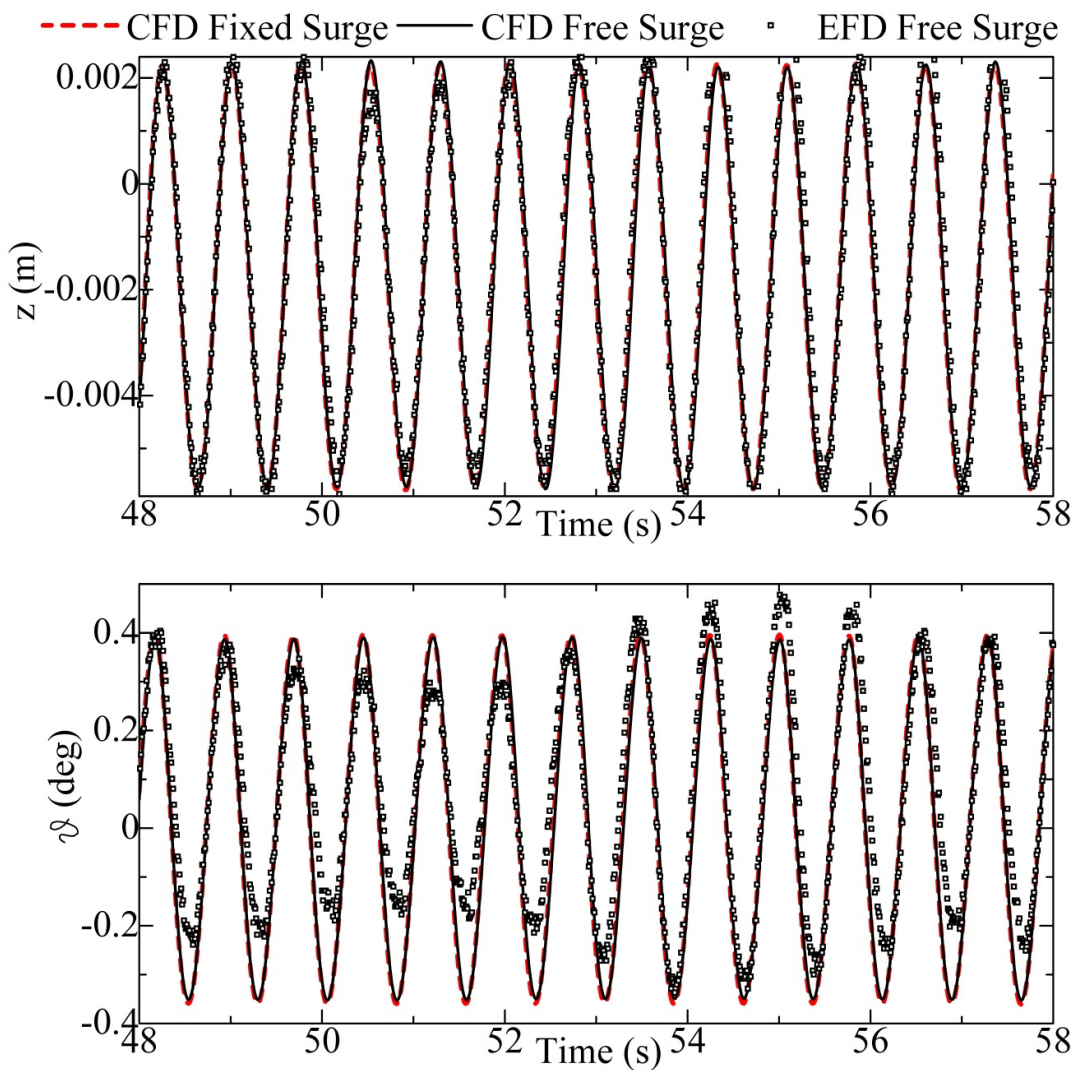


Fig. 6-12 Time history of heave and pitch motion for ballast condition at $\lambda/L=0.6$

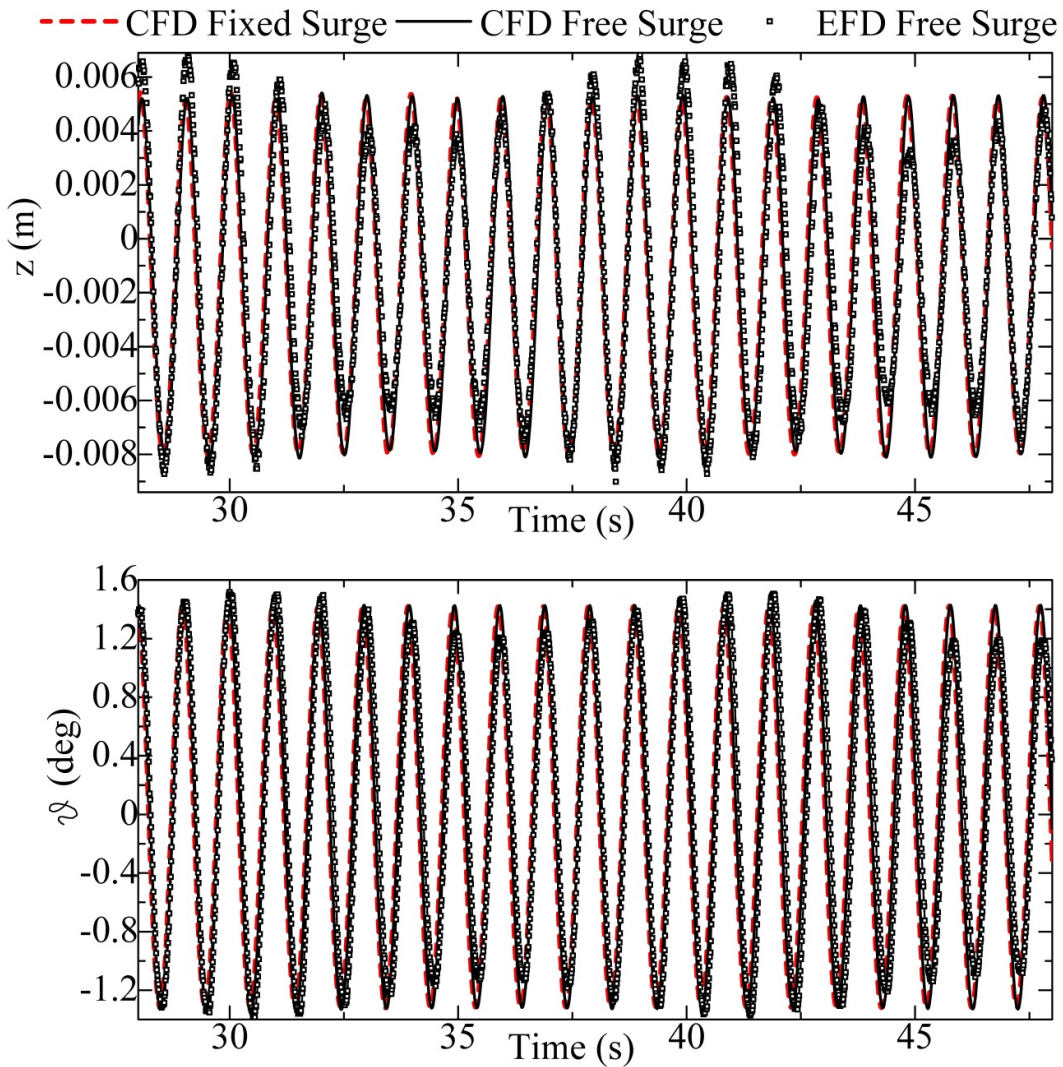


Fig. 6-13 Time history of heave and pitch motion for ballast condition
at $\lambda/L=0.9$

Figure 6-12 to 16-14 show the EFD (free surge) and CFD (fixed and free surge) time history comparison for ballast condition in $\lambda/L = 0.6, 0.9$ and 1.6 at $Fr=0.142$. Based on the nature of Eq. (1), only heave and pitch motion are compared here.

Generally, the comparison among those results shows good agreement. It also reveals

that the surge motion has less influence on heave and pitch motion. And the amplitude of EFD data might have some fluctuation observed because the measured wave amplitude has very small deviations from the incident wave amplitude.

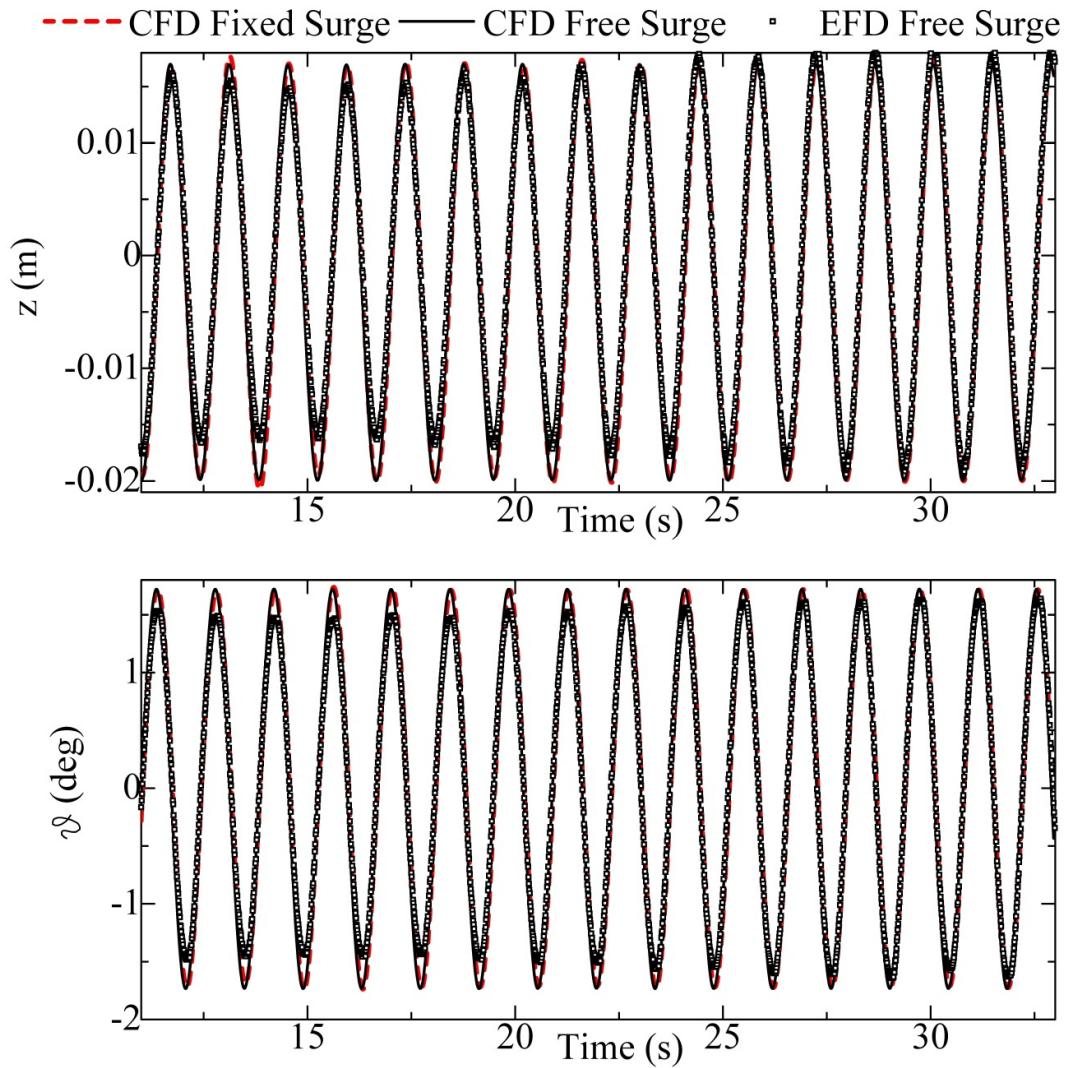


Fig. 6-14 Time history of heave and pitch motion for ballast condition
at $\lambda/L=1.6$

6.3.2 Motion responses and the added resistance

The CFD results in comparison with OU EFD data for ballast condition at $Fr=0.142$ are presented from Figure 6-12 to 15 and the error table is in Table 6-9. The cases labeled “fine” in the figure and table for fixed surge condition use GB_a grid (refer Table 3-2) for $\lambda/L=0.6$ and 0.9, and GB_b grid (refer Table 3-2) for the shortest wave length $\lambda/L=0.3$. Their background is much finer compared with the other cases using G₂ grid.

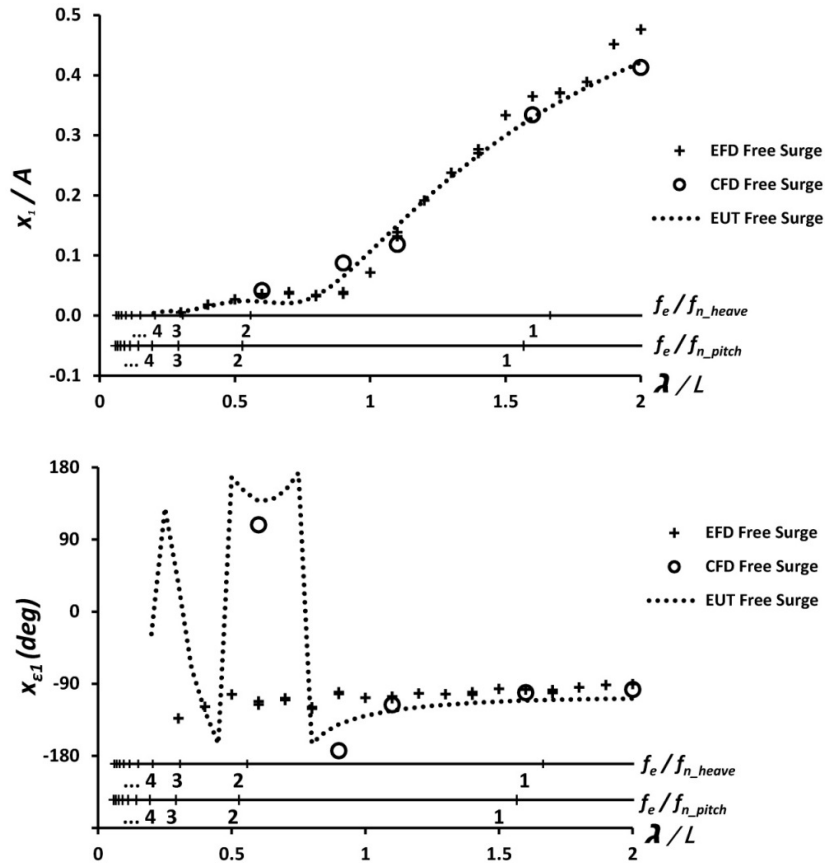


Fig. 6-15 1st harmonic amplitude and phase of surge motion for ballast condition at $Fr=0.142$.

For surge motion, Figure 6-12 shows the 1st amplitude and phase. For the 1st harmonic amplitude x_1/A , basically CFD with free surge condition predicts well. In the longer wave such as $\lambda/L=1.6$ and 2.0, CFD under-predicts the values. CFD and EFD show the same trend: x_1/A decreases as λ/L decreases. In very short waves, x_1/A would be close to zero. However, at $\lambda/L=0.9$ EFD reveal an obvious trough on its trend but CFD over-predicts it with very large error more than 100% D . The average error among all cases is 31% D . By excluding $\lambda/L=0.9$, the average error drops to 10% D . By decreasing λ/L , the phase x_{e1} keeps around -90 deg and decreases as $\lambda/L<1$.

For heave motion, the 1st amplitude, phase and mean values are shown in Figure 6-13. The good agreement is existed between CFD and EFD showing that the 1st harmonic amplitude z_1/A decreases as λ/L decreases. In very short waves, z_1/A would be close to zero. For very long waves, z_1/A would tend to be one, which means the ship vertically moves as the wave amplitude. For free and fixed surge cases, the average error is about 5% D . The absolute error rises as λ/L becomes short. Using the fine grids would reduce the error, especially for the short wave condition (2.75% D in average), but for $\lambda/L=0.9$ the error increases very slightly. For the phase z_{e1} , it shows no phase lag for longer waves $\lambda/L>1$. The ship vertically moves to the maximum when the long wave crest arrives at the mid-ship. And as λ/L decreases z_{e1} increases. It implies the ship moves to maximal heave amplitude much later for shorter waves. For the mean values z_0 , it maintains nearly a constant value around -0.2cm for all cases.

For pitch motion, the 1st amplitude, phase and mean values are shown in Figure 6-14. CFD and EFD agree well for the 1st amplitude θ_1/Ak except for the shorter and longer waves. For $\lambda/L=2.0$, it shows around 9% D error larger than the average error 5~6% D . The very good agreement for $\lambda/L=1.1$ and 1.6: around 1% for fixed surge condition and

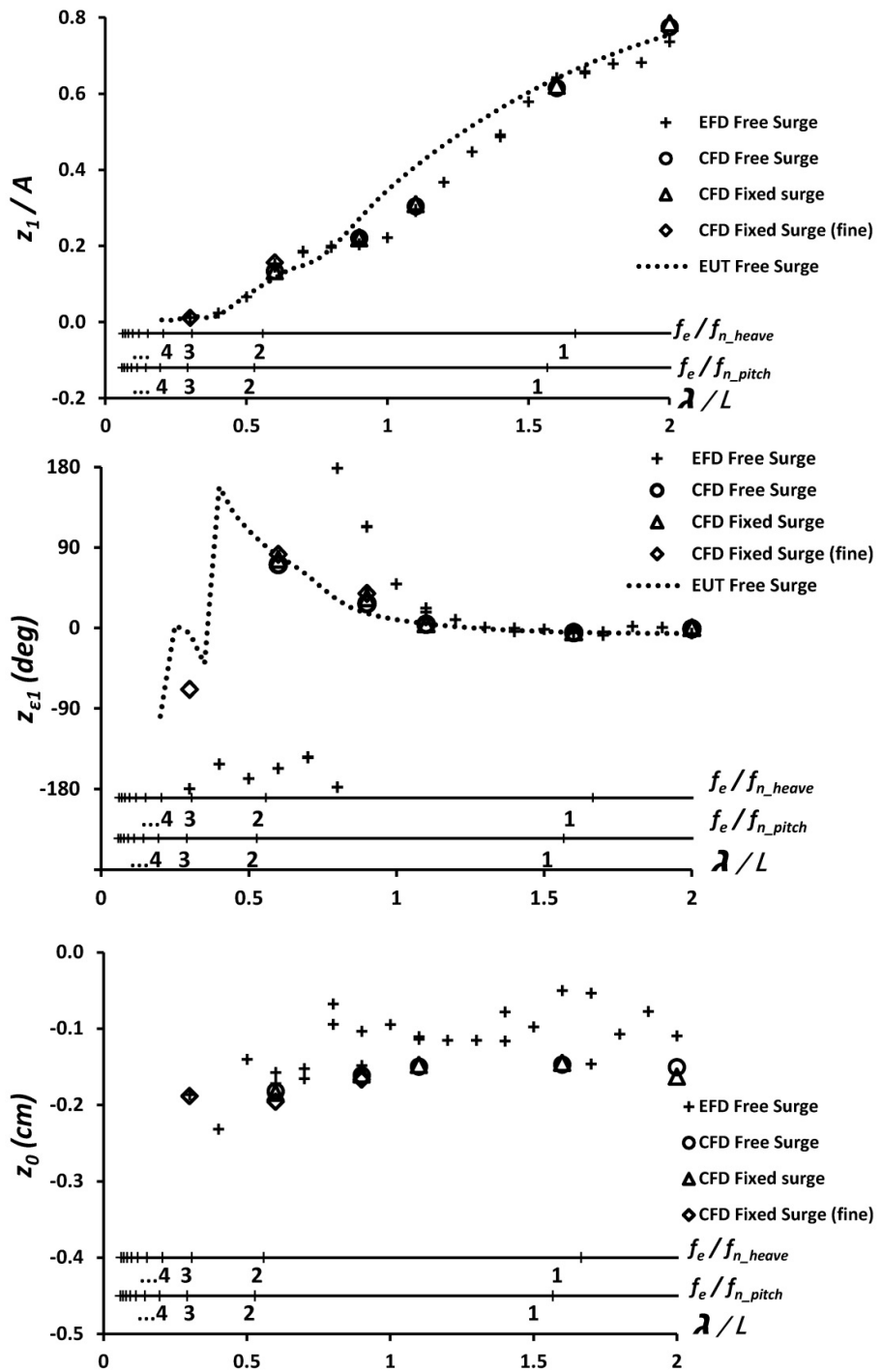


Fig. 6-16 1st harmonic amplitude and phase of heave motion for ballast condition at $Fr=0.142$

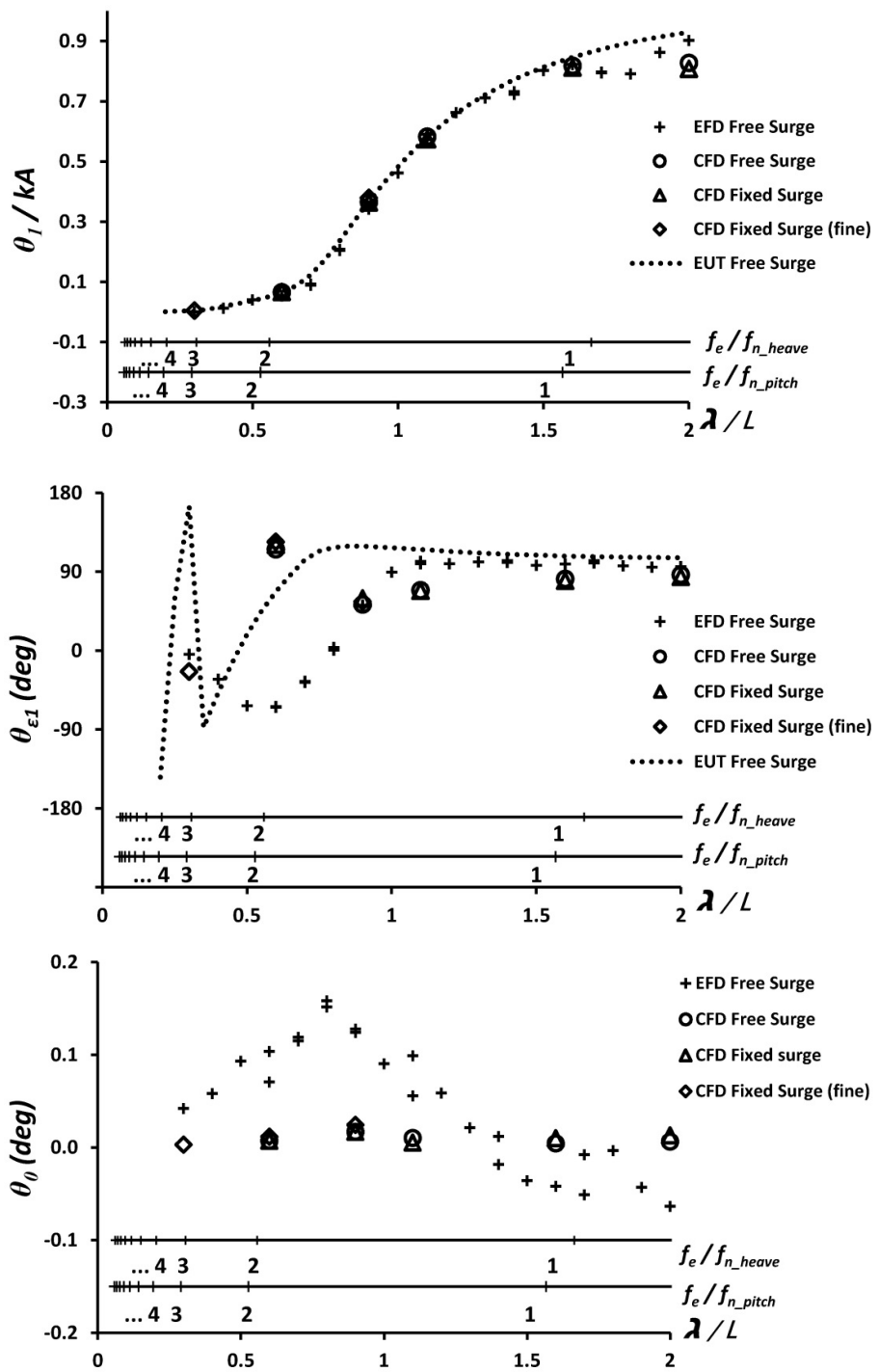


Fig. 6-17 1st harmonic amplitude and phase of pitch motion for ballast condition at $Fr=0.142$.

less than 1% for free surge condition. The error increases as λ/L decreases from 0.9 to 0.3 and the fine grid could not reduce the errors. The maximum error occurs for the shortest wave $\lambda/L=0.3$. CFD value is around 7 times larger than EFD one. However, both are very small values close to zero. For the phase, θ_{e1} drops from 90 deg very slightly as λ/L decreases. For longer waves, the sinkage and trim of the ship would follow the slope of the incident waves. The maximum slope would have 90% phase difference with the maximum amplitude in a cosine wave. For the short waves ($\lambda/L=0.6$ and 0.3), the θ_{e1} increases as λ/L decreases. For mean values, θ_0 also maintains nearly the constant zero value among all cases.

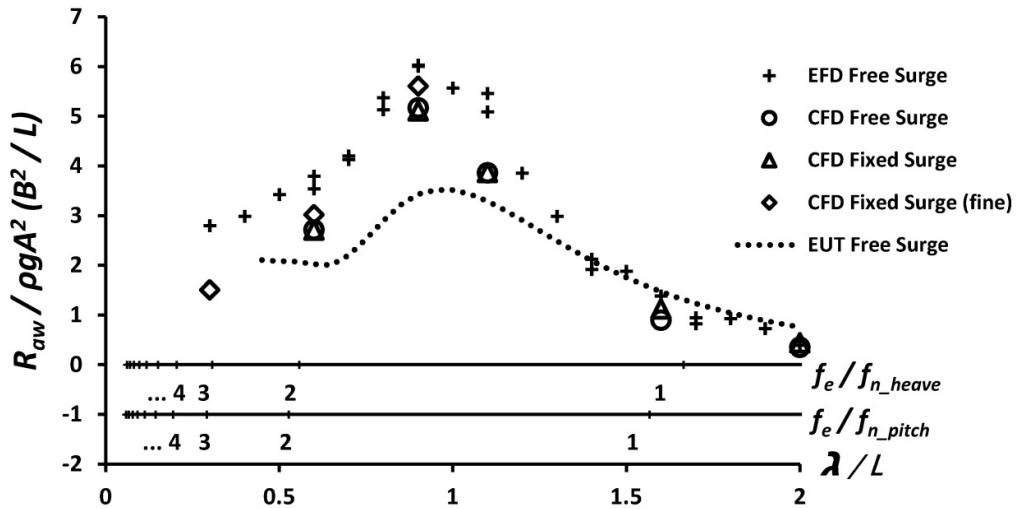


Fig. 6-18 Added resistance at $Fr=0.142$ for ballast condition.

For the added resistance coefficient, as shown in Figure 6-15, CFD and EFD present the peak at $\lambda/L=0.9$. For the all range of wave lengths, CFD predicted the added resistance with 18% D error for fixed and free surge condition. The fine grid improves the prediction error to 12% D in average. For the largest added resistance, i.e. $\lambda/L=0.9$,

the accuracy increase around twice (14~15% vs. 7%). The error also could be improved for short waves, for instance the error of $\lambda/L=0.6$ is reduced from 26% to 18%. However, the error for very short waves such as $\lambda/L=0.3$, it still needs much finer grid to improve the result (current error is 46% D).

Unlike the fully-loaded condition in which the maximum added resistance coincides with the heave natural frequency and the discussion in Chapter 1, the maximum value for ballast condition is still around wave resonance condition $\lambda \sim L$ ($\lambda/L=1.1$) but far away from the heave or pitch natural frequency. Both natural frequencies only correspond to their own larger motion amplitude in longer wave length region.

Table 6-9 Prediction errors for free and fixed surge condition for CFD in ballast condition (EFD source: OU, free surge)

λ/L	x_I/A		z_I/A		θ_I/Ak				C_{aw}		
	Free surge E%D	Fixed surge E%D	Fixed surge (fine) E%D	Free surge E%D	Fixed surge E%D	Fixed surge (fine) E%D	Free surge E%D	Fixed surge E%D	Fixed surge (fine) E%D	Free surge E%D	
0.3			2.20			-768.92				46.12	
0.6	-17.44	10.37	-5.27	10.29	-21.36	-19.34	-18.55	26.09	17.74	25.96	
0.9	-134.92	-7.77	-9.04	-8.07	-5.09	-9.59	-5.60	15.13	6.89	14.12	
1.1	12.27	-5.61		-3.68	1.36		-0.22	26.73		26.82	
1.6	8.42	3.31		4.33	1.32		0.58	18.79		34.99	
2.0	13.28	-6.56		-5.21	10.46		8.24	-13.43		11.09	
$ E $	31.06	5.60	2.75	5.26	6.60	132.98	5.53	16.70	11.79	18.83	

D: OU EFD, free surge.

CHAPTER 7: LOCAL FLOW ANALYSIS

7.1 FORCE DISTRIBUTION ON THE HULL

To investigate the source of the added resistance, in Figure 7-1 to 7-4, the middle column shows the local resistance difference $dX-dX_S$ on the hull surface which is the difference of x-force distribution in waves and calm water. By assuming the dynamic wetted area in waves is close to the steady area in calm water, $\overline{(dX - dX_S) dA_W} \sim \bar{X} - \bar{X}_S = R_{AW}$. The figures are in ship-fixed coordinate for the four quarter periods on each row from (a) to (d), $t/Te = 0, 0.25, 0.5$ and 0.75 for fixed surge simulation at $\lambda/L = 0.18, 0.6, 1.1, 1.6$. The figures are along with the one-period time history of resistance (C_T), heave (x) and pitch motions (θ) on the left column, and the comparison of free surface elevation on the hull and entire ship movement in waves and calm water on right column.

As shown in Figure 7-1, the motions are very small for the short waves $\lambda/L = 0.18$ and 0.6 , i.e. the wave radiation force is not dominant. The $dX-dX_S$ on most of the parts of the ship is negligibly small and the large value is only observed for the small area right above the bow which is induced by bow wave diffraction. For larger wave length condition, the strong force distribution above the bow is not only induced by wave diffraction but also by large hydrodynamic force due to the large heave and pitch motion. From the figures, a strong correlation appears between the $dX-dX_S$ above the bow and the bow motion. The maximum/minimum of $dX-dX_S$ above the bow is observed at the time of bow down/up, especially for $\lambda/L = 1.1$ and 1.6 . Since among different wave length condition, the maximum bow displacement is at $\lambda/L = 1.1$, see Figure 7-3, the $dX-dX_S$ above the bow is significantly large compared to the other wave lengths. Besides

the motions, the difference of the free surface location on the hull between in calm water and waves reveals the influences on $dX \cdot dX_S$. The more difference results in larger change of wetted area in wave and introduces nonlinearity in the added resistance. As observed in the Figures, the difference mainly is around the bow. It might interact with the bow motion, i.e. the relative bow motion. Since the free surface difference is very large for $\lambda/L=1.1$, it is expected to have the maximum nonlinearities and higher order effects. Figure 6-8 also confirms the largest second harmonic amplitude X_2 for $\lambda/L=1.1$.

Based on the time history of Figure 7-1 to 7-4, Fourier analysis on $dX \cdot dX_S$ could be performed as Figure 7-5 showing each component of the $dX \cdot dX_S$ on the ship hull for fixed surge simulation at $\lambda/L=0.18, 0.6, 1.1, 1.6$. The figures are plotted for the mean value $dX_0 \cdot dX_S$ (i.e. the “local” added resistance), and first and second harmonic amplitude dX_1 and dX_2 . For all wave length condition, the mean value distribution shows that the added resistance is induced by the high pressure region on the upper bow. The size of the high pressure region correlates with the bow relative motion (see Figure 6-7) which increases to its maximum at $\lambda/L=1.1$ close to the location of the peak of the added resistance, as shown in Figure 6-9. The first harmonic dX_1 distribution shows large values near the bow for all wave length conditions as well suggesting that the resistance forces/x-forces/surge forces oscillates with larger amplitude near the bow. The dX_1 value in the mid-ship and at stern is nearly zero such that the resistance force oscillations are small for most of the body except near the bow. The plotted second harmonic dX_2 distribution shows existence of nonlinearity and higher order effects close to the bow induced by large change of the wetted area. The maximum amplitude of the second harmonic is about 30% of the maximum first harmonic amplitude.

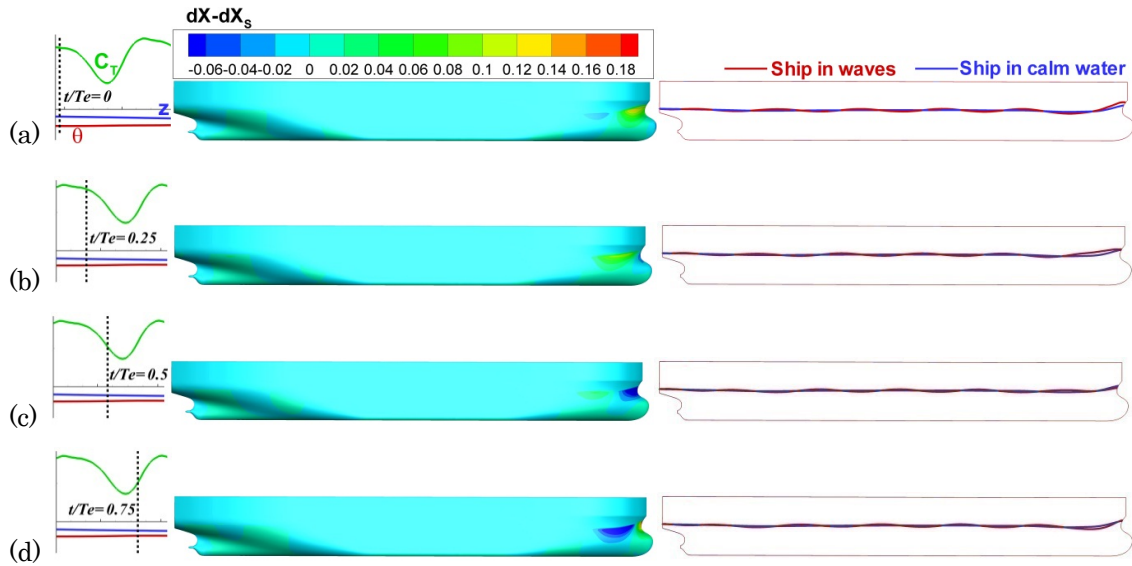


Fig. 7-1 Local resistance difference and ship motions ($\lambda/L=0.1810$, fixed surge).

(a) $t/T_e = 0$; (b) $t/T_e = 0.25$; (c) $t/T_e = 0.5$; (d) $t/T_e = 0.75$.

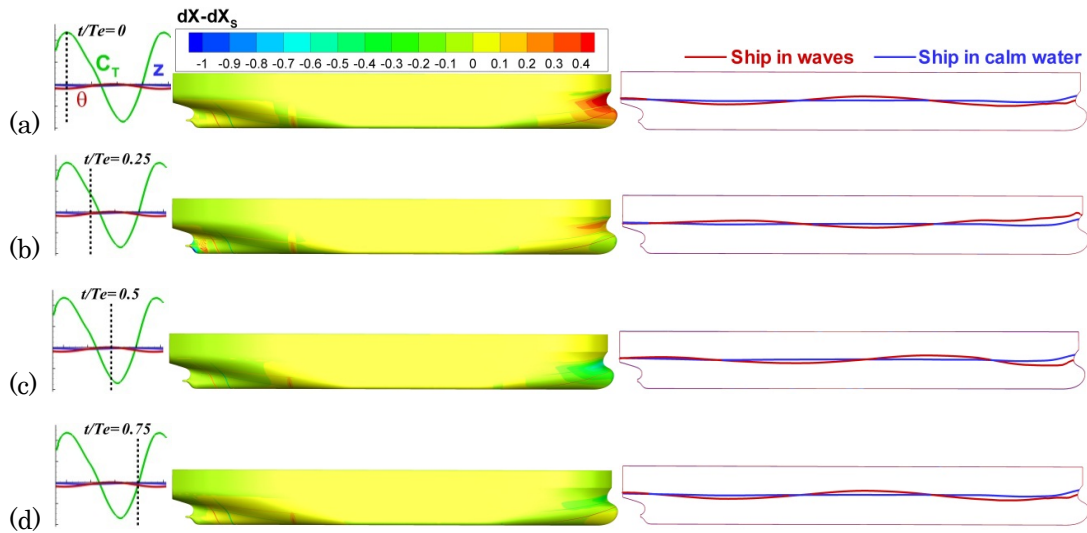


Fig. 7-2 Local resistance difference and ship motions ($\lambda/L=0.6$, fixed surge).

(a) $t/T_e = 0$; (b) $t/T_e = 0.25$; (c) $t/T_e = 0.5$; (d) $t/T_e = 0.75$.

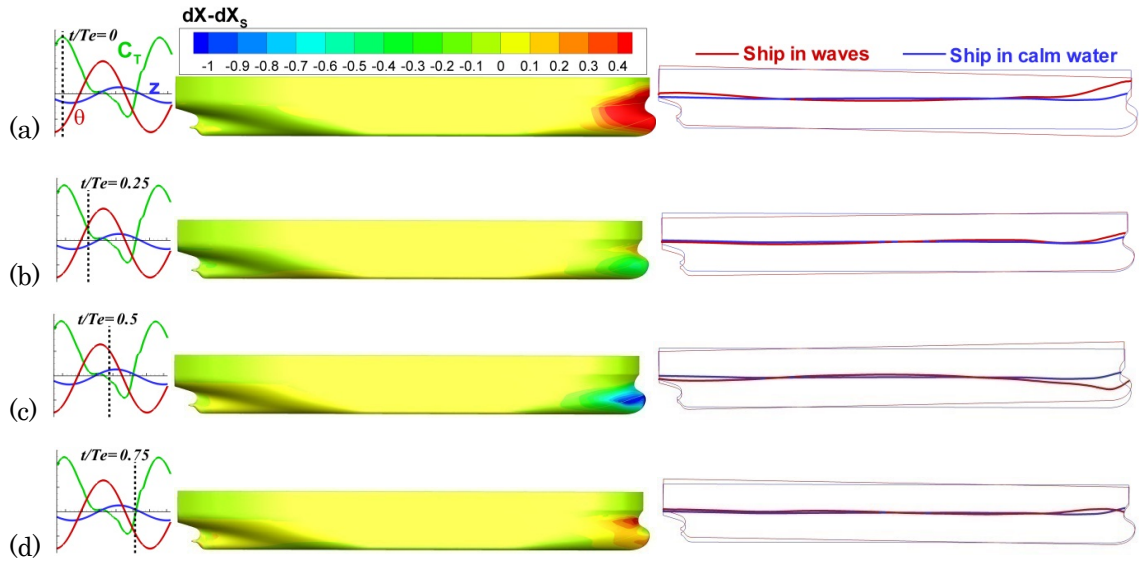


Fig. 7-3 Local resistance difference and ship motions ($\lambda/L=1.1$, fixed surge).

(a) $t/T_e = 0$; (b) $t/T_e = 0.25$; (c) $t/T_e = 0.5$; (d) $t/T_e = 0.75$.

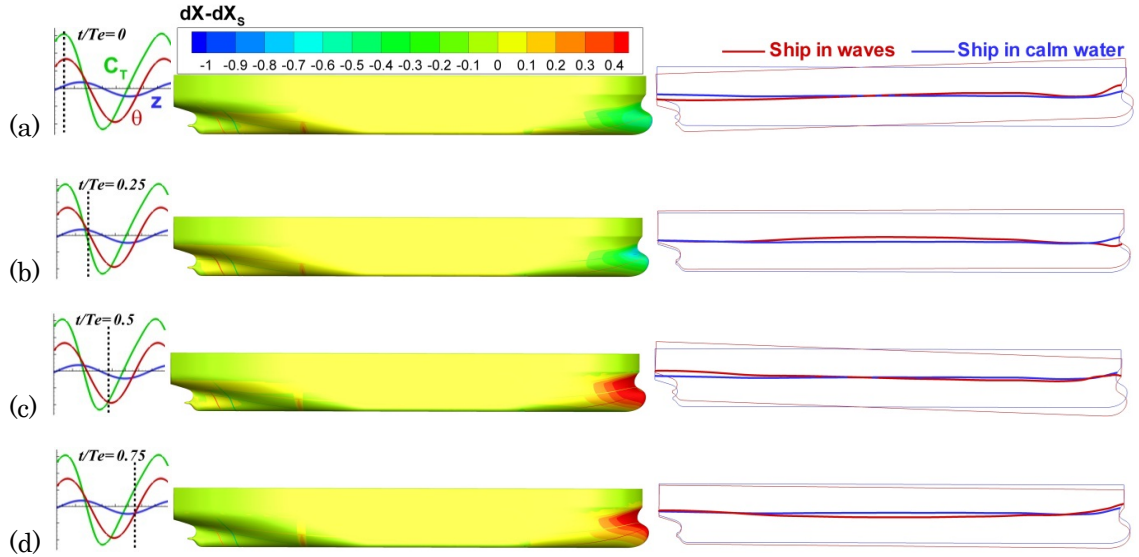


Fig. 7-4 Local resistance difference and ship motions ($\lambda/L=1.6$, fixed surge).

(a) $t/T_e = 0$; (b) $t/T_e = 0.25$; (c) $t/T_e = 0.5$; (d) $t/T_e = 0.75$.

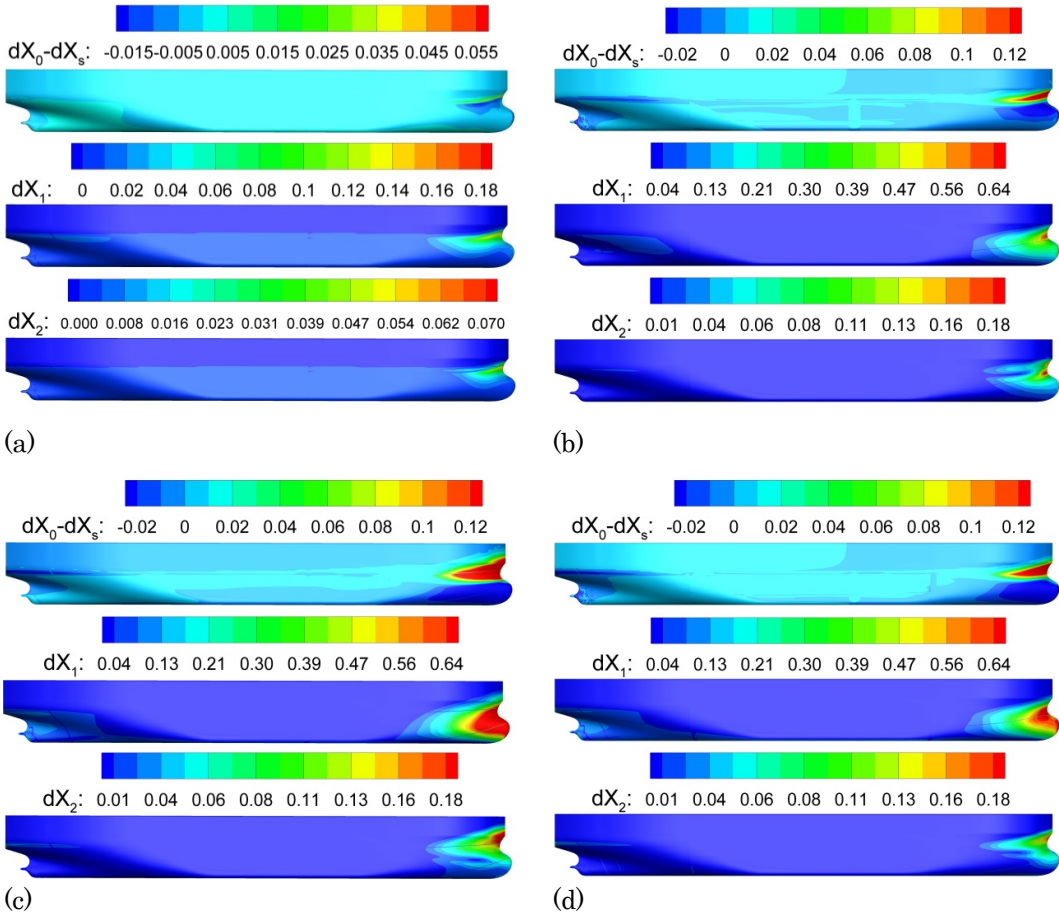


Fig. 7-5 The mean value, 1st and 2nd harmonic amplitude of local resistance difference for fixed surge: (a) $\lambda/L=0.1810$; (b) $\lambda/L=0.6$; (c) $\lambda/L=1.1$; (d) $\lambda/L=1.6$.

7.2 UNSTEADY WAVE PATTERN ANALYSIS

The wave pattern in one-quarter periods is shown in Figure 7-6 for four different wave length conditions of $\lambda/L=0.18, 0.6, 1.1, 1.6$. The free surface is colored with elevation for the four quarter periods for all of the cases. The wave crest of undisturbed incident wave/cosine wave is at forward perpendicular of ship bow when $t/T_e = 0$. For $\lambda/L=0.18$, the wave amplitude is smaller to keep the wave in linear zone ($A/L=0.002719$). For the other cases, $A/L=0.009375$. All cases show very similar wave pattern. For all

cases the transverse waves and Kelvin envelope are observed. Two distinct scars on the free surface, originating from the bow and aft of the ship show the Kelvin envelope.

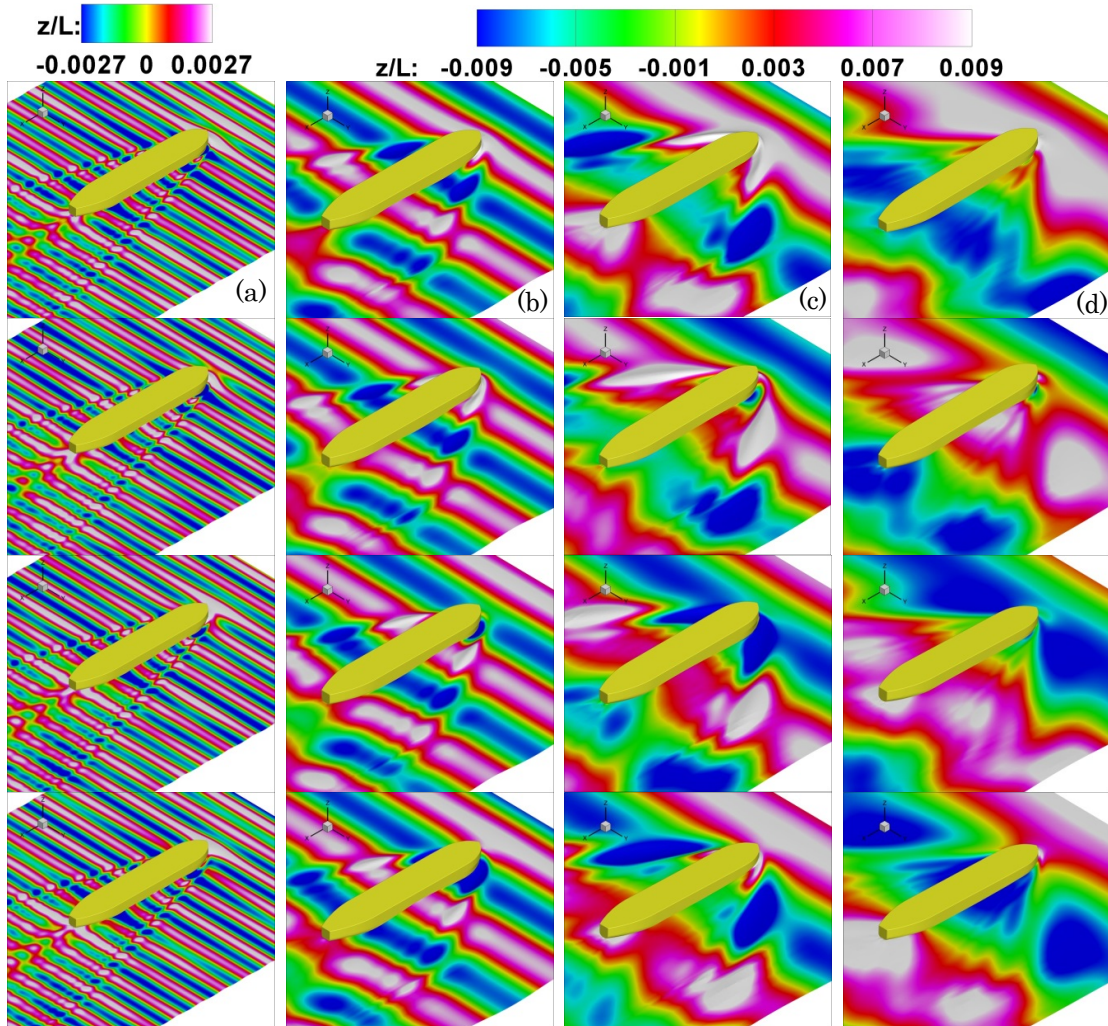


Fig. 7-6 Wave pattern for the four quarter encounter periods $t/T_e = 0, 0.25, 0.5, 0.75$:

(a) $\lambda/L=0.1810$; (b) $\lambda/L=0.6$; (c) $\lambda/L=1.1$; (d) $\lambda/L=1.6$.

In order to evaluate the contribution of free surface deformation to the added resistance, the unsteady wave pattern for $\lambda/L=0.18, 0.6, 1.1, 1.6$ is calculated by subtracting the incident wave and calm water free surface elevation from the predicted

free surface deformation in head waves. The computed unsteady wave pattern for $\lambda/L=0.18, 0.6, 1.1, 1.6$ is plotted at four instants in the encounter period ($t/T_e = 0, 0.25, 0.5$ and 0.75), as shown in Figure 7-7. The unsteady wave pattern shows the diffraction and radiation waves initiate from the fore-body shoulder and transom corner with a phase lag. The size of the unsteady wave increases by increasing wave length and then drops for $\lambda/L > 1.1$. Thus the maximum energy loss of the ship (i.e. the peak of the added resistance) is expected to be for λ/L near 1.1. The generated unsteady waves diverged from the model at 22° with respect to the center-plane for very short waves. The angle increases to 45° for $\lambda/L=1.1$. Since for all wave length condition, the group velocity of waves is higher than the ship speed (Hamaoka parameter $U\omega/g$ is higher than $\frac{1}{4}$), there is no wave generated from the ship at upstream due to the ship forward speed.

The mean value, the first harmonic amplitude and phase, and the second harmonic amplitude and phase for the unsteady wave pattern for $\lambda/L=0.18, 0.6, 1.1, 1.6$ are shown in Figure 7-8 to 7-11. The mean value is the difference between the zeroth-harmonic amplitude and the calm water free surface elevation. For all wave length, this difference is nearly zero for most parts of the near- and far-field region meaning that zeroth-harmonic amplitude of wave field displays the typical wave pattern characteristics of a hull form advancing in calm water including diverging and transverse waves. In near-field region close to the fore-body shoulder, the amplitude of the diverging wave pattern in waves is higher than that in calm water inducing non-zero mean value. This non-zero mean value is largest for $\lambda/L=1.1$ and might have a non-negligible contribution to the added resistance force. The first harmonic amplitude of unsteady wave pattern induced by radiated and diffracted waves shows that the unsteady wave initiates at the fore-body shoulder and transom corner. It also shows no

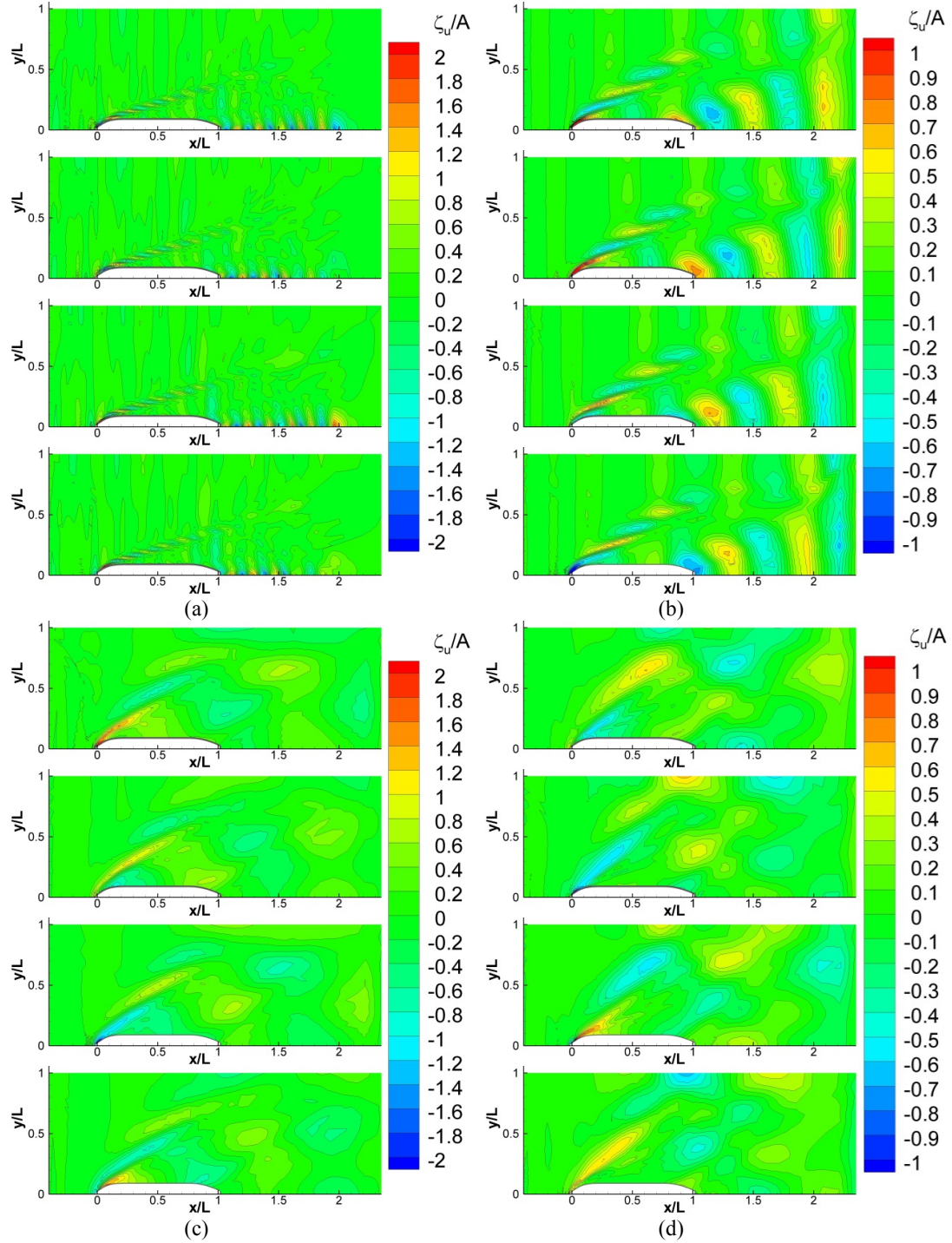


Fig. 7-7 Unsteady wave component ζ_u ($=\zeta - \zeta_i - \zeta_s$; ζ unsteady free surface elevation; ζ_i incident wave elevation; ζ_s steady free surface elevation in calm water) of the free surface elevation for four quarter encounter periods $t/T_e = 0, 0.25, 0.5, 0.75$:

(a) $\lambda/L=0.1810$; (b) $\lambda/L=0.6$; (c) $\lambda/L=1.1$; (d) $\lambda/L=1.6$.

wave generated from the ship at upstream due to the ship forward speed. The positive peak of unsteady wave is located near the fore-body shoulder and bow for $\lambda/L \leq 1.1$ with maximum value for $\lambda/L=1.1$ while negative peak is located near the bow for $\lambda/L>1.1$. This suggests that maximum dynamical rise of the water surface near the bow occurs for λ/L close to 1.1, providing the maximum bow relative motion and largest added resistance. The amplitude of second harmonic is near zero for far-field region. In near-field region close to the fore-body shoulder, the second harmonic unsteady wave exists which might be originated from the wave breaking at fore-body shoulder or close to the bulbous bow. Kashiwagi (2013) revealed the interesting phenomena of the unsteady wave pattern corresponding to our conclusion here. The fore-front part of the unsteady wave pattern shows non-linearity due to larger ship motion. Also, it consists of various wave components, such as short-wavelength components which should be considered in the linear waves to predict the wave profile and the added resistance.

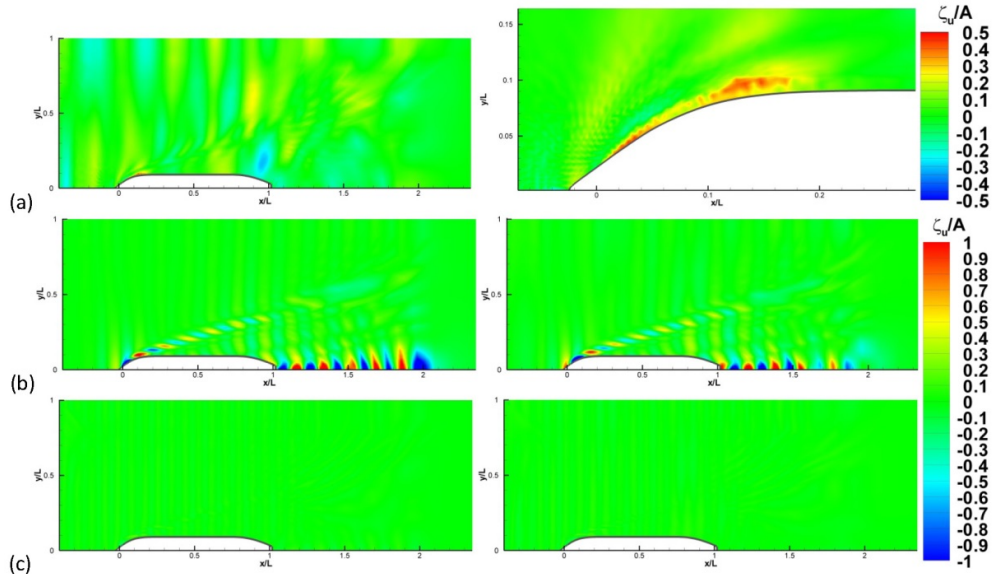


Fig. 7-8 Fourier analysis of ζ_u for $\lambda/L=0.1810$, $A/L=0.002719$ and fixed surge.
 (a) Mean value. (b) 1st harmonic amplitude of Cosine (left) and Sine (right) component. (c) 2nd harmonic amplitude of Cosine (left) and Sine (right)

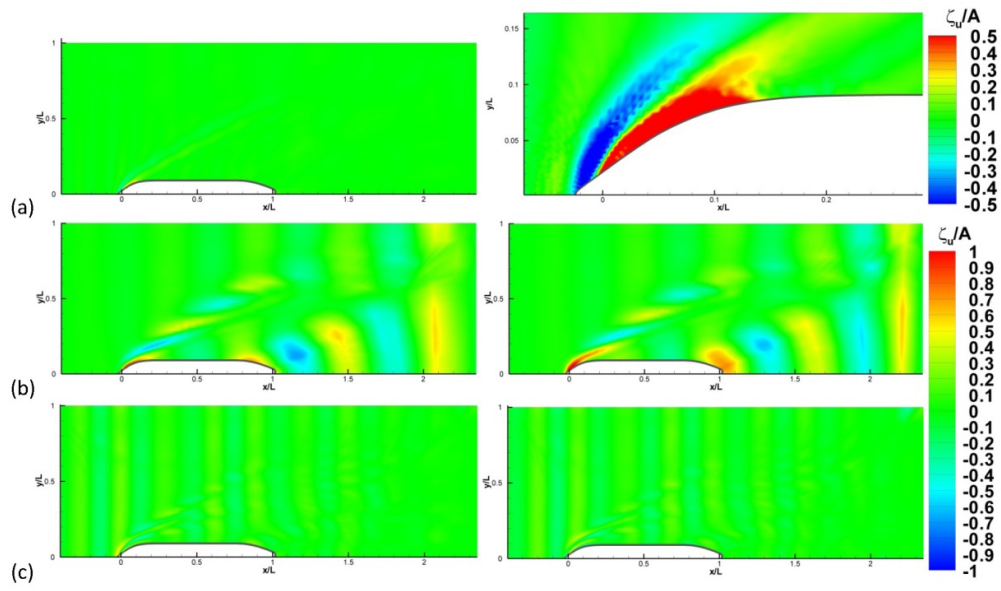


Fig. 7-9 Fourier analysis of ζ_u for $\lambda/L=0.6$, $A/L=0.009375$ and fixed surge.

(a) Mean value. (b) 1st harmonic amplitude of Cosine (left) and Sine (right) component. (c) 2nd harmonic amplitude of Cosine (left) and Sine (right)

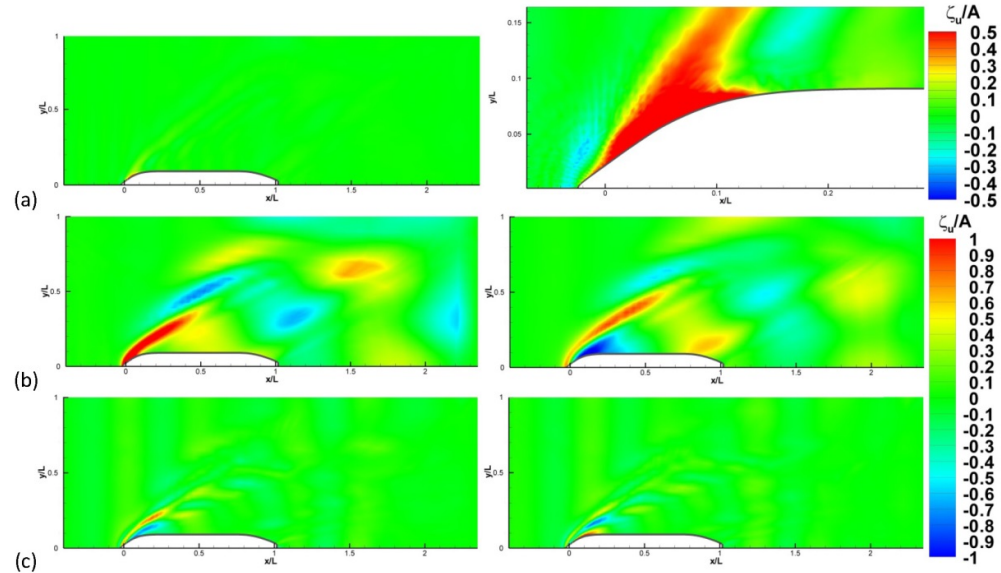


Fig. 7-10 Fourier analysis of ζ_u for $\lambda/L=1.1$, $A/L=0.009375$ and fixed surge.

(a) Mean value. (b) 1st harmonic amplitude of Cosine (left) and Sine (right) component. (c) 2nd harmonic amplitude of Cosine (left) and Sine (right).

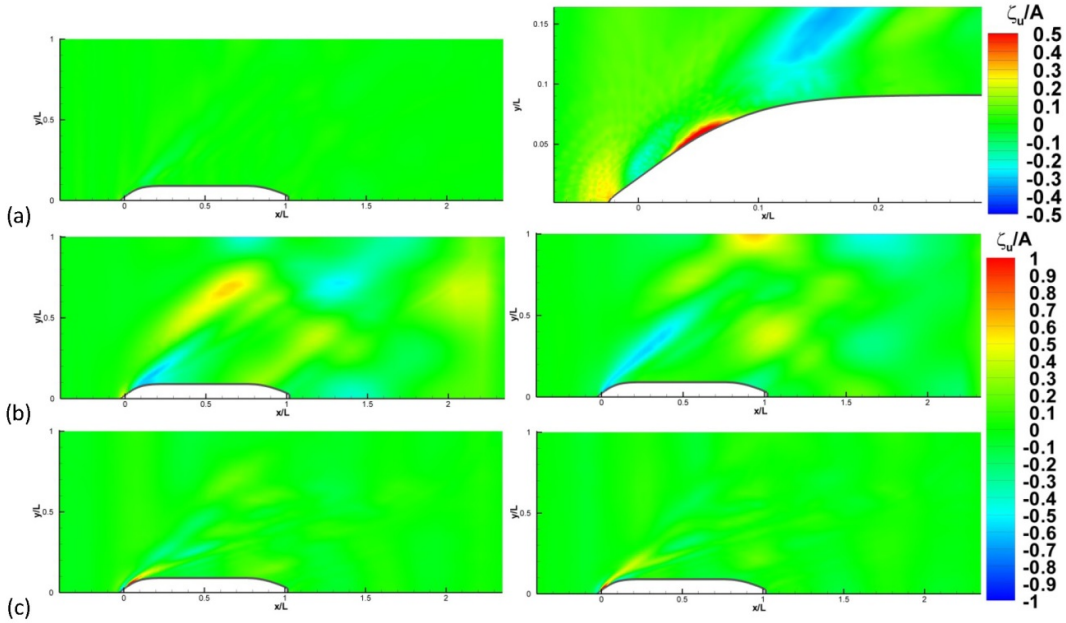


Fig. 7-11 Fourier analysis of ζ_u for $\lambda/L=1.6$, $A/L=0.009375$ and fixed surge.

(a) Mean value. (b) 1st harmonic amplitude of Cosine (left) and Sine (right) component. (c) 2nd harmonic amplitude of Cosine (left) and Sine (right).

7.3 NOMINAL WAKE ANALYSIS

7.3.1 Boundary layer development

Figure 7-12 shows the developed boundary layer around the ship hull represented by constant x value slices colored with axial velocity limited to $U=0.9$ for the four quarter periods for $\lambda/L=1.1$ condition. As the wave crest passes the bow at $t/T_e=0$, the bow goes down into the water and the generated vortices near the sharp edges under the ship are transported downstream. This causes very thick boundary layer after $x/L=0.8$ where the hull shape is designed to accommodate the rudder and shaft. At $t/T_e=0.25$ and 0.75

when the wave trough is located as the aft, the generated vortices at the location of rudder and shaft touch the free surface providing very thick wake field compared to that for $t/T_e=0$ and 0.5. This would cause significant change in propeller load and performance in waves.

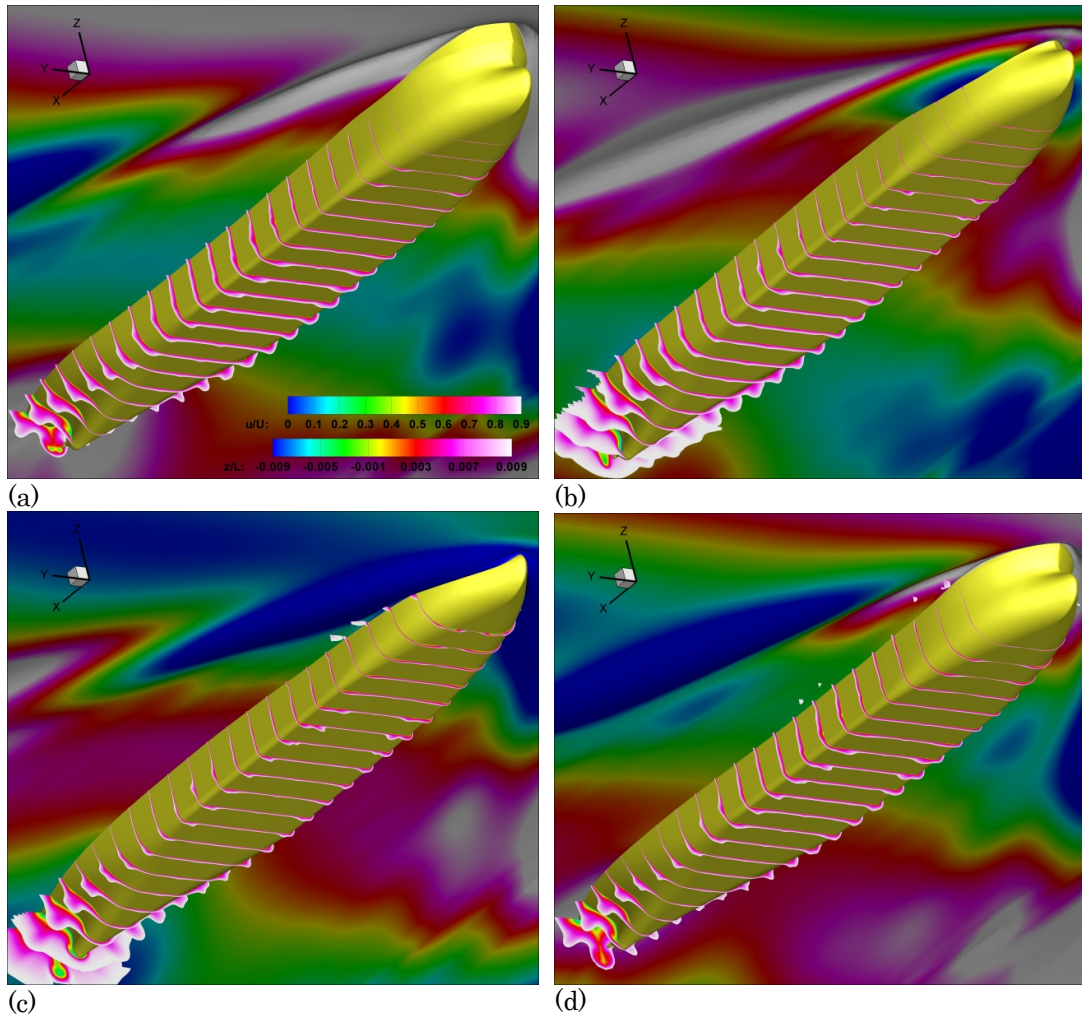


Fig. 7-12 Boundary layer represented by slices colored with axial velocity below $u/U=0.9$ for the four quarter encounter periods for $\lambda/L=1.1$, $A/L=0.009375$ and fixed surge. (a) $t/T_e = 0.01$; (b) $t/T_e = 0.277$; (c) $t/T_e = 0.455$; (d) $t/T_e = 0.813$.

Figure 7-13 shows the Q-criterion q , defined as the following, equal to 400

$$q = -\frac{1}{2} \left[\left(\frac{\partial u}{\partial x} \right)^2 + \left(\frac{\partial v}{\partial y} \right)^2 + \left(\frac{\partial w}{\partial z} \right)^2 \right] - \left[\frac{\partial u}{\partial y} \frac{\partial v}{\partial x} + \frac{\partial u}{\partial z} \frac{\partial w}{\partial x} + \frac{\partial v}{\partial z} \frac{\partial w}{\partial y} \right] \quad (36)$$

The axial velocity is the contour color on the iso-surface of $q=400$. The two sources of vortex can be observed clearly. The figure presents in four quarter period. The bilge vortex is developed on the hull body and shedding into downstream and propeller plane. It would move and develop relatively to the ship motion. And the other one is formed around the shaft/stern bulb. The vortex is induced by the vertical motion of the stern. Both might interact. More detail is discussed in the next section.

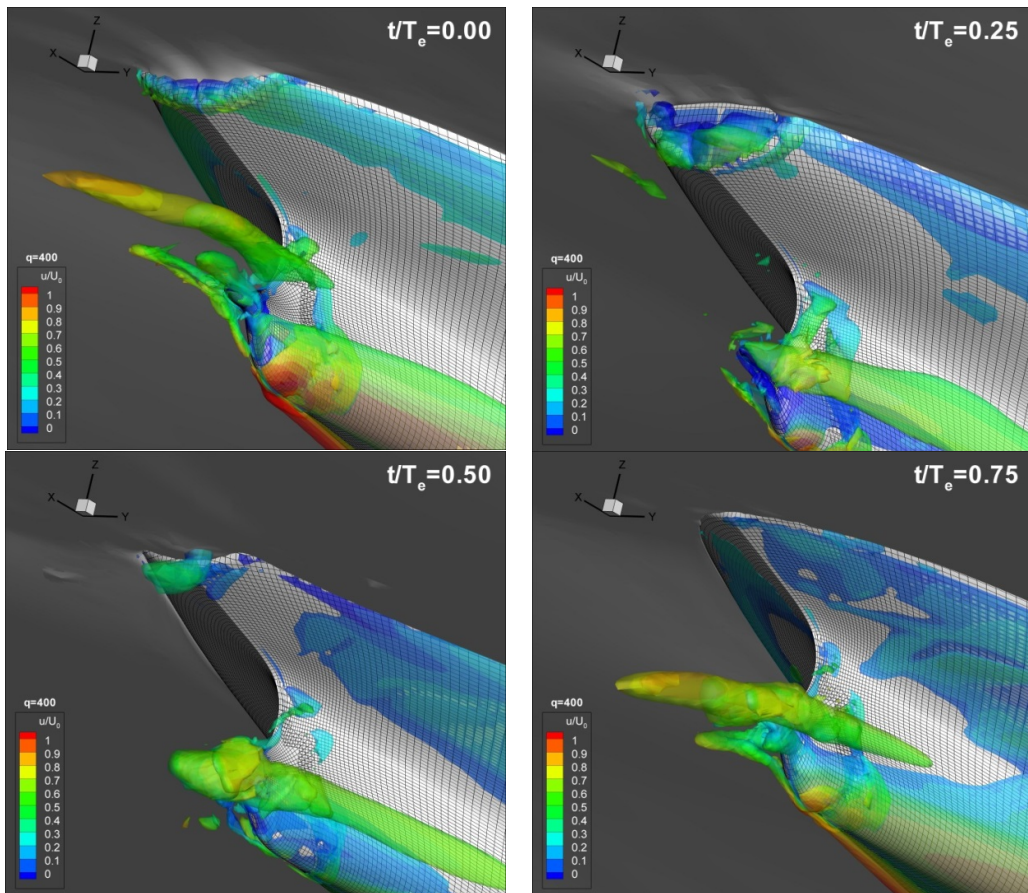


Fig. 7-13 Vortex behavior in stern flow: Q-criterion $q=400$ with axial velocity u/U_0 contour for the four quarter encounter periods for $\lambda/L=1.1$.

7.3.2 Propeller plane in tank fixed coordinate

The CFD axial velocity contours at the stern of the ship ($x/L=0.98$) are plotted in Figure 7-14, 7-15 and 7-16 for $\lambda/L=0.6, 1.1, 1.6$ for fully-loaded condition and compared with the PIV measurement (Hayashi, 2012). And Figure 7-17, 7-18 and 7-19 for $\lambda/L=0.6, 0.9, 1.5/1.6$ are for ballast condition (PIV: Okawa, 2013).

The wake field is more complex than in calm water as the wave changes the shape of the wake field over the encounter period. For all wave length conditions, the wake fields are compressed by higher velocity from outer flow in both y and z directions when the aft is located on the wave crest and then they are expanded in wave trough. The bilge vortex appears as a pair of counter-rotating vortices (counter-clockwise in starboard; clockwise in port side) locating in the middle layer of wake $u/U=0.4\sim0.7$. Following the stern moves down or up, the bilge vortex is observed above or below the shaft and the boundary layer grows thicker around the area. The vertical motion of ship stern induces large low speed area in the wake field around the propeller disk. Another pair of counter-rotating vortices (clockwise in starboard; counter-clockwise in portside) forms inside this area which is inner wake field with $u/U<0.2$. Especially, while the stern moves up, the low speed area extends deeply. It might be deeper than one propeller radius for longer waves. These four vortices show up together clearly in the middle of the stern upward movement, i.e. the bilge vortex is above the shaft and the vortex in the low speed area is under the shaft. The CFD simulation predicts very well the wake pattern and generated vortices around the propeller shaft for all wave length conditions. Note that the CFD wake fields are not plotted for exact same time of EFD as the CFD field solution was saved for limited instants.

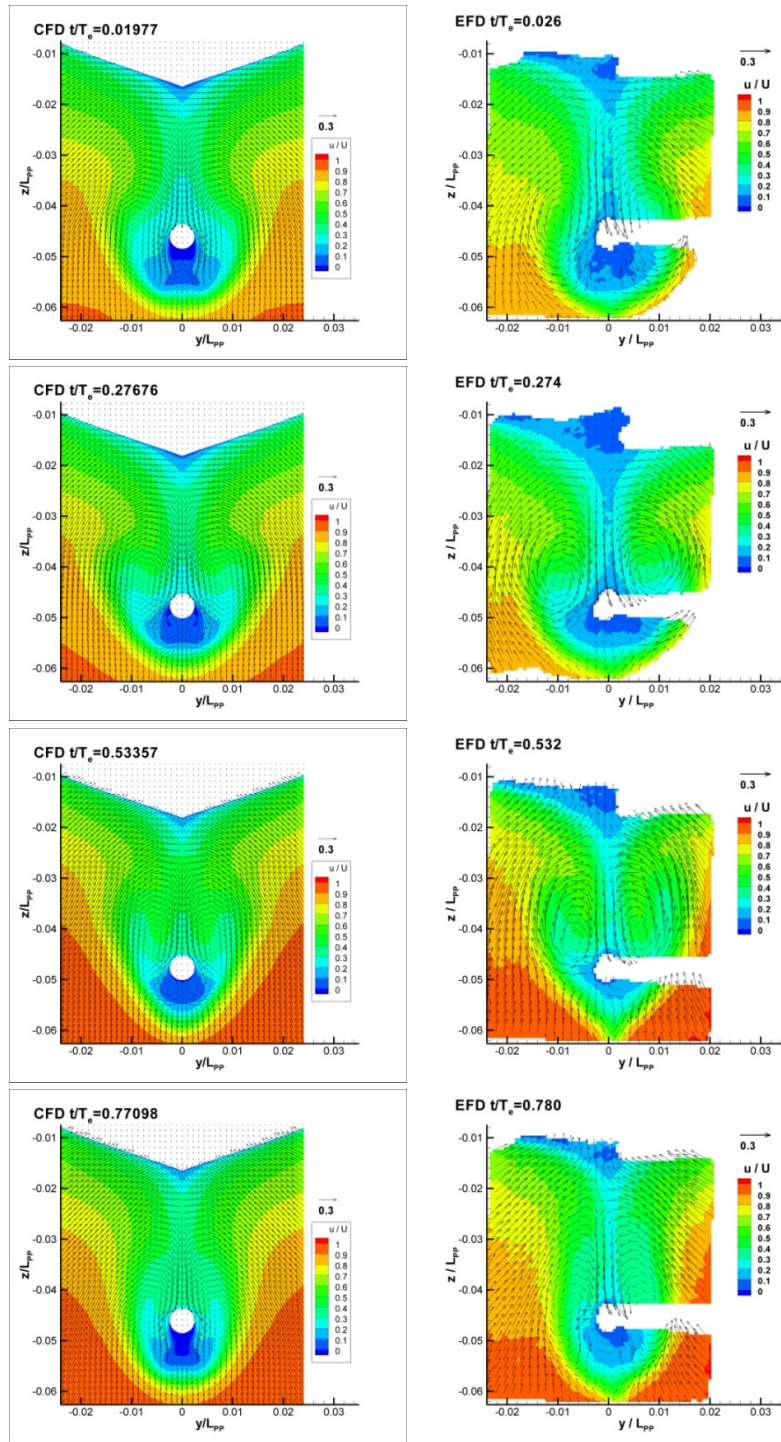


Fig. 7-14 The comparison between CFD (fixed surge) and PIV (free surge): axial velocity contours and velocity vector at propeller plane ($x/L=0.98$) for the four quarter encounter periods for $\lambda/L=0.6$, $A/L=0.009375$, fully-loaded condition.

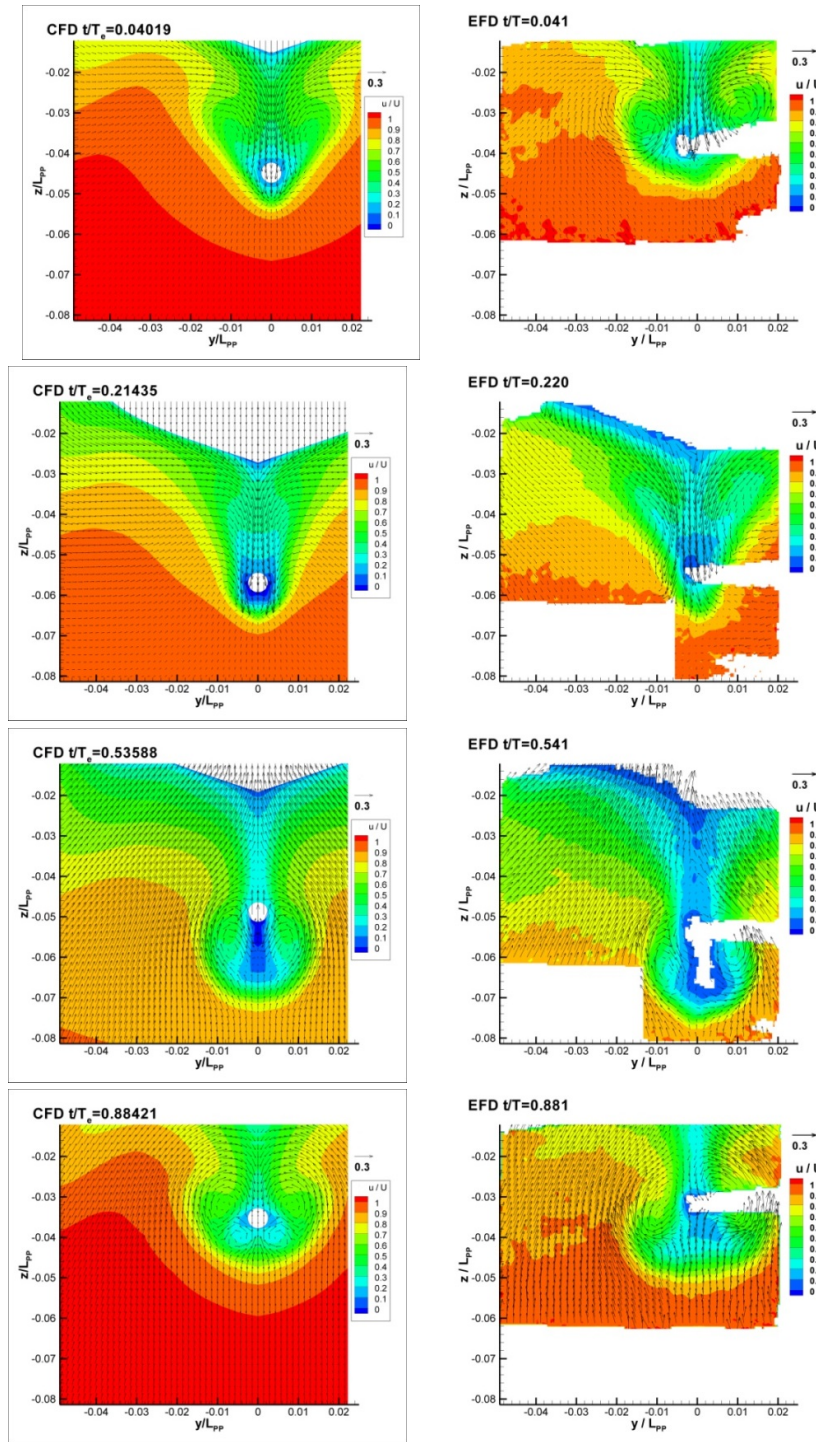


Fig. 7-15 The comparison between CFD (fixed surge) and PIV (free surge): axial velocity contours and velocity vector at propeller plane ($x/L=0.98$) for the four quarter encounter periods for $\lambda/L=1.1$, $A/L=0.009375$, fully-loaded condition.

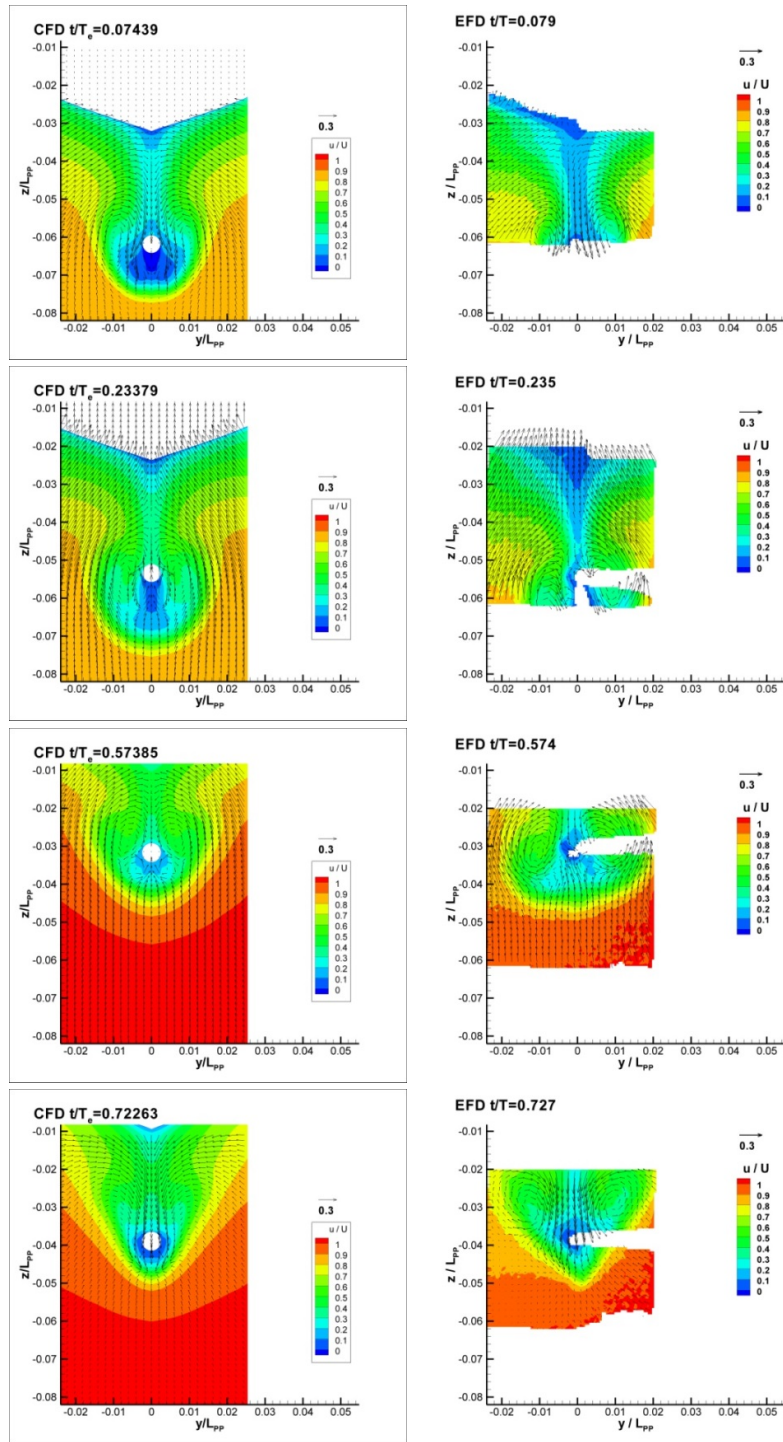


Fig. 7-16 The comparison between CFD (fixed surge) and PIV (free surge): axial velocity contours and velocity vector at propeller plane ($x/L=0.98$) for the four quarter encounter periods for $\lambda/L=1.6$, $A/L=0.009375$, fully-loaded condition.

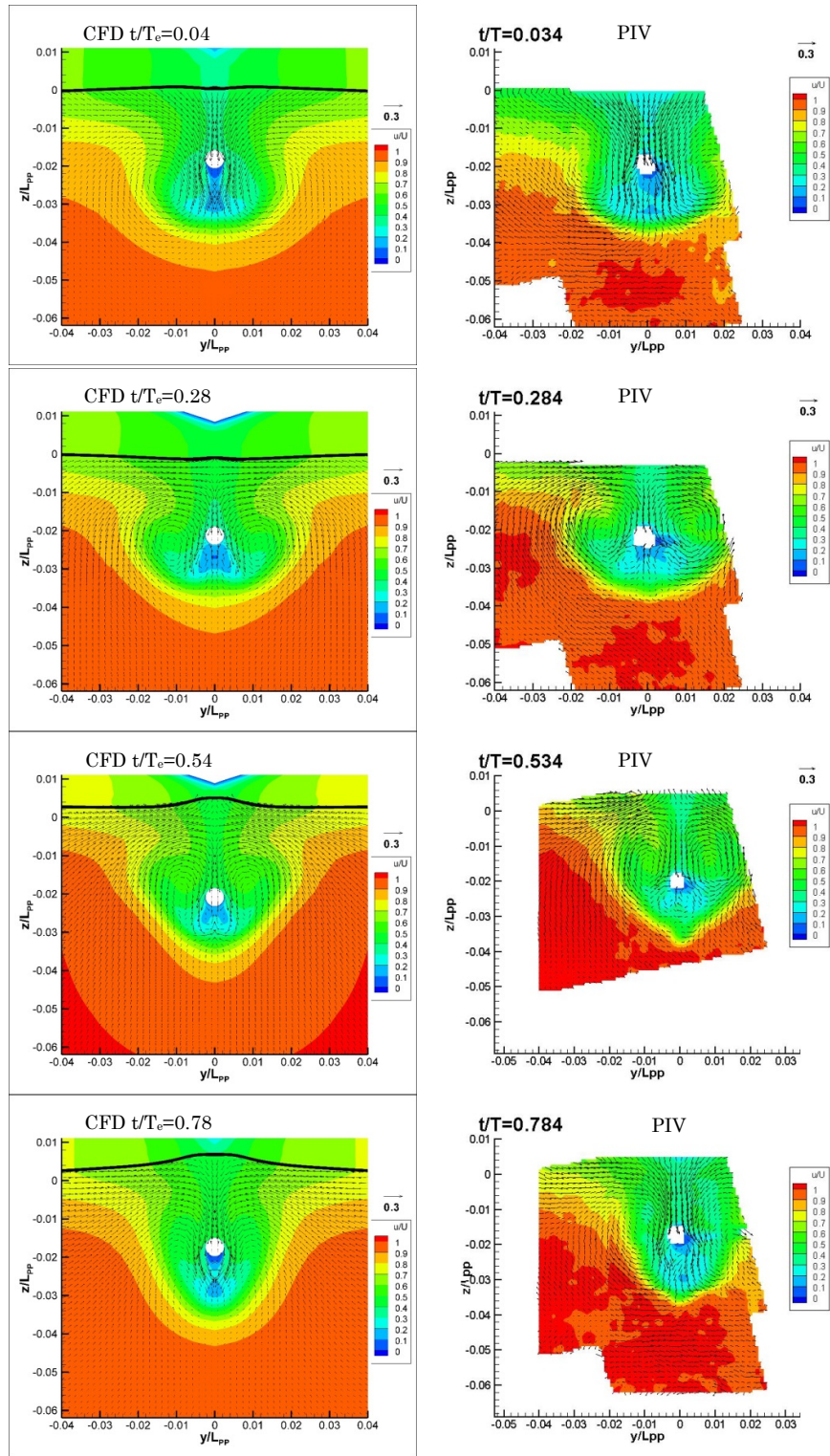


Fig. 7-17 The comparison between CFD (fixed surge) and PIV (free surge)
for $\lambda/L=0.6$, $A/L=0.009375$, ballast condition.

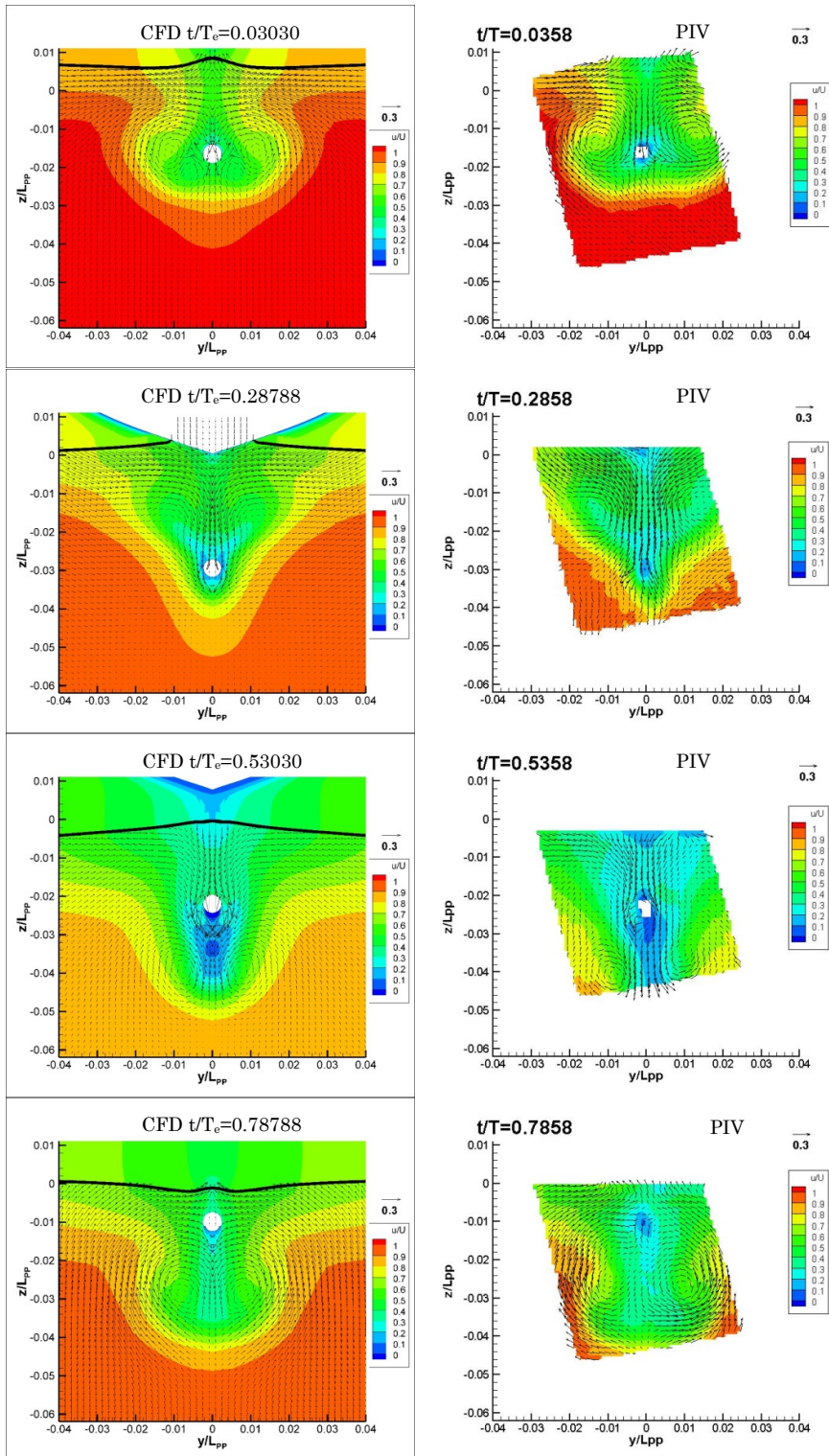


Fig. 7-18 The comparison between CFD (fixed surge) and PIV (free surge) for $\lambda/L=0.9$, $A/L=0.009375$, ballast condition.

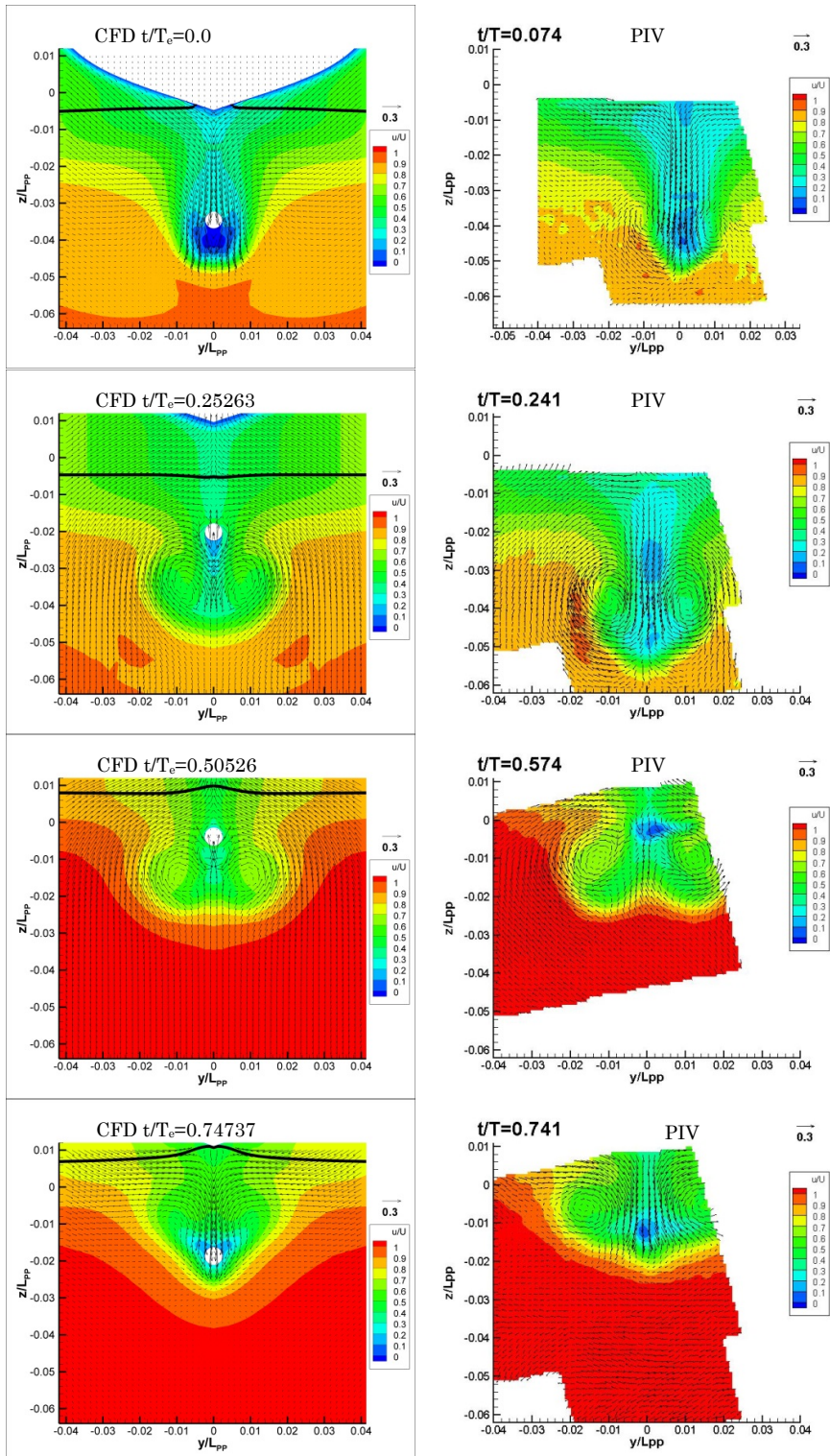


Fig. 7-19 The comparison between CFD ($\lambda/L=1.6$, fixed surge) and PIV ($\lambda/L=1.5$, free surge) for ballast condition.

7.3.3 Propeller plane in ship fixed coordinate

a. Vortex behavior in nominal wake

To understand the vortex behavior of the nominal wake on the propeller plane in waves, Figure 7-20 shows the contour flooding for vorticity $\bar{\omega}_x$, contour lines for axial velocity u/U_0 , and horizontal and vertical velocity vectors $(v/U_0, w/U_0)$ in one encounter period for $\lambda/L=1.1$ in fully loaded condition. $t/T_e=0.0$ is for the incident wave crest at bow. Two sources of vortices appear as mentioned: bilge vortex and the vortex shedding around the shaft. The bilge vortex is generated from the ship hull body ahead and then shedding into the propeller plane. Thus, it locates around outer boundary layer $u/U_0=0.4\sim0.6$ covering larger area and moves up and down relatively to the vertical stern motion. And the positive vorticity corresponding to the counter-clockwise rotating vortex is produced. The vortex shedding around the shaft is caused by vertical stern motion. When stern moves up, a very low speed area beneath the shaft extends downward deeply to almost a propeller radius, like $t/T_e=0.5$ in Fig.7-20. The vortex sheds from the side of shaft into low speed area with longer length and negative vorticity corresponding to the clockwise rotating vortex. Meanwhile the bilge vortex is below and next to the shaft. When ship moves down, the vortex with negative vorticity would turn to shedding up and induces another small vortex with positive vorticity. In addition, the bilge vortex moves above the shaft, like $t/T_e=0.0$ in Fig.7-20. Because of the vortex shedding around the shaft, it locates at inner boundary layer $u/U_0=0.0\sim0.3$. Also, it has larger vorticity magnitude than bilge vortex has but occupies smaller area.

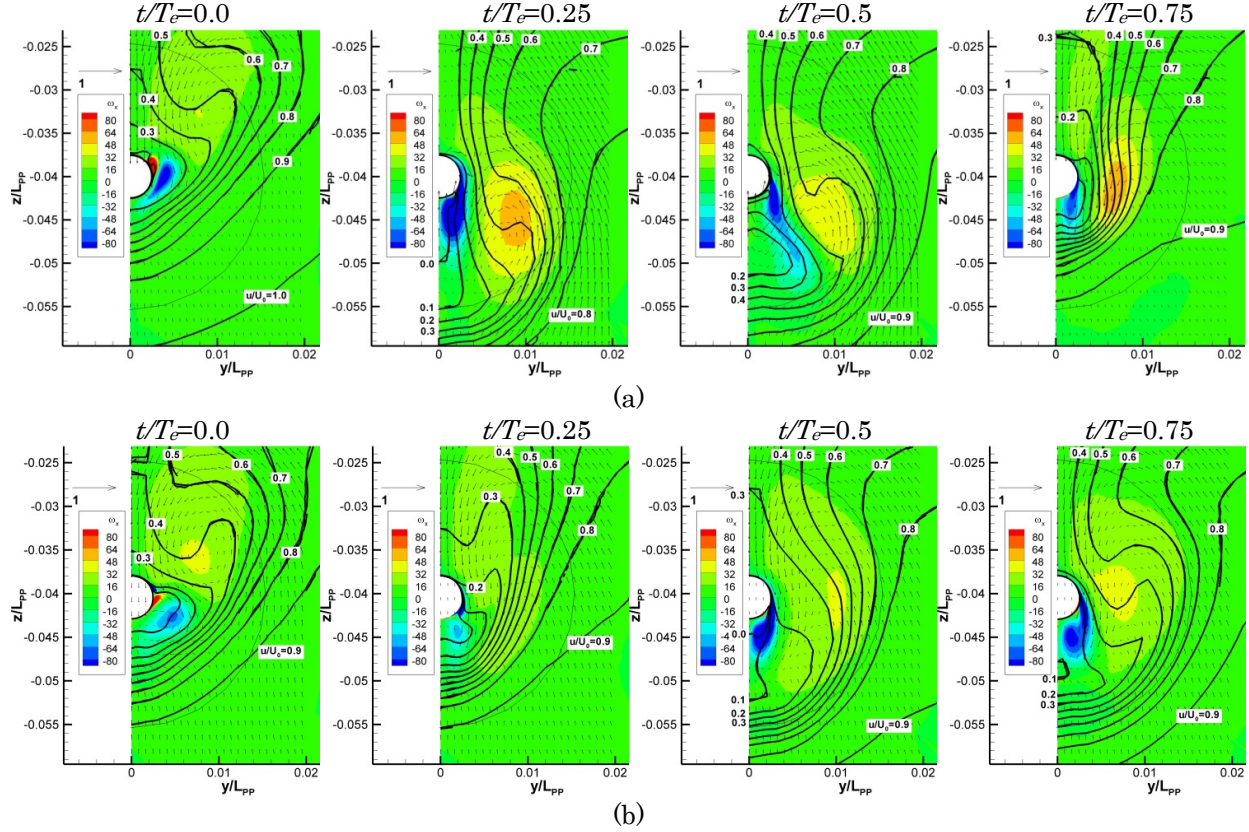


Fig. 7-20 Vortex behavior in one encounter period for $\lambda/L=1.1$ at fully-loaded condition. (a) $A/L=0.009375$. (b) $A/L=0.0046875$.

Although section 6.2.6 concludes the smaller wave amplitude does not show major influences on the RAOs and added resistance, Figure 7-20 shows the smaller magnitude of vorticity, smaller vortex and the shallower downward extension of the low speed area.

By integrating the vorticity along the propeller plane area $d\hat{A}$, the circulation Γ on the propeller plane is

$$\Gamma = \int_{r_0}^r \overrightarrow{\omega_x} \cdot d\hat{A} \quad (37)$$

where $r=r_p=0.01535L_{PP}$ for fully loaded condition and $\lambda/L=0.6$ of ballast condition. And $r=0.5r_p$ for $\lambda/L=0.9$ and 1.6 in ballast condition because the propeller would be out of water. r_p and $r_0=0.002379L_{PP}$ are the radius of propeller and hub, respectively. Γ for

calm water, $\lambda/L=0.6, 1.1/0.9$ and 1.6 for both loading condition are presented in Fig. 7-21 for one encounter period. $t/T_e=0.0$ is for the incident wave crest at $x/L=0.98$ (propeller plane). As the discussion for Figure 7-20, the vorticity shows very large magnitude: $\omega_x > +32$ for bilge vortex covering larger area and $\omega_x < -80$ for the vortex shedding around the shaft with smaller area. Thus, for Eq. (32) the positive and negative vorticity would almost cancel each other as shown in Fig. 7-21. The circulation is very small positive value suggesting bilge vortex's contribution is slightly larger. All cases have similar phase lag $\sim t/T_e=0.5$.

For fully-loaded condition, the man circulation $\bar{\Gamma}$ is 0.00341 for $\lambda/L=1.1$ which is very close to calm water circulation $\Gamma=0.00342$. $\bar{\Gamma}=0.00367$ for $\lambda/L=0.6$ and $\bar{\Gamma}=0.00351$ for $\lambda/L=1.6$ are larger than calm water one. However, all values for short wave ($\lambda/L=0.6$ and smaller wave amplitude ($\lambda/L=1.1$) are higher than calm water one with much smaller amplitude. It is because for smaller ship motion bilge vortex has smaller movement and size change but is still stronger than in calm water. For $\lambda/L=1.1$, although its $\bar{\Gamma}$ is similar to calm water one, the second harmonic component is obvious. The bilge vortex might move or grow in higher frequency. The 2nd harmonic component is not clear for $\lambda/L=0.6$ and 1.6 . The larger amplitude appears for $\lambda/L=1.6$ indicates that larger ship motion causes more intense periodic change of the bilge vortex.

For ballast condition, $\lambda/L=0.6$ in which the propeller is not out of water confirm the conclusion drawn for shorter waves. For $\lambda/L=0.9$ and 1.6 , because the propeller would be out of water at some instants, Eq. (32) would only be integrated up to $0.5r_p$. According to Figure 7-20, the $-\omega_x$ would be dominant inside 0.5 propeller radius, i.e. around the shaft mainly. Thus, $\bar{\Gamma} < 0$. Both values oscillating with much larger amplitudes reveal that the large ship motion in long waves causes intense periodic change of the low speed area.

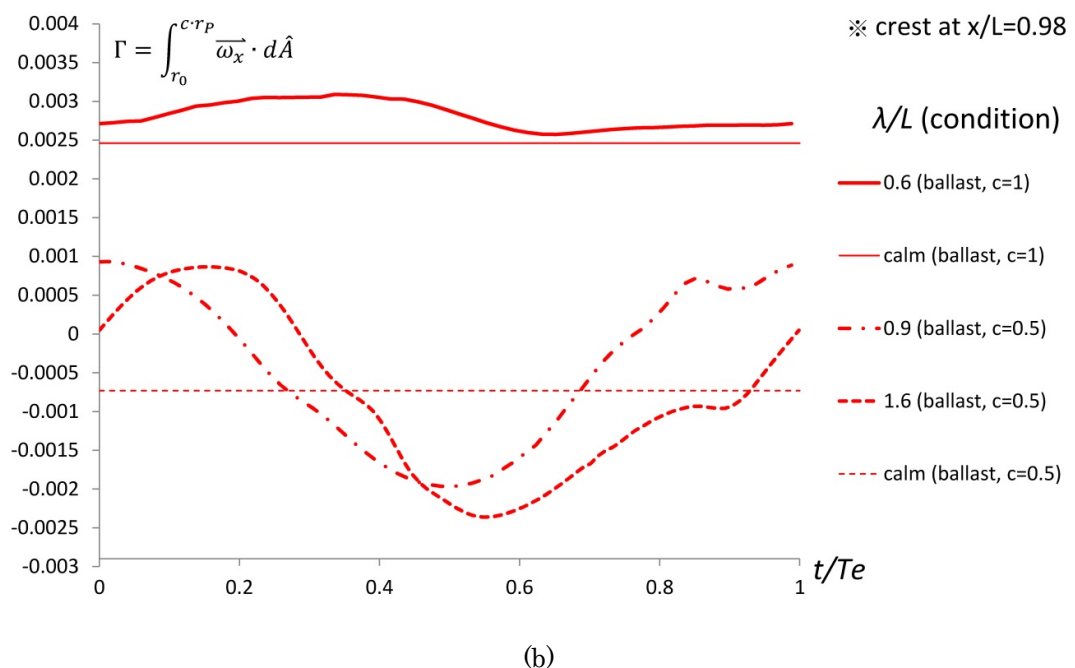
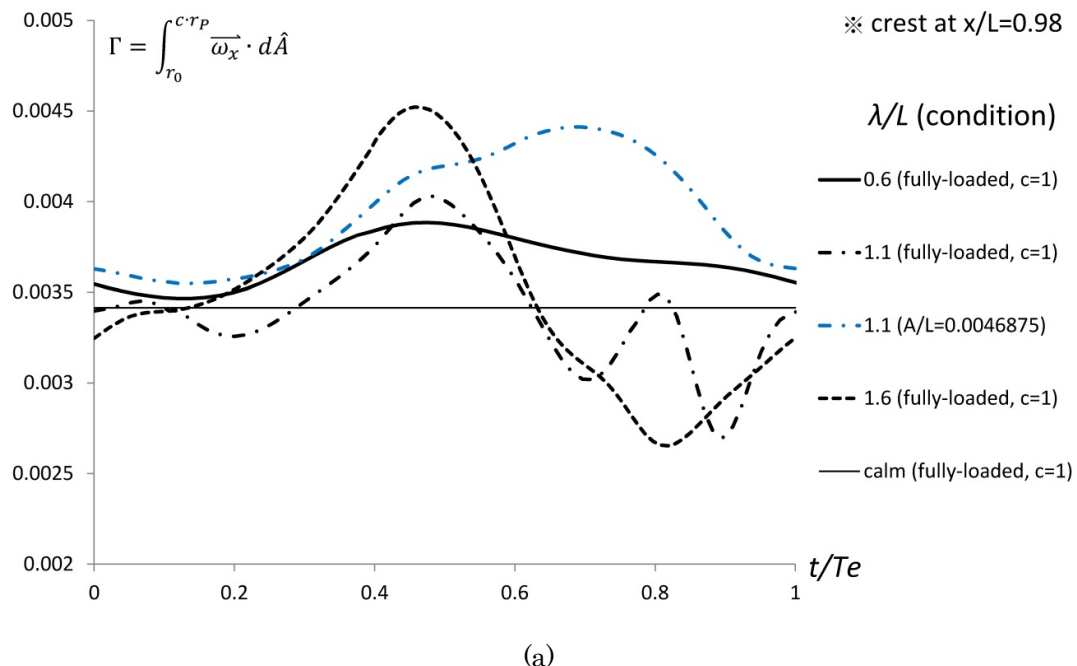


Fig. 7-21 Circulation at propeller plane in one encounter period. (a)
Fully-loaded condition. (b) Ballast condition.

b. Orbital velocity

Base on linear wave theory in deep water condition, axial component of potential flow (PF) orbital velocity u' and its amplitude u'_{max} at propeller plane $x/L=0.98$ under a certain water depth z are

$$u'(t) = \frac{\partial \phi}{\partial x} = A\omega e^{kz} \cos(kx' - \omega_e t)/U_0; u'_{max} = A\omega e^{kz}/U_0 \quad (38)$$

where ω_e is encounter frequency, $k=2\pi/\lambda$ is wave number, and $\omega = \sqrt{gk}$ is wave frequency. Also, $L=L_{pp}=3.2\text{m}$, $A=0.03\text{m}$, $g=9.81\text{m/s}^2$, $x=x/L-0.98$, $z/L=-0.04687$ for fully loaded condition and -0.01868 for ballast condition which is the z location of the propeller center under the undisturbed free surface $z_0=0$. The CFD orbital velocities $u/U_{\sigma 1}$ are extracted from the propeller center along several lateral positions to $y/L=2B/L=0.3626$. The total velocities, $u+1$ for PF and u/U_0 for CFD, are compared in Fig. 7-22. $t/T_e=0.0$ is for the incident wave crest at $x/L=0.98$.

The difference between orbital velocity amplitude u'_{2B} for CFD which is $|u/U_{\sigma 1}|$ at $2B$ and u'_{max} from Eq. (33) for PF is calculated in Table 7-1 as $E1$. $E1$ is less than 5% for $\lambda/L=0.6$ and 1.6 for both loading conditions as Figure 7-22 indicates that in the far field the waves behave the same for CFD and PF. For $\lambda/L=1.1$ in fully loaded condition and 0.9 in ballast condition, CFD has much smaller values. $2B$ lateral distance might be not far away enough from the ship for the cases having the largest added resistance. From Figure 7-22, by y/L closer to the hull the mean velocity decreases due to viscosity. However, the amplitude with phase lag increases because of the pressure gradient between inner and outer boundary layer. And for long waves such as $\lambda/L=1.1/0.9$ and 1.6, the 2nd harmonic components are observed. It is caused by the disturbance from bilge vortex moving relatively to ship motion which is larger in longer waves.

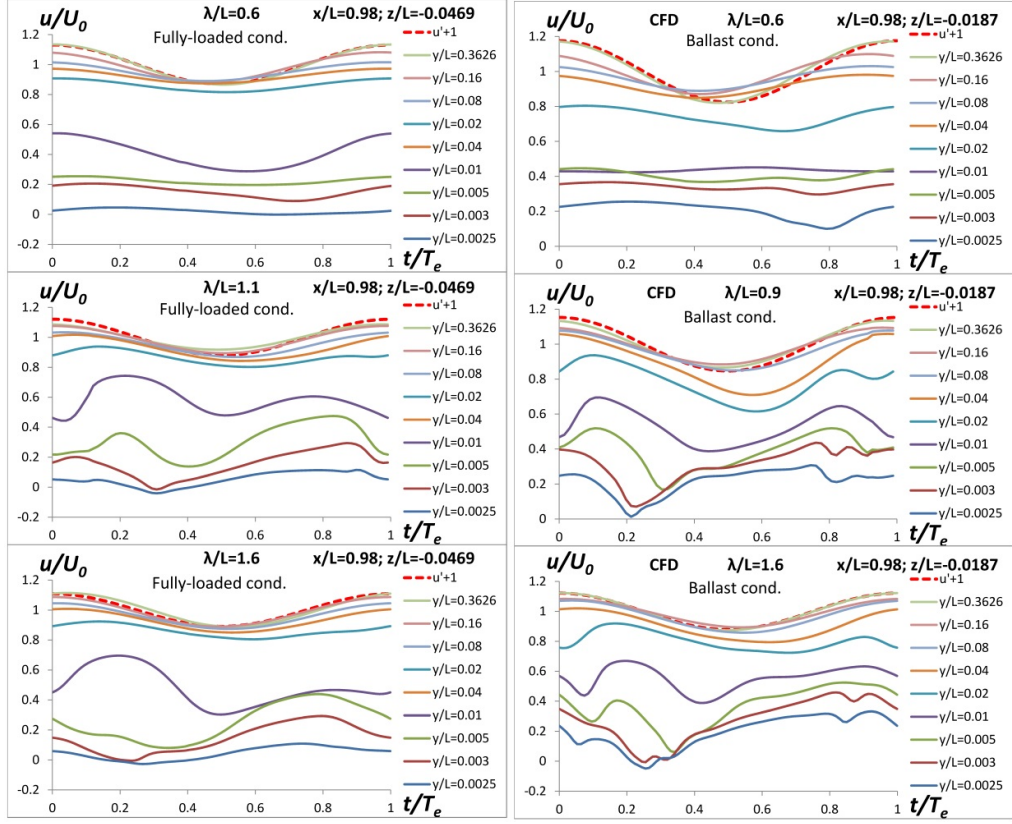


Fig. 7-22 Total velocities (ship speed+orbital velocities) at different lateral distances

Table 7-1 Orbital velocity and time average of volume average velocity.

		CFD			PF		
	λ/L	\bar{u}_N	$ u_N $	u'_{2B}	u'_{max}	$E1(\%)^*$	$E2(\%)^{**}$
Fully-loaded condition $r=r_p$	calm	0.4104	-	-	-	-	-
	0.6	0.4341	0.06485	0.1344	0.1308	-2.75	50.42
	1.1	0.5173	0.1222	0.08623	0.1207	28.56	-1.24
	1.6	0.4754	0.1192	0.1142	0.1088	-4.96	-9.56
Ballast condition $r=r_p$	calm	0.4283	-	-	-	-	-
	0.6	0.4393	0.0430	0.1717	0.1757	2.27	75.53
Ballast condition $r=0.5r_p$	calm	0.3650	-	-	-	-	-
	0.9	0.3778	0.1105	0.1342	0.1531	12.34	27.82
	1.6	0.3595	0.1324	0.1219	0.1216	-0.25	-8.88

* $E1(\%) = 100 * (u'_{max} - u'_{2B})/u'_{max}$

** $E2(\%) = 100 * (u'_{max} - |u_N|)/u'_{max}$

c. Volume mean velocity

By integrating the axial velocity distributing on the propeller plane, the volume average nominal wake velocity u_N could be computed

$$u_N = \frac{1}{\pi(r^2 - r_0^2)} \int_{r_0}^r u d\hat{A} \quad (39)$$

The CFD result of u_N for one encounter period is showed in Figure 7-23 for $\lambda/L=0.6$, 1.1/0.9 and 1.6 for both loading condition in comparison with calm water value. $t/T_e=0$ is for the incident wave crest at $x/L=0.98$.

A linear method to estimate u_N is proposed to compare with the CFD result too. If calm water u_{N_calm} is given, u_{N_linear} in waves could be estimated from Eq. (38) by

$$u_{N_linear}(t) = u_{N_calm} + u'_{max} \cos(\omega_e t) \quad (40)$$

Table 7-1 listed the time average of volume average nominal wake velocity \bar{u}_N and its amplitude $|u_N|$. The linear method uses CFD calm water \bar{u}_N for u_{N_calm} and PF orbital velocity amplitude u'_{max} . Both methods are compared in Figure 7-24 for one encounter period.

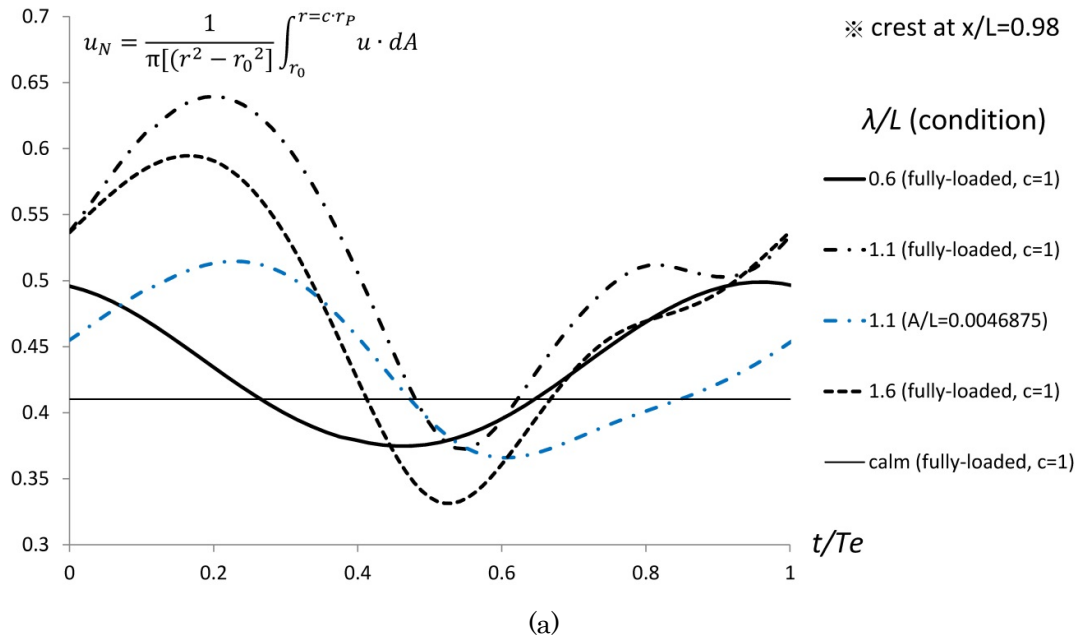
For the difference between \bar{u}_N , \bar{u}_N in waves would be higher than the calm water one explaining the added resistance. For fully-loaded condition, the difference is larger for $\lambda/L=1.1$ and smaller in short ($\lambda/L=0.6$) and long wave ($\lambda/L=1.6$). It might be related to the trend of the added resistance: it hits the peak at $\lambda/L=1.1$, and drops for shorter and longer waves (Figure 6-9). And \bar{u}_N of $\lambda/L=0.6$ (including both loading conditions) is very close to the calm water value because of smaller ship motion in short waves. For ballast condition, the ship has smaller draft and CB. Thus, its calm water \bar{u}_N is higher than the calm water value for fully-loaded condition. Also, \bar{u}_N of $\lambda/L=0.6$ in ballast condition is larger than that in fully-loaded condition. For the case with propeller out of water

($\lambda/L=0.9$ and 1.6 in ballast condition), \bar{u}_N inside $r=0.5r_p$ is smaller because it is in the inner boundary layer. However, they are very close to the calm water value, $\lambda/L=1.6$ even has slightly smaller values. It implies that the larger ship motion might not have much influence on the \bar{u}_N for smaller propeller radius or in more inside of the boundary layer. It means that the main difference between \bar{u}_N in waves and calm water, i.e. the source of the added resistance, is from the bilge vortex moving and changing in the middle layer of the boundary layer.

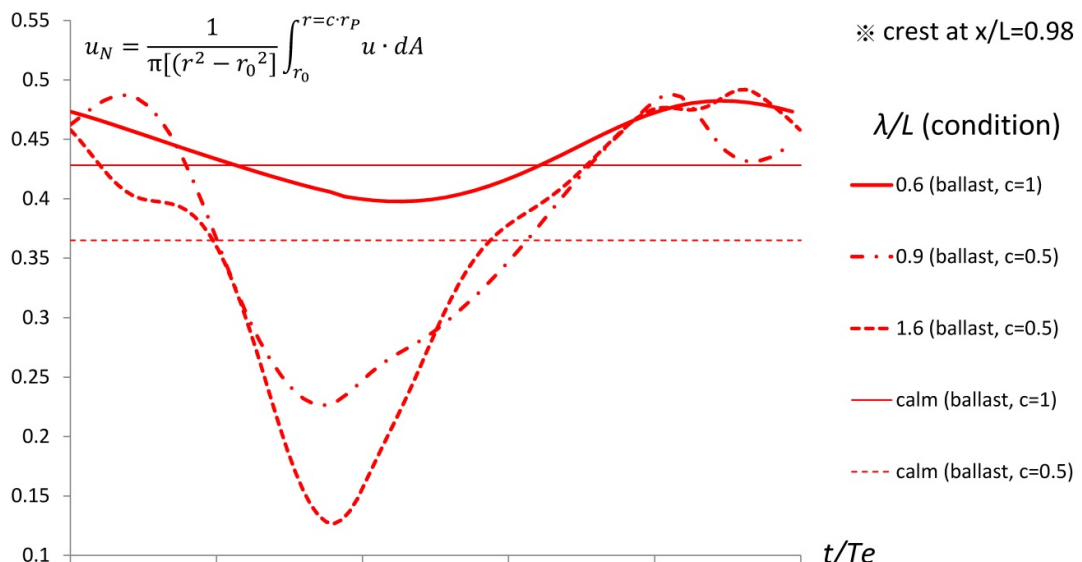
Unlike mean value \bar{u}_N , for the short waves $\lambda/L=0.6$ of both loading condition the amplitude of the linear method are much larger than CFD has ($E2=50\%$ and 76% in Table 7-1). For longer waves, the amplitudes of CFD and linear method have smaller difference instead (except for $\lambda/L=0.9$ in ballast condition). CFD's amplitudes are very lightly larger. $E2$ is only -1% for $\lambda/L=1.1$ in fully-loaded condition and around -9% for $\lambda/L=1.6$ in both loading conditions. In longer waves the orbital velocity could keep the amplitude even close to the ship. It is because of the larger pressure gradient caused by larger ship motion mentioned in the previous section. In short wave, the orbital velocity amplitude decay significantly close to the ship.

For the phase lag, more deviation is observed obviously in Figure 7-23. Also, the 2nd harmonic component ignored in linear method could be seen clearly. In long waves, the added resistance is dominated by ship motions. The large ship motion produces more disturbances such as phase lag and 2nd harmonic component on waves.

In the conclusion, it is possible to use linear method conditionally to estimate u_N PF amplitude for long waves and calm water value for mean value in short waves.



(a)



(b)

Fig. 7-23 Volume average nominal wake velocities. (a) Fully-loaded condition.
(b) Ballast condition

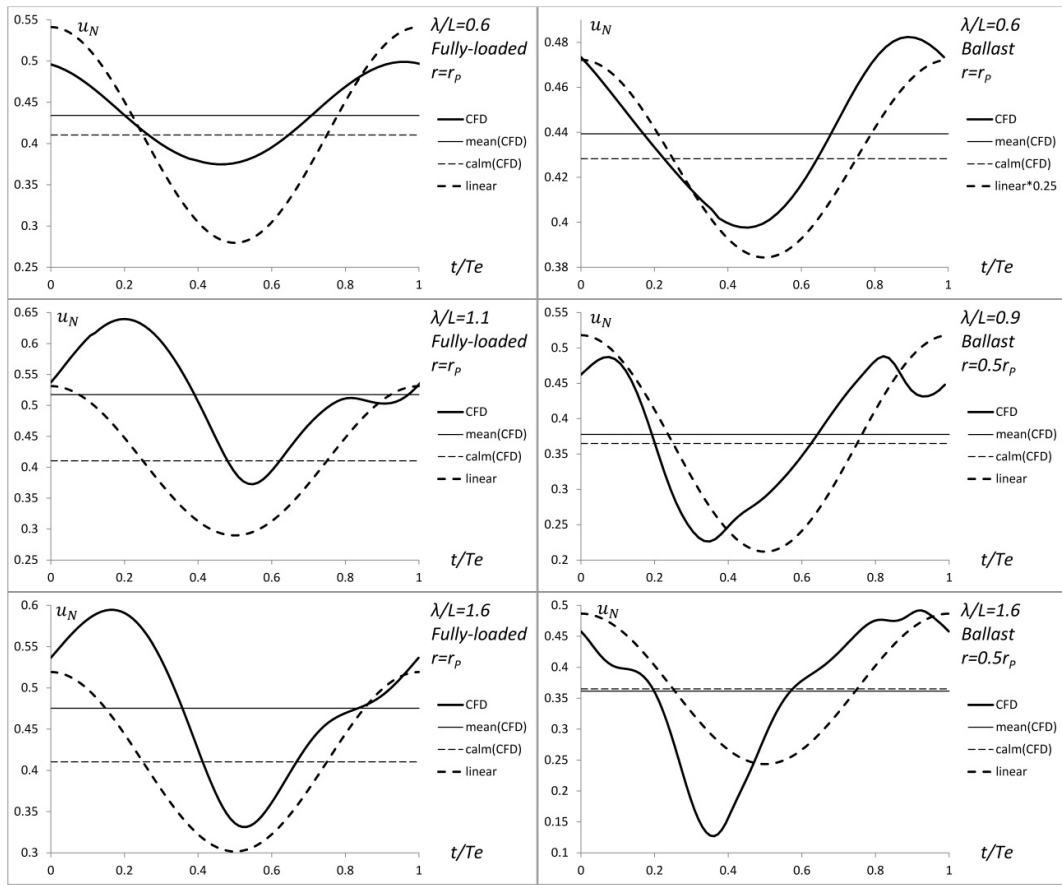


Fig. 7-24 The comparison of u_N by CFD and linear method.

d. Fourier analysis on propeller plane

In comparison of axial velocity distribution at propeller plane, Figure 7-25 shows the calm water result, Fig.7-26 and 7-27 are the harmonic components by Fourier analysis for $\lambda/L=0.6, 1.1$ and 1.6 (from left to right) for both loading conditions. Here, ZCG is at $z=0$ and incident wave crest at $x/L=0.0$ when $t/T_e=0$.

For mean value component, only $\lambda/L=0.6$ for both loading conditions has similar

pattern to the calm water one. As the discussion for Table 7-1 and Figure 7-23/24 also reveals, \bar{u}_N of $\lambda/L=0.6$ is close to calm water values. It might be due to the smaller ship motion in short waves.

For fully-loaded condition, the largest 1st harmonic amplitude under the keel is observed in $\lambda/L=0.9$ and 1.6. It corresponds to the low speed area extending beneath the shaft induced by the larger ship motion in long waves. For the main component of the 2nd harmonic, its location is related to the generation and movement of bilge vortex. For $\lambda/L=0.6$, because of small ship motion the contribution of the low speed area under the shaft is not clear. The bilge vortex is governing in both harmonics. For wave amplitude effect, the results of $\lambda/L=1.1$ for two difference A/L are showed in the figure too. The similar phenomena are showed for both harmonics but with smaller maximum amplitude. And the mean value of the smaller wave amplitude is closer to the calm water one because of smaller ship motion. Same conclusion is gained in Figure 7-23 (a).

For ballast condition, $\lambda/L=1.6$ shows the similar phenomena with the long waves for fully-loaded condition. For $\lambda/L=0.6$ and 0.9, unlike in fully-loaded condition, the main contribution in both harmonics becomes the low speed area below the shaft.

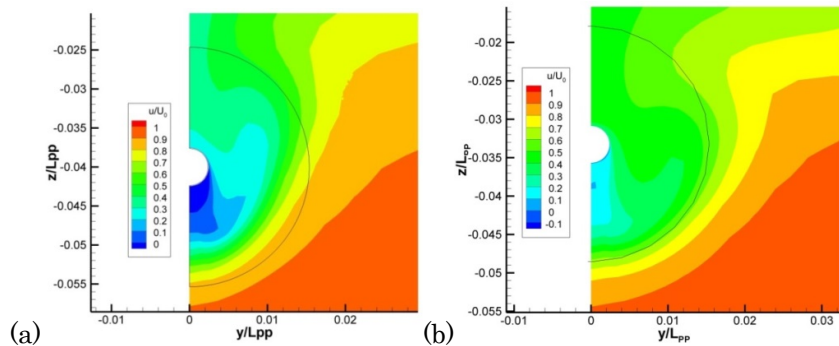


Fig. 7-25 Axial velocity distribution at propeller plane in calm water.
(a) Fully loaded condition; (b) Ballast condition.

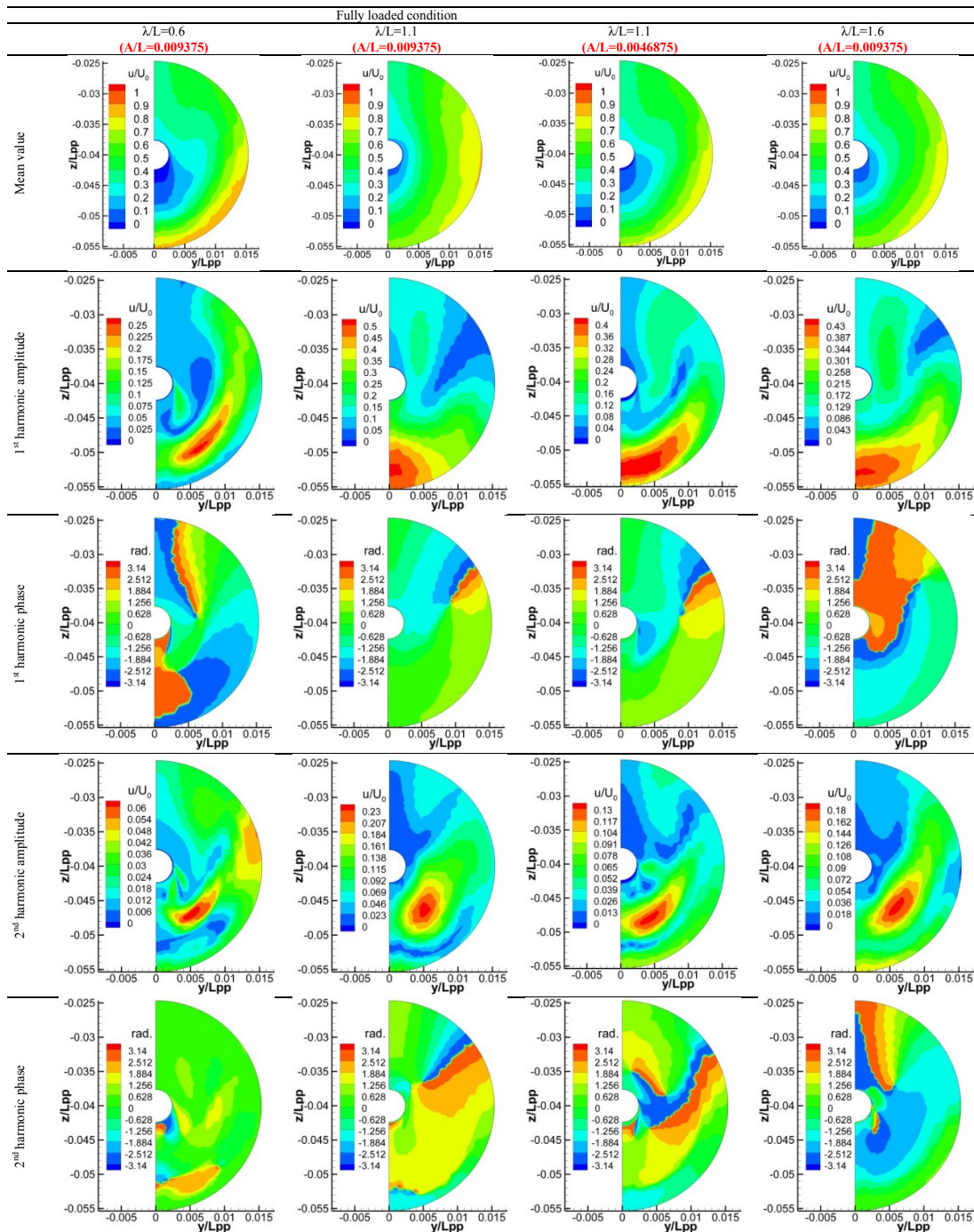


Fig. 7-26 Fourier analysis on axial velocity distribution at propeller plane for fully loaded condition.

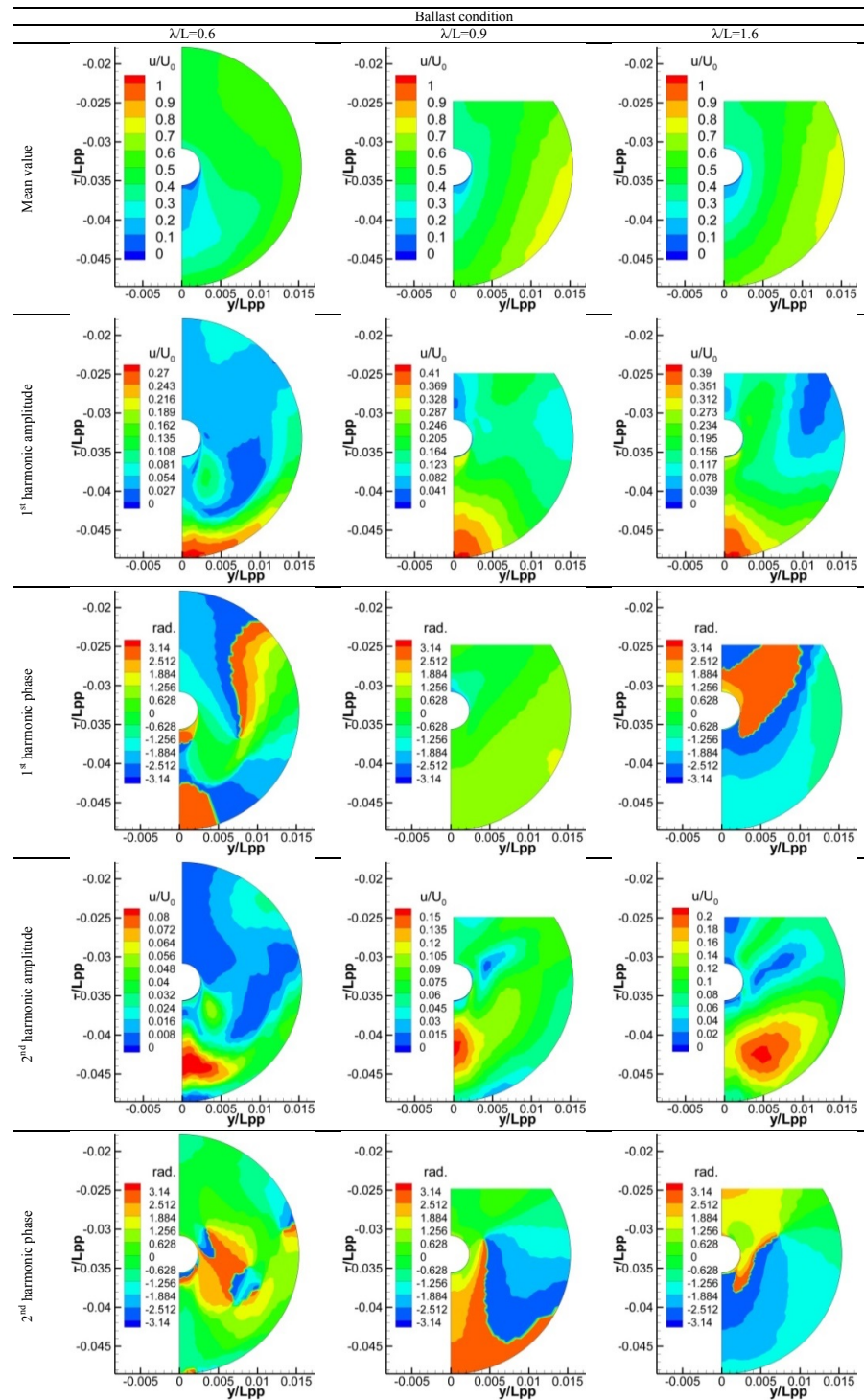


Fig. 7-27 Fourier analysis on axial velocity distribution at propeller plane for ballast condition.

e. Simple estimate for thrust and torque

Since the flow velocity (u, v, w) at each points on the propeller plane in waves are solved by CFD for one encounter period, as discussed in section 7.3.3a. To study the thrust and torque in waves, a simple estimate method using blade element theory (BET; Yokota, 2013) with the CFD (u, v, w) result on propeller plane as the input/inflow are proposed here. It is a simple estimate which means that there is no interaction between RANS solver and BET subroutine. The test condition is at KVLCC2's self-propulsion points $J=0.5$ for $\lambda/L=1.1$, fully-loaded condition and fixed surge. The estimated thrust coefficient K_T would oscillate corresponding to the volume average nominal wake velocity u_N (section 7.3.3c and Eq. (39)) with an inverse trend as expected in Figure 7-28. The higher u_N implies higher inflow velocity into the propeller plane but generates the lower thrust. Also, compared with calm water values, the average K_T in waves would be smaller. Instead, mean value of u_N in waves is higher than calm water value. It suggests that the propeller inflow velocity in waves is larger and produces smaller thrust compared with that in calm water. On the other hand, the periodic change of torque coefficient K_Q in waves has the same similar trend (such as phase lag) to u_N .

The periodic change to local thrust and torque in waves also could be obtained and compared with the thrust and torque distribution in calm water. As shown in Figure 7-29(a), in calm water the high local thrust area would cover on star board side because of right rotating (clockwise) propeller. The highest thrust would be under the shaft due to the low speed area beneath it. However, the local thrust in waves, as shown in Figure 7-30(a) in one-quarter encounter period, has higher and lower magnitude in turn in the upper and lower part of propeller plane. For the local torque, Figure 7-29(b) indicates

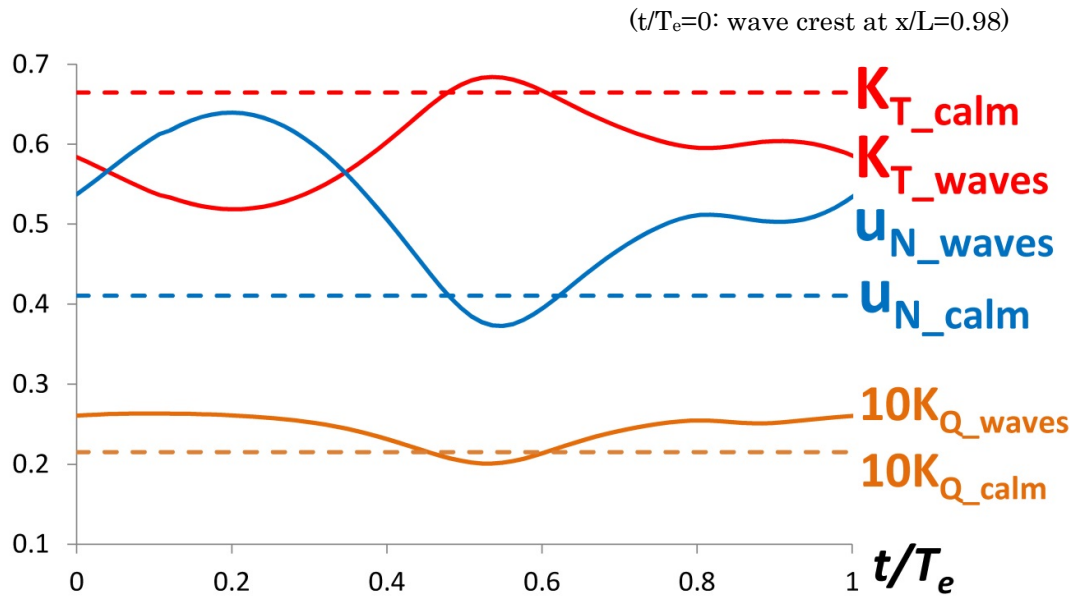


Fig. 7-28 Thrust estimate in one encounter period.

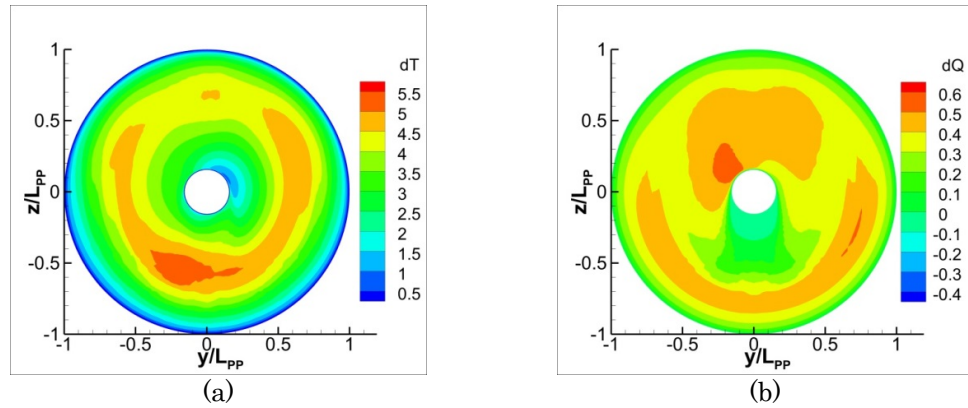


Fig. 7-29 Estimated local propeller performance in calm water. (a) Thrust. (b) Torque

in calm water the small negative values below the shaft, and higher positive values are above the shaft and in the outer area under the shaft. In waves, the negative values has larger magnitude, such as $t/T_e=0.5$ in Figure 7-30(b). The positive values with larger magnitude and covering larger area move up and down on the both side of propeller plane in one encounter period.

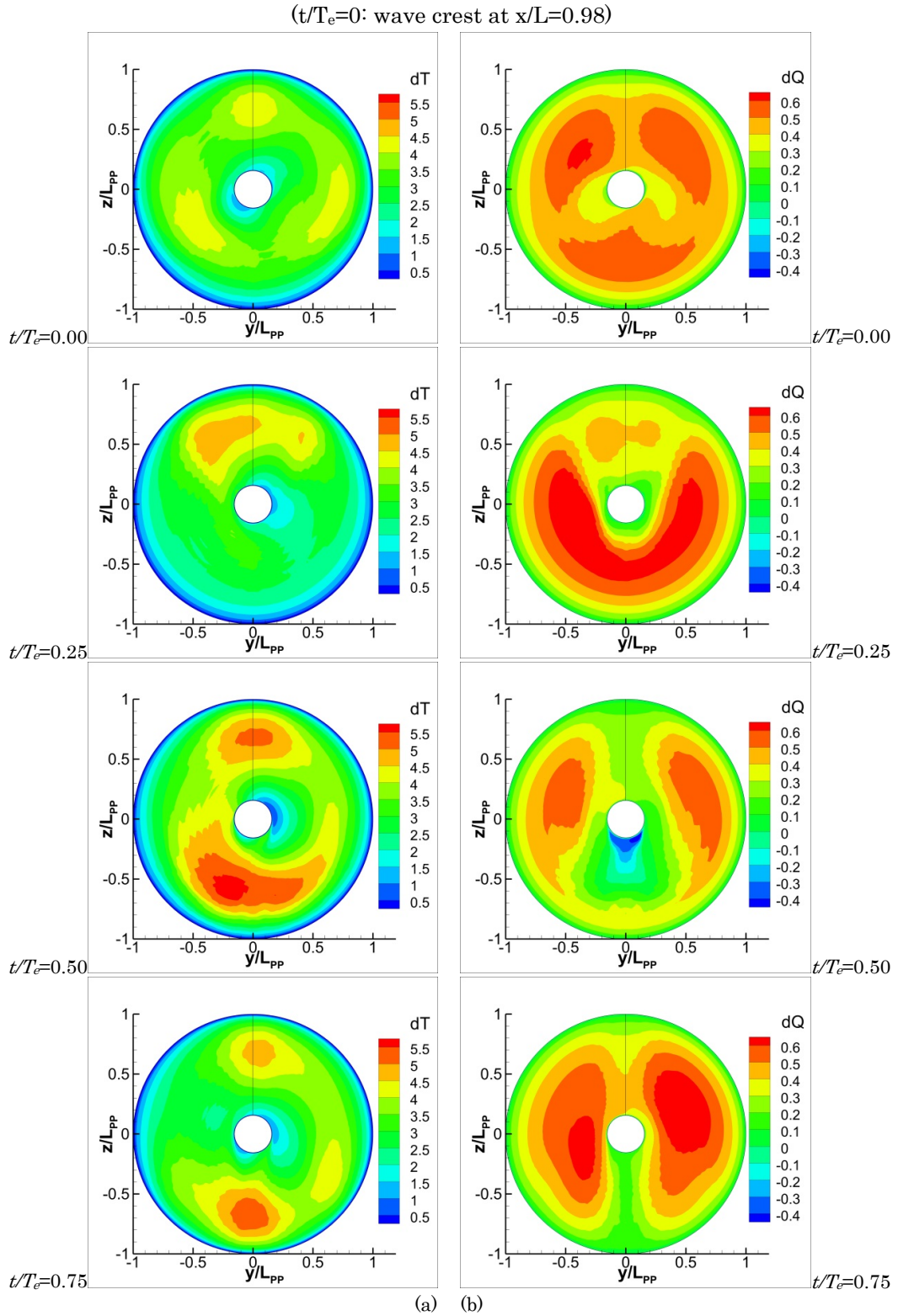


Fig. 7-30 Estimated local propeller performance in waves for one-quarter encounter period. (a) Thrust. (b) Torque

CHAPTER 8: CONCLUSION AND FUTURE WORK

The motions and added resistance of KVLCC2 tanker under fully-loaded and ballast condition advancing at $Fr=0.142$ with fixed and free surge in head waves are validated for a wide range of wave length condition including very short waves. The verification, natural heave and pitch frequencies, effects of higher ship speed and the conditions for maximum added resistance and ship motions are investigated. The CFD results are compared with the potential flow predictions and the decomposition of total forces into Froude-Krylov, diffraction and radiation is evaluated. Lastly, the local flow is analyzed and the wake field at propeller plane is validated against PIV measurements.

The verification studies showed grid, time step and iterative uncertainty of about $U_G = 2.5\%S_I$, $U_T = 1.60\%S_I$ and $U_I = 1.3\%S_I$ such that the total simulation uncertainty of $U_{SN} = 3.46\%S_I$ meaning the results are fairly insensitive to the grid size and time step.

The coupled and uncoupled natural frequency of vertical motions are investigated at $Fr=0.0$ and compared with the empirical values. For heave, the coupled, uncoupled and empirical natural frequency are fairly close while large differences are observed between the coupled, uncoupled and empirical pitch natural frequency. The coupled pitch natural frequency is about 90% of the uncoupled frequency and 83% of the empirical one. The predicted responses in waves confirmed the coupled heave and pitch frequency values.

For resistance in calm water, EFD data is available from different facilities. The facility bias is $U_{FB} = 11.2\%$ for resistance. The large facility bias for resistance is due to the difference in the model length size in different facilities. The facility biases for sinkage and trim are about 20% and 12%, respectively. The error for CFD resistance

prediction at $Fr=0.142$ compared with OU and INSEAN data is 7.8%D and 6.8%D, respectively. The sinkage and trim are predicted by 2.2%D/25.3%D and 4%D/12.8%D for OU/INSEAN data. The large comparison error for INSEAN is due to the fact that the motions provided by INSEAN are far away from the values provided by other facilities. Comparing the CFD results at $Fr=0.142$ and $Fr=0.25$ shows that the total resistance is nearly doubled from $Fr=0.142$ to $Fr=0.25$ and the sinkage and trim are about four times larger. The comparison of CFD predictions at $Fr=0.142$ and larger Reynolds number with NTNU data shows average prediction error of 6%D.

CFD time histories for $\lambda/L = 0.6, 1.1$ and 1.6 at $Fr=0.142$ show good agreement with EFD. The time histories show that both EFD and CFD data for free and fixed surge do not converge well mostly for heave and pitch mean values. Also, the time histories display sinusoidal oscillation for motions while the axial force includes higher harmonics for $\lambda/L = 1.1$.

For fully-loaded condition, CFD predicts 1st harmonic amplitude and phases of motions with the average of 7.85%D and 4.28% 2π , respectively. For the mean values the errors are large as the EFD data is too scattered. The largest amplitude of EFD and CFD bow relative motion occurs around $\lambda/L=1.2$ where the phase lag between the wave signal and bow motion is close to 180 deg and also the amplitudes of the motions are large. CFD indicates no significant differences between free and fixed surge while in EFD there is difference for pitch motion at $\lambda/L = 1.6$. The CFD simulations for the higher ship speed ($Fr=0.25$) show larger value for heave amplitude with the peak shifted to longer waves. The phases are unchanged by increasing ship speed and the mean values raise to the dynamic sinkage and trim at $Fr=0.25$. The bow relative motion at $Fr=0.25$ shifts to longer waves but the peak is similar to that for $Fr=0.142$.

For ballast condition, the average error of the 1st harmonic amplitude of surge motion is 31%D. For the 1st harmonic amplitude of heave motion, the average error is about 5%D. The fine grids would improve the error, especially for the short wave condition (2.75%D in average). In regard of pitch motion, the error increases as λ/L decreases from 0.9 to 0.3 but the very good agreement for $\lambda/L=1.1$ and 1.6: around 1% for fixed surge condition and less than 1% for free surge condition are presented. For the added resistance, CFD predicted the added resistance with 18%D error for fixed and free surge condition. The fine grid improves the prediction error to 12%D in average.

The forces show that CFD under predicts the 1st harmonic amplitude of surge force by average of 35%D at Fr=0.142. The components of surge force and pitch moment show a peak for wave excitation component near $\lambda/L=1.33$ and for radiation near the resonance condition. The components of heave force shows largest wave excitation force for longest wave length and largest radiation force near the resonance condition. The summation of excitation and radiation force/moment considering their phase difference estimates 1st harmonics of total forces/moments very well but not the 2nd harmonics, suggesting nonlinear interaction between higher order components. The 2nd harmonics components show that the nonlinearity originates from the radiation in long waves and from diffraction in very short waves. CFD predicts the trend of the added resistance very well. The added resistance was largest near the wave length condition for maximum bow relative motion showing strong correlation between the added resistance and bow relative motion. CFD indicates no variation of the added resistance for free and fixed surge while EFD added resistance at $\lambda/L=1.6$ is changed. The results for very short waves show the added resistance coefficient increases slightly with decreasing λ/L . The results for higher ship speed Fr=0.25 shows that increasing speed shifts the added

resistance peak to longer wave length but the peak value is not changed similar to that for bow relative motion showing the correlation of the added resistance with bow relative motion.

Maximum motions occur when the total forces/moment are maximum i.e. the wave excitation and radiation components are maximum. For surge and pitch, wave excitation component is maximum around $\lambda/L=1.33$ and radiation is maximum near the resonance condition. At a given speed and variant wave length, the peak for surge/pitch motion occurs at a wave length near both $\lambda/L=1.33$ and resonance condition as shown by the results at $Fr=0.142$. For variant speed and wave length, the overall peak for surge/pitch motion occurs when the peaks for wave excitation and radiation components overlap. This happens at $Fr=0.082$ which is not simulated in this study. For heave, wave excitation force is maximum at long waves and radiation is maximum near the resonance condition. For a given speed and variant wave length, the peak of heave force and accordingly heave motion occurs in long waves and near the wave length corresponding to the resonance condition as shown for both $Fr=0.142$ and $Fr=0.25$. For variant speed and wave length, the overall peak for heave motion occurs when the peaks for wave excitation and radiation overlap. The comparison of the heave motions for $Fr=0.142$ and 0.25 shows that $Fr=0.25$ provides large heave motion since the resonance condition and thus the peak of radiation force is shifted from $\lambda/L=1.4$ to $\lambda/L=1.6$ where the weave excitation force is larger. The coincidence of the peaks for wave excitation and radiation forces increases the ship motions and accordingly the bow and stern motions. However, the bow and stern relative motions might not increase as they do also depend on the phase between the wave and the bow and stern motions.

The average errors of EUT predictions for surge, heave and pitch are 30.3%D and

8.6% 2π , for amplitudes and phases, respectively, which are larger than those for CFD.

The added resistance predicted by EUT provides $E=24\%D$ and is compared with the predictions by Gerritsma and Beukelman method and Faltinsen asymptotic formula. It is confirmed that the Faltinsen asymptotic formula provides good prediction of added resistance in short waves. Comparing the components of forces with CFD show that EUT predicts the components and the total forces fairly well for heave and pitch while the excitation force and the total force is not predicted well for surge motion.

The local flow analysis shows that the added resistance is mainly induced by high pressure acting on the upper bow. The size of the high pressure region correlates with the bow relative motion which increases to its maximum around $\lambda/L=1.1$ close to the location of the peak of added resistance. The unsteady wave pattern analysis shows the added resistance is the result of the energy loss from the generated radiation and diffraction waves initiating at fore-body shoulder and transom corner and diverging from the model. The CFD wake field at propeller plane shows very good agreement with PIV measurement. The wake field was compressed when the aft was located on the wave crest and then it was expanded in wave trough. Two sources of the vortex system in the wake are observed: bilge vortex generated from the hull body and shedding into the propeller plane, and the low speed area induced by vertical stern motion and shedding around the shaft. By the studies of circulation and volume average axial velocity on the propeller plane, the vortex behavior is understood. The simple estimate of propeller performance indicates the periodic change of thrust and torque and their local distribution. Those variables in waves show their mean values are different from the calm water one and their fluctuations have phase lag and 2nd harmonic component.

For future work, the bow shape optimization can be promising to reduce the added

resistance. The added resistance and its correlation with bow relative motion for high speed ships and in regular and irregular waves with different heading should be investigated. The conditions for maximum ship motions should be studied for the waves with larger H/λ to investigate the nonlinear interaction between the components of the forces. The study of effective wake and self-propulsion test in waves are expected.

References

Bingjie G. and Steen S.: Added resistance of a VLCC in short waves. 29th Intl Conf. on Ocean offshore and Arctic Engineering. OMAE, Shanghai, China, 2010

Boese P.: Eine einfache methode zur berechnung der winderstancershohung eines schiffes im seegang. Schiffstechnik 17 (86), 1970.

Blok J.J.: The resistance increase of a ship in waves. PhD thesis, Delft University of Technology, 1983.

Bunnik T. et al.: A comparative study on state-of-the-art prediction tools for seakeeping. 28th Symposium on Naval Hydrodynamics, Pasadena, California, 2010.

Carrica P.M. et al.: Large-scale DES computations of the forward speed diffraction and pitch and heave problems for a surface combatant. Computer & Fluids, Vol. 39, Issue 7, pp. 1095-1111, 2010.

Carrica P.M. et al.: Ship motions using single-phase level set with dynamic overset grids. Computers & Fluids, Vol. 36, Issue 9, pp. 1415-1433, 2007.

Castiglione T. et al.: Numerical investigation of the seakeeping behavior of a catamaran advancing in regular head waves. Ocean Engineering, Vol. 38, Issue 16, pp 1806-1822, 2009.

Dallinga R.P. et al.: Seakeeping Issues in the Design of Containerships. MARIN, Netherlands, 2008.

Deng G.B. et al.: Verification and validation for unsteady computation. Gothenburg 2010: A Workshop on CFD in Ship Hydrodynamics, 2010.

Duan W. and Li C.: Estimate of added resistance for large blunt ship in waves. *Journal of Marine Science and Application*, Vol. 12, Issue 1, pp1-12, 2013.

Erwandi and Suzuki T.: Analysis of diffraction waves around a ship using projected light distribution method. *Journal of Society of Naval Architecture of Japan* (spring meeting), Vol. 189, pp 1-12, 2001.

Fabbri L. Campana E. and Simonsen C.: An Experimental Study of the Water Depth Effects on the KVLCC2 Tanker. *AVT-189 Specialists Meeting on Assessment of Stability and Control Prediction Methods for NATO Air and Sea Vehicles*, Portsdown West, UK, 2011.

Faltinsen O.M. et al.: Prediction of resistance and propulsion of a ship in a seaway. *Proc. of the 13th Symposium on Naval Hydrodynamics*, Tokyo, pp. 505–529, 1980.

Faltinsen O.M.: *Sea loads on ships and offshore structures*. Cambridge University press, Cambridge, UK, 1990.

Fang M.-C. and Chen G.-R.: On the nonlinear hydrodynamic forces for a ship advancing in waves. *Ocean Engineering*, Vol. 33, pp 2119-2134, 2006.

Gerritsma J. and Beukelman W.: Analysis of the resistance increase in waves of a fast cargo ship. *International Shipbuilding Progress* 19 (217), 1972.

Ghani M. and Julait J.: Prediction of added resistance of ship due to regular head waves. *Jurnal Mekanikal*, No. 26, pp.1-8, 2008.

Grigoropoulos G.J. Loukakisa T.A. and Perakis A.N.: Seakeeping standard series for oblique seas (a synopsis). *Ocean Engineering*, Vol. 27, pp. 111–126, 2000.

Gui L. et al.: Forces, moments, and wave pattern for surface combatant in regular head

waves: Part II. Measurement results and discussions. *Experiments in Fluids*, Vol. 32, pp 27-36, 2002.

Guo B.J. Steen S. and Deng G.B.: Seakeeping prediction of KVLCC2 in head waves with RANS. *Applied Ocean Research*, Vol. 35, pp. 56-67, 2012.

Hayashi Y.: Phase-averaged 3DPIV flow field measurement for KVLCC2 model in waves. M.S. thesis (in Japanese), Osaka University, 2012.

He W. et al.: Uncertainty Quantification of Delft Catamaran Total/Added Resistance and Motions in Irregular and Variable Regular Head Wave: Supplemental Materials. 29th Symposium on Naval Hydrodynamics, Gothenburg, Sweden, 2012.

Irvine M. Longo J. and Stern F.: Pitch and heave tests and uncertainty assessment for a surface combatant in regular waves. *J. Ship Research*, Vol. 52, pp.146-163, 2008.

Journee J.M.J: Motions and Resistance of a Ship in Regular head Waves. Report428, Ship hydromechanics laboratory, Delft University of Technology, 1976.

Journee J.M.J: Experiments and Calculations on 4 Wigley Hull Forms in Head Waves. Report 0909, Ship hydromechanics laboratory, Delft University of Technology, 1992.

Journee J.M.J: Verification and Validation of Ship Motion Program SEAWAY. Report1213a, Ship hydromechanics laboratory ,Delft U. of Technology, 2001.

Joncquez S.A.G. Bingham H. and Andersen P: Validation of Added Resistance Computations by a Potential-Flow Boundary-Element Method. 27th Symposium on Naval Hydrodynamics, Seoul, Korea, 2008.

Kandasamy M. et al.: Integral force/moment water-jet model for CFD simulations. *Journal of Fluids Engineering*, Vol. 132, Issue 10, pp 101-103, 2010.

Kashiwagi M.: Prediction of Surge and Its Effect on Added Resistance by Means of the Enhanced Unified Theory. Transactions of West-Japan Society of Naval Architects, Vol. 89, pp.77-89, 1995.

Kashiwagi M. et al.: An Analysis System For Propulsive Performance in Waves. Journal of Kansai Society of Naval Architecture of Japan, No. 241, pp.67-82, 2004.

Kashiwagi M.: Impact of hull design on added resistance in waves— application of the enhanced unified theory. Proceedings of the 10th International Marine Design Conference, Trondheim, Norway, pp.521–535, 2009.

Kashiwagi M.: Hydrodynamic Study on Added Resistance Using Unsteady Wave Analysis. 34th Weinblum Memorial Lecture, 2011.

Kashiwagi M.: Hydrodynamic Study on Added Resistance Using Unsteady Wave Analysis. Manuscript to be submitted to Journal of Ship Research , 2013.

Kim J. et al.: Feasibility study on numerical towing tank applications of resistance and self-propulsion performance for a ship. Gothenburg 2010: A Workshop on CFD in Ship Hydrodynamics, 2010.

Kim K.-H. et al.: Numerical Analysis on Added Resistance of Ships in Time-domain. Proceedings of 25th International Workshop on Water Waves and Floating Bodies, Harbin, China, 2010.

Larsson L. Stern F. and Visonneau M. (editors): Gothenburg 2010: A Workshop on Numerical Ship Hydrodynamics. Gothenburg, Sweden, 2010.

Lewis E.V.: Principles of naval architecture, vol. III: Motions in waves and controllability. The society of Naval Architects and Marine Engineers, NJ, 1989.

Liu S. Papanikolaou A. and Zaraphonitis G.: Prediction of added resistance of ships in waves. *Ocean Engineering*, Vol. 38, Issue 4, 2010.

Matsumoto K. et al.: BEAK-BOW to reduce the wave added resistance at sea. 7th interl sym. on practical design of ships and mobile units, Hague, Natherlands ,pp. 521-526, 1998.

Matsumoto K.: “Ax-Bow”: a new energy-saving bow shape at sea. *NKK Technical Review*, No. 86, pp46-47, 2002.

Maruo H.: The excess resistance of a ship in rough seas. *International Shipbuilding Progress* 4 (35), 1957.

Maruo H.: Resistance in waves. 60th anniversary Series, *The Society of Naval Architects of Japan*, 8, pp 67–102, 1963.

McTaggart K.: An Updated Strip Theory Program for Predicting Ship Motions and Sea Loads in Waves. *Technical Memorandum*, 1997.

Minsaas K. and Steen S.: Lecture notes for TMR4220. *Naval Hydrodynamics*, 2008.

Moctar B. et al.: Prediction of ship resistance and ship motions using RANSE. Gothenburg 2010: A Workshop on CFD in Ship Hydrodynamics, 2010.

Mousaviraad S.M. Carrica P.M. and Stern F.: Development And Validation Of Harmonic Wave Group Single-Run Procedure For Rao With Comparison To Regular Wave And Transient Wave Group Procedures Using URANS. *Journal of Ocean Engineering*, Vol. 37, pp 653-666, 2010.

Naito S.: Added resistance and speed loss. *Hydrodynamics in ship and ocean engineering*, RIAM, Kyushu University, pp.115-143, 2001.

Nakamura S. et al.: Propulsive performance of a container ship in waves (4th report).

Journal of Kansai Society of Naval Architects of Japan, No. 159, pp. 29-39, 1975.

Newman J.N.: Marine Hydrodynamics. The MIT Press, the U.S., 1977.

Nordas D.E.: Optimization of bow shape for large slow ships. M.S. thesis, Norwegian University of Science and Technology (NTNU), 2012.

Okawa H.: Motions, added resistance and nominal wake fluctuation in waves for KVLCC2 Ballast condition. B.S. thesis (in Japanese), Osaka University., 2013.

Ogiwara S. and Yamashita S.: On resistance increase in waves of short wave-length. Journal of Kansai Society of Naval Architects of Japan, No. 225, pp. 37-46, 1996.

Orihara H.: Comparison of CFD simulations with experimental data for a tanker model advancing in waves. International Journal of Naval Architect and Ocean Engineering, Vol. 3, pp 1-8, 2011.

Orihara H. and Miyata H.: Evaluation of added resistance in regular incident waves by computational fluid dynamics motion simulation using overlapping grid system. Journal of Marine Science and Technology, Vol. 8, Issue 2, pp. 47–60, 2003.

Sadat-Hosseini H. et al.: URANS simulation and valiation of added resistance and motions of the KVLCC2 crude carrier with fixed and free surge conditions. Gothenburg 2010: A Workshop on CFD in Ship Hydrodynamics, 2010a.

Sadat-Hosseini H. et al.: Head-waves parametric rolling of surface combatant. Journal of Ocean Engineering, Vol. 37, Issue 10, pp 859-878, 2010b.

Sadat-Hosseini H. et al.: CFD, system-based and EFD study of ship dynamic instability events: surf-riding, periodic motion, and broaching. Journal of Ocean Engineering,

Vol. 38, Issue 1, pp. 88-110, 2011.

Sadat-Hosseini H. et al.: CFD verification and validation of added resistance of KVLCC2 with fixed and free surge conditions in short and long head waves. *Journal of Ocean Engineering*, Vol. 59, pp. 240-273, 2013.

Salvesen N.: Added Resistance of Ships in Waves. *Journal of Hydronautics*, 1978.

Simonsen C. and Stern F.: CFD Simulation of KCS Sailing in Regular Head Waves. Gothenburg 2010: A Workshop on CFD in Ship Hydrodynamics, 2010.

Simonsen C. Otzen J. and Stern F.: EFD and CFD for KCS heaving and pitching in regular head waves. *Proceedings of the 27th Symposium on Naval Hydrodynamics*, Seoul, Korea, 2008.

Takai T. Kandasamy M. and Stern F.: Verification and Validation study of URANS simulations for axial waterjet propelled large high-speed ship. *Journal of Marine Science and Technology*, pp1-14, 2011.

Toxopeus S. et al.: Viscous-flow calculations for KVLCC2 in manoeuvring motion in deep and shallow water. AVT-189 Specialists Meeting on Assessment of Stability and Control Prediction Methods for NATO Air and Sea Vehicles, UK, 2011.

Tsukada Y. Hinatsu M. and Hasegawa J.: Measurement of unsteady ship wakes in waves. *J of Kansai Society of Naval Architects of Japan*, No. 228, pp. 15-20, 1997.

Ueno M. Tsukada Y. and Tanizawa K.: Estimate and prediction of effective inflow velocity to propeller in waves. *Journal of Marine science and Technology*, published online, DOI 10.1007/s00773-013-0211-8, 2013.

Weymouth G. Wilson R. and Stern F.: RANS CFD predictions of pitch and heave ship

motions in head seas. *Journal of Ship Research*, Vol. 49, pp. 80–97, 2005.

Xing T. and Stern F.: Factors of Safety for Richardson Extrapolation. *ASME J. Fluids Eng.*, Vol. 132(6), 061403: pp. 1-13, 2010.

Xing T. Carrica P. and Stern F.: Computational Towing Tank Procedures for Single Run Curves of Resistance and Propulsion. *ASME J. Fluids Eng.*, 130(2), pp. 1–14, 2008.

Xing T. Carrica P. and Stern F.: Developing Streamlined Version of CFDShip-Iowa-V4.5. *IIHR Technical Report No. 479*, 2011.

Ye H. Shen Z. and Wan D.: Numerical prediction of added resistance and vertical ship motions in regular head waves. *Journal of Marine Science and Application*, Vol. 11, Issue 4, pp410-416, 2012.

Yokota S.: The simple prediction method for body force distribution in CFD code. B.S. thesis (in Japanese), Osaka University, 2013.

Zakaria N.M.G. and Baree M.S.: Alternative Methods on Added Resistance of Ships in Regular Head Waves. *The Institution of Engineers, Malaysia*, Vol. 68, No. 4, 2008.

Zeraatgar H. and Abed H.F.: Added resistance & drift force analysis in regular and irregular waves. *Journal of Marine Engineering*, Vol. 2, No. 1, 2006.

Zhang S. Weems K.M. and Lin W.M.: Investigation of the horizontal drifting effects on ships with forward speed. *Proc. of the ASME 2009 28th Intl Conf. on Ocean, Offshore and Arctic Engineering*, Honolulu, Hawaii, USA, 2009.

Acknowledgement

Firstly, I would like to express my sincere gratitude to my adviser Prof. Yasuyuki Toda for giving this chance of studying in Japan and the U.S which is a dream come true. His instruction and knowledge will influence me profoundly in many ways, such as for my future work and being a researcher. I am particularly grateful for the support and instruction given by Prof. Frederick Stern to encourage me to conquer tough circumstances I ever met for this dissertation. Also, I would like thank Dr. Seyed Hamid Sadat Hosseini in particualr for mentoring the work related to CFDSHIP-IOWA and several papers. Several parts of this dissertation are mainly his work, such as the fully-loaded condition in long waves and facility biases. My special thanks are extended to the committee member and professors, such as Prof. Masashi Kashiwagi, Prof. Kazuhiko Hasegawa, Prof. Kiyoshige Matsumura, Prof. Hiroyoshi Suzuki, and Prof. Shigeru Naito for attending my final defense presentation and providing the valuable comments and reviewing this work. To my labmates in Japan and the U.S., and Prof. Yugo Sanada, it is great honor to work and live with them. I appreciate their kind help, especially when I was new in those places. Also, I would like to thank Dr. Yong-hee Lee and all my friends on the court. Spending a lot of enjoyable time together is the only way to bolster my morale during all kind of difficult circumstances. Finally, I wish this work is a contribution to engineering, especially for computation. Also, express my sincere respect to the person dedicating to experiment for their effort and hard working. “A theory is something nobody believes, except the person who made it. An experiment is something everybody believes, except the person who made it.” -Albert Einstein.

List of publications

JOURNAL PAPERS

Sadat-Hosseini, H., **Wu, P.-C.**, Carrica, P., Kim, H., Toda, Y., and Stern, F., (2013), “CFD verification and validation of added resistance of KVLCC2 with fixed and free surge conditions in short and long head waves”, Journal of Ocean Engineering, Vol. 59, pp. 240-273.

CONFERENCE PAPERS

Wu, P.-C., Sadat-Hosseini, H., Toda, Y., and Stern, F., (2013), “URANS studies of ship-ship interaction in shallow water”, Proceedings of 3rd International conference on ship manoeuvring in shallow and confined water, Ghent, Belgium.

Wu, P.-C., Sadat-Hosseini, H., Stern, F., and Toda, Y., (2013), “Nominal wake fluctuation due to waves: volume mean and distribution based on CFD and PIV”, Conference Proceeding of The Japan Society of Naval Architect and Ocean Engineering, Vol. 16, Hiroshima, Japan.

Wu, P.-C., Kim, H., Hayashi, Y., Oshita, S., and Toda, Y., (2012), “Added resistance and phase averaged wake field of KVLCC2 model ship in waves”, Proceedings of the 2nd East Asia International Student Symposium on Maritime Sciences (EAISS2012), Kobe, Japan.

Sadat-Hosseini, H., **Wu, P.-C.**, Toda, Y., Carrica, P., and Stern, F., (2011), "URANS studies of ship-ship interaction in shallow water", Proceedings of 2rd International conference on ship manoeuvring in shallow and confined water, Trondheim, Norway.

Curriculum vitae

Education

Doctoral Course, Naval Architecture and Ocean Engineering **2009 - present**

Osaka University (OU) - Suita, Japan

Adviser: Dr. Yasuyuki Toda

Areas of research: Computational fluid dynamics, ship hydrodynamics.

Current topic: CFDShip-IOWA V4.5, ship-ship interactions, free running self-propulsion using interactive propeller model in deep and shallow water, added resistance and ship motions of KVLCC2 in head waves under fully-loaded and ballast condition, nominal wake in waves.

Used topic: OpenFOAM to simulate ship waves induced by Wigley hull form, 2D viscous flow around a flat plane with periodic 3DOF motion in inertial coordinate system.

Received Interchange Association, Japan Scholarship (2009~2010); Scholarship by JASSO (Japan Student Services Organization) (2012~2013).

Visiting Research Scholar, IIHR-Hydroscience & Engineering **2010 - 2012**

University of Iowa (UI) - Iowa, United State

Adviser: Dr. Frederick Stern

Topic: CFDShip-IOWA V4.5, ship-ship interactions in shallow water and added resistance of KVLCC2 in short and long waves under fully-loaded condition.

Master of Science, Systems Engineering and Naval Architecture **2005**

National Taiwan Ocean University (NTOU) - Keelung, Taiwan

Adviser: Dr. Jiahn-Horng Chen

GPA: 3.90, Class rank: 3rd/22

Thesis: "Numerical Simulation of Supercavitating Projectile"

Areas of research: 3-D propeller panel code (PATPANS), 3-D cavitation model, water entry problem.

Bachelor of Science, Systems Engineering and Naval Architecture **2003**
National Taiwan Ocean University (NTOU) - Keelung, Taiwan
Overall GPA: 3.74/4.0, Junior / senior GPA: 3.90/4.0, Class rank: 2nd/41

Received Undergraduate Student Research Scholarship of National Science Council

R.O.C. 2002~2003

Received Certification of Presidential Award seven times 1999~2003

Professional Experience

Research Assistant, Dr. Jiahn-Horng Chen, NTOU **2007 - 2009**

Areas of research: Commercial code using Fluent and Gridgen, viscous cavitating flow simulation, and free surface simulation.

The Honor Guard of the Air Force, Taiwan (R.O.C) Military **2005 – 2006**

Teaching Assistant, Dr. Jiahn-Horng Chen, NTOU **2003 - 2005**

Curriculum topics: Probability theorem and linear programming.

Undergraduate Student Researcher, Advisor: Dr. Jiahn-Horng Chen **2002 - 2003**

Areas of research: FORTRAN programming, 2-D boundary element method, potential flow theory, and cavitation closure model.

Intern in Medium Cavitation Tunnel, Dr. Young-Zehr Kehr, NTOU **2001 - 2001**

Areas of research: Cavitation of high-speed, high-skew and inclined-shaft propeller.